MECHANISTIC DEVELOPMENT OF DECLINE CURVES FOR GAS-CONDENSATE RESERVOIRS

A Thesis

by

RIYAN ARIWIBOWO

Submitted to the Office of Graduate and Professional Studies of
Texas A&M University
in partial fulfillment of the requirements for the degree of

MASTER OF SCIENCE

Chair of Committee,	Maria A. Barrufet
Committee Members,	I. Yucel Akkutlu
	Marcelo Sanchez
Head of Department,	Dan Hill

May 2017

Major Subject: Petroleum Engineering

ABSTRACT

This study incorporates material balance, complex fluid behavior, reservoir characteristics, and well operating conditions into a mechanistic model to forecast production from gas-condensate reservoirs. The model can represent the behavior of the fluids and production from a gas-condensate reservoir, with considerations of condensate banking phenomena and adsorption, while running an order of magnitude faster than a commercial compositional reservoir simulator.

The constant volume depletion (CVD) process serves as a basis to estimate production from gas-condensate reservoirs by coupling a robust phase-behavior calculation using a thermodynamic cubic equation of state (EOS) and radial flow equations. The mechanistic method developed in this project establishes the relationship between production and time.

The CVD test is coded as a multicompositional molar-accounting program that simulates gas-condensate phase behavior. As near-wellbore and reservoir pressures drop below saturation pressure, in gas-condensate reservoir condensate banking occurs, hindering flow. The two-tank CVD approach developed in this work models the near-wellbore liquid saturation buildup caused by this phenomenon.

The modified CVD provides a material balance base for the method. The backbone of this model is the vapor/liquid equilibrium (VLE) calculation with the Peng-Robinson equation of state (EOS). Produced fluid volumes are calculated with each CVD pressure decrease. Using this information coupled with the flow equation, the model can forecast production behavior. Cumulative oil and gas production comparisons between the results from this model and those from a compositional reservoir simulator show an average absolute error of around 4%. Oil and gas production rate forecasts from this model have an average absolute error of 15% from the compositional reservoir simulator forecasts. Comparison of results from this model with those from the commercial simulator shows the importance

of considering condensate accumulation effects on productivity and accurately predicting flow from the gas-condensate reservoir.

In the model, hydraulic fracture well completions are represented with an equivalent skin factor. In this case, the effect of condensate banking is less significance, and the new model produced results comparable to production forecasted by the commercial simulator.

This model is unique because it uses the CVD process as a material balance basis to predict production. This process provides the physical basis for reservoir engineers to predict production behavior of a gas-condensate reservoir, instead of the empirically based predictions from conventional decline analysis. This simple tool can also be incorporated to the evaluating prospects before further in-depth reservoir studies are conducted.

DEDICATION

This thesis is dedicated to:

My mother, Huntje Marcella

My father, Bayong Chandra Wibowo

My brother, Randy Ardywibowo

ACKNOWLEDGEMENTS

I would like to thank my family, friends, colleagues and committee members for their continued assistance in helping me complete this work. I am very grateful to Dr. Maria Barrufet for her overwhelming understanding, support, and guidance to help me become a better engineer and scholar. Also, my appreciation to Dr. Yucel Akkutlu and Dr. Marcelo Sanchez for their help and support as my committee members.

CONTRIBUTORS AND FUNDING SOURCES

Contributors

This work was supervised by a thesis committee consisting of Professor Maria A. Barrufet and Professor I. Yucel Akkutlu of the Department of Petroleum Engineering and Professor Marcelo Sanchez of the Department of Civil Engineering.

All work for the thesis was completed by the student, in collaboration with Professor Maria A. Barrufet of the Department of Petroleum Engineering.

Funding Sources

There are no outside funding contributions to acknowledge related to the research and compilation of this document.

NOMENCLATURE

A	mixing constant
a	LBC constant
b	PR covolume parameter
f	fugacity of pure component
$\hat{f}$	fugacity of mixture
f_α	molar fraction of phase ($\alpha = v, l$)
G_{SL}	Langmuir volume
k	permeability
k_r	relative permeability
k_{abs}	absolute permeability
k_{eff}	effective permeability
K	vapor/liquid equilibrium ratio
M_w	molecular weight
N_c	number of components
p	pressure
p_c	critical pressure
p_L	Langmuir pressure
q_{gsc}	gas rate at standard conditions
R	gas constant
T	temperature
T_c	critical temperature
T_r	reduced temperature
v	volume
V_m	molar volume
x_i	molar fraction of component i in the liquid phase
y_i	molar fraction of component i in the gas phase
Z	gas compressibility factor

Greek Symbols

ω	acentric factor
γ	specific gravity
φ	fugacity coefficient of pure component
μ	viscosity
ρ	density
ξ	viscosity parameter

Superscripts

L	liquid phase
ℓ	phase
V	vapor phase

Subscripts

c	critical
i	component i
j	component j
l	liquid phase
m	mixture
pc	pseudocritical
pr	pseudoreduced
r	reduced
v	vapor phase

Abbreviations

API	American Petroleum Institute
BHP	bottomhole pressure
CVD	constant volume depletion
DCA	decline curve analysis

EOS	equation of state
EUR	estimated ultimate recovery
GOR	gas/oil ratio
LBC	Lorentz-Bray-Clark
PR	Peng-Robinson
PVT	pressure/volume/temperature
SRK	Soave-Redlich-Kwong
VLE	vapor/liquid equilibrium

Units

md	milidarcy
MSCF/D	thousand standard cubic feet per day
SCF	standard cubic feet

TABLE OF CONTENTS

Page

LIST OF FIGURES

Page

LIST OF TABLES

Page

CHAPTER I

INTRODUCTION

Gas-condensate reservoirs are an important source of energy for the United States, with prevalent resources found along the Texas-Louisiana gulf coast. Shale resource developments initially targeted dry-gas regions and are now shifting focus towards liquid-rich regions. The use of horizontal drilling and hydraulic fracturing has made it possible to produce hydrocarbons from these nanodarcy formations. The production from liquid-rich shale resources in the US has contributed to the increase of US domestic hydrocarbon production. As shown in Figure 1, production from liquid-rich reservoirs increased significantly starting 2010 and peaked at 4.5 million barrels of oil per day in 2015. The majority of the contribution comes from the Eagle Ford and Bakken shale resources.

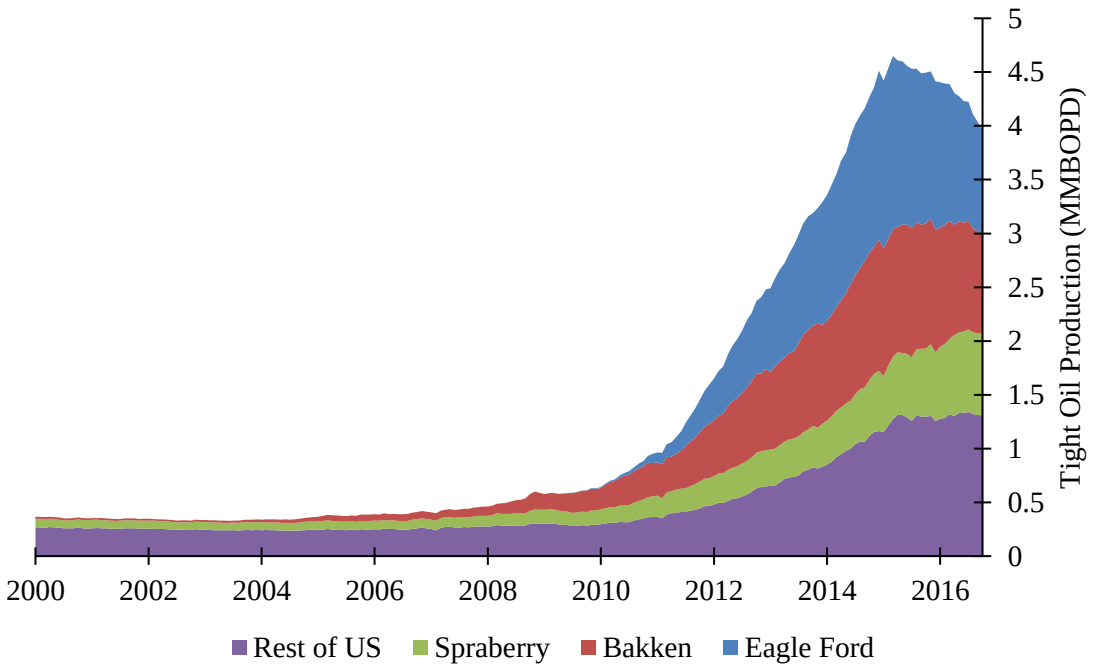

Figure 1 – U.S. tight oil production in million barrels of oil per day. Created from data gathered by EIA (2016) through October 2016.

As industry interest move to liquid-rich shale plays, we need to be able to accurately predict performance from these types of reservoirs. Decline curve analysis (DCA) models have been developed to tackle the problem of forecasting depletion including in tight/shale reservoirs. The Arps decline curve and the modified hyperbolic methods are easy to use, but they are empirically based and may lead to unrealistic prediction. For example, using the Arps decline parameter *b* greater than 1 leads to infinite ultimate recovery, which is not possible.

Compositional reservoir simulation is another conventional method to accurately predict the production performance from gas-condensate reservoirs. However, compositional reservoir simulations have longer simulation run times, adding to the cost of the study. The number of grids and components add to the simulation run time. Consider a simple homogeneous reservoir, composed of 15,000 grid blocks and a reservoir fluid of 11 components. Simulating a single producing well at the center of the reservoir with constant bottomhole flowing pressure takes up to an hour to complete. This is not practical when engineers need to evaluate hundreds of wells.

1.1 Definition of Problem

Increasing industry focus on liquid-rich and gas-condensate reservoirs creates the need for accurate and fast method to forecast production. Current proposals of DCA are empirically based and lack the physics-based considerations. Though numerical simulators provide more accuracy to the prediction, simulations require longer to process and thus become expensive.

The fast, simple model presented in this project can predict production performance of gas-condensate reservoirs. It incorporates retrograde gas behavior and produces comparable performance to reservoir simulation runs. The model, which is based on physical phenomena that occur in the reservoir, is cost effective and can assess

deliverability of gas-condensate reservoir production under common operational strategies.

1.2 Objectives

The main goal of this project was to develop a mechanistic production decline model that can be used to forecast the production behavior of liquid-rich systems. This was accomplished by coupling a modified constant volume depletion (CVD) approach with a flow equation. Specific tasks in this project included:

- Developing a simulated CVD test in Excel Visual Basic (VBA) and validating it with commercial software (PVTi)
- Developing a production decline model of multicomponent liquid-rich reservoirs by coupling the CVD with flow equations
- Incorporating adsorption and relative permeability effects into to the CVD and productivity equations

1.3 Description of Chapters

Chapter I describes the objectives and relevance of the work and method proposed in this thesis. In Chapter II, the fundamental basis of the research is explained. I define a gas-condensate fluid and its behavior, specifically retrograde condensation. I also describe the fundamental equations to model the constant volume depletion test: the Peng-Robinson equation of state, which is used in the vapor/liquid equilibrium calculation and volumetric computations, and the flow equations, real-gas pseudopressure, and fracture representation for the development of the mechanistic model. In addition, I describe the extended Langmuir model used for multicomponent adsorption modeling. The software I used are also defined in this chapter.

Chapter III explains the development of the constant volume depletion test in Visual Basic for Application (VBA). Here, I present the workflow of the calculations to simulate the

constant volume depletion and the modifications made to the CVD, which allows production of gas with liquid and production beginning above the dewpoint. I also validate the constant volume depletion developed with a commercial pressure/volume/temperature simulator and present the method for coupling adsorption to the constant volume depletion.

Chapter IV describes coupling between the flow equations and the constant volume depletion. This chapter details the inputs necessary and the workflow to create a production forecast of a gas-condensate well. Well operational rules (minimum bottomhole pressure, constant rate, and drawdown pressure constraint) and well completion (e.g. hydraulic fracturing) are explained in this chapter.

I compared the prediction from this new model to a commercial reservoir simulator and obtained good agreement absolute average error was within 15% for gas rate and 4% for cumulative gas production for a single well producing from the center of a gas-condensate reservoir. For the case considering hydraulic fracturing, our method tends to overestimate production, with an average absolute error of 19% for gas rate and 13% for cumulative gas production. A closer look at the commercial reservoir simulation shows condensate buildup impeding gas flow to the well, causing disagreement between the commercial and the mechanistic forecasts.

Also in Chapter IV, I discuss the limitation in applying the constant drawdown constraint for our model. This limitation is caused by the different definitions of drawdown pressure between the commercial simulator and the mechanistic model. I attempted to remedy this discrepancy, but further studies are needed to accurately forecast a well producing under a constant drawdown pressure using this new model.

I also compared the capabilities of forecasting by this method and the Arps decline curve method for a well producing with constant bottomhole pressure. This forecasting method

is beneficial in determining spacing for the reservoir development and for finding initial gas/oil in place.

As discussed in Chapter IV, the liquid saturation buildup in the near-wellbore region impedes the gas flow into the wellbore. In Chapter V, I present three approaches to explore estimation of liquid saturation buildup in the condensate bank region. These approaches are based on a small tank, simulated as a CVD test with production and replenishment alterations, to model the condensate banking. Liquid saturation estimated from the small tank is used to obtain a relative permeability value to be used in the flow equation. Calibrating the production forecast with these approaches resulted in a better agreement with the results from the compositional reservoir simulator. Of the three methods developed, I recommend the use of the y^* method to calibrate the production forecasts because of its simplicity.

Finally, Chapter VI contains the conclusions and recommendations obtained from this research.

CHAPTER II

LITERATURE REVIEW

2.1 Gas-Condensate Reservoirs

Gas-condensate reservoirs are hydrocarbon-bearing formations at temperatures between the critical point and the cricondentherm of the reservoir fluid (Thomas et al. 2009). The phase envelope (pressure/temperature) of a typical gas-condensate fluid is illustrated in Figure 2. When the reservoir pressure is above the dewpoint pressure, the fluid exists as a single-phase gas in the reservoir. During depletion, as reservoir pressure falls below the dewpoint, retrograde condensation occurs. This causes liquid (condensate) to drop out of the gas phase and accumulate in the reservoir. The presence of gas and liquid in the reservoir leads to multiphase flow, which hinders the production of gas condensates. Liquid that drops out within the reservoir will not flow and cannot be produced (McCain 1990), unless liquid saturation reaches the critical oil saturation (S_{oc}).

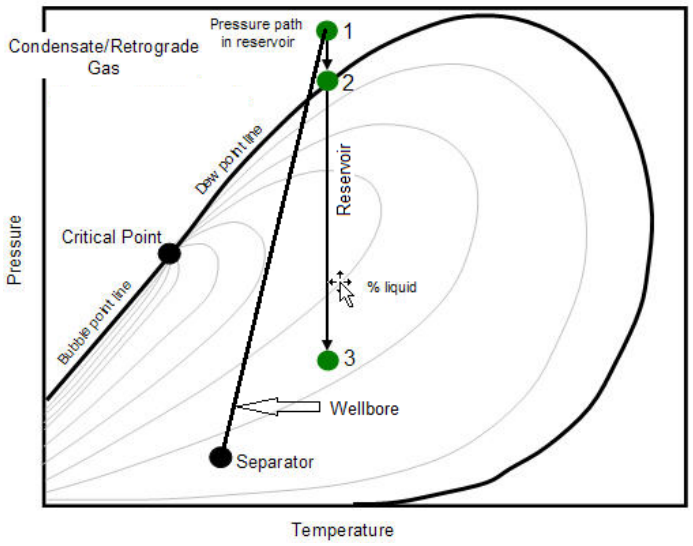

Figure 2 – Schematic of a gas-condensate phase envelope (Fekete 2014). The gas-condensate reservoir experiences a unique depletion regime due to the crossing of the dewpoint.

The main differences between gas-condensate and oil-associated reservoir gas are that gas-condensates contain large amounts of methane and ethane; the liquid condensate is made up of propane, butanes, and pentanes, where in crude oil it is mostly heptane plus; and the heptane-plus components of crude oil are heavier than gas condensates. Typical fluid properties to classify reservoir fluids are elaborated in Table 1.

Table 1 – Typical fluid properties of five reservoir fluid types (McCain 1994).

	Black Oil	Volatile Oil	Retrograde Gas	Wet Gas	Dry Gas
Initial producing gas/liquid ratio (SCF/STB)	<1,750	1,750 to 3,200	>3,200	>15,000	100,000
Initial stock-tank liquid gravity, °API	<45	>40	>40	Up to 70	No liquid
Color of stock-tank liquid	Dark	Colored	Lightly colored	no color	No liquid
Heptanes plus, mol%	>20	20 to 12.5	<12.5	<4	<0.7

Typically, according to McCain (1990), gas-condensate reservoirs have a gas/oil ratio (GOR) from 3,300 to 150,000 scf/STB. The GOR may be higher if reservoir temperature is closed to the critical point or lower if reservoir temperature is close to the cricondentherm. Producing GOR will increase when reservoir pressure decreases below the dewpoint. Stock-tank gravities of oil associated with the gas condensate typically range from 40° to 60° API. The strong dependency of the fluid on pressure, temperature, and composition requires a fluid description more detailed than GOR and liquid gravity, so the fluids are defined in terms of percentage of each hydrocarbon component in the gas-condensate mixture. Compositional analysis of a fluid sample taken from the producing well is important to understanding the behavior of the fluid as pressure decreases. With information of the overall composition, pressure, and temperature, we can predict the phase(s) of the fluid using the vapor-liquid equilibrium calculation with the Peng-Robinson equation of state.

2.1.1 Condensate Banking

Condensate banking is the accumulation of liquid in the near-wellbore region of the reservoir due to pressure falling below the dewpoint (Figure 3). This liquid dropout phenomenon hinders the flow of gas due to the decrease in gas relative permeability. As noted in the literature, as pressure in the reservoir declines below the dewpoint, condensate can rapidly build up (Barker 2005; Wheaton and Zhang 2000). Additionally, tight/low-permeability formations exacerbate condensate banking due to the significant pressure drop (Giamminonni et al. 2010; Lee and Chaverra 1998).

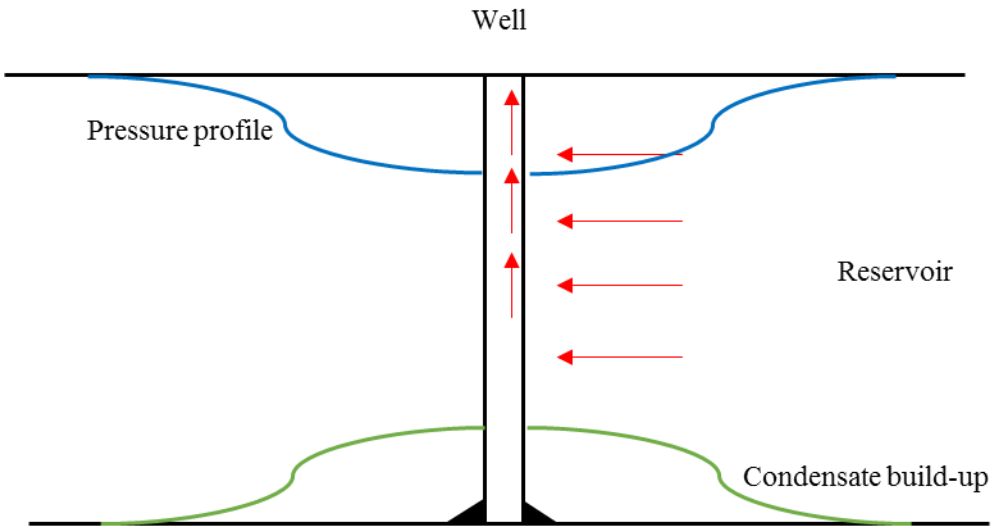

Figure 3 – Illustration of condensate buildup in the near-wellbore area as pressure decreases below the dewpoint.

Operators typically implement production strategies to avoid condensate buildup. These strategies are mostly related to pressure maintenance (Sayed and Al-Muntasheri 2014), such as keeping the bottomhole pressure (BHP) above saturation pressure or gas injection for pressure maintenance. Some operators also attempt remediation by implementing well shut-ins to build up pressure, thus revaporizing the condensates and recovering gas flow. Methods to circumvent this condensate-banking problem include drilling horizontal wells,

re-entry drilling, or hydraulic fracturing completions (Luo and Barrufet 2006; Sayed and Al-Muntasheri 2014; Smits et al. 2001).

Because condensate banking in the vicinity of the wellbore impacts the production from gas-condensate reservoirs, several methods have been developed to forecast its presence. These include compositional reservoir simulation studies with fine gridding and empirical models that can account for the production decrease it causes.

Compositional reservoir simulation is a forecasting method used for gas-condensate reservoirs. The near-wellbore area experiences a greater change in pressure than the rest of the reservoir, thereby becoming the area of interest for condensate banking effects. Here, coarse grid blocks are not capable of characterizing the change in saturation around the wellbore. Finer gridding and local grid refinement (LGR) near the wellbore have been shown to capture liquid build up in the reservoirs (Barker 2005; Huerta Quinones et al. 2012). Accounting for pressure, temperature, and composition, numerical simulators are able to obtain an accurate prediction of condensate saturation and the proper relative permeability for gas flow calculations. This method is popular for well deliverability forecasting as well as field forecasting, but it is expensive to do because of the long simulation times (Lee and Chaverra 1998; Smits et al. 2001).

The cost of compositional numerical simulation prompts research to find simpler and less expensive methods. Mott (2002) acknowledges the need for quicker and/or easy-to-use methods for predictions of gas-condensate deliverability, such as using a material balance model combined with an inflow performance relationship (IPR). Mott's work follows work by Fevang and Whitson (1996) that combines PVT properties, gas/oil relative permeabilities, and pseudopressure to calculate well deliverability.

This thesis presents a simple model that uses the constant volume depletion mechanism as a basis for material balance. I used the Peng-Robinson equation-of-state (EOS) with

volume translation (Péneloux et al. 1982) to conduct the vapor-liquid equilibrium calculations and derive volumetric properties. This method is compositional, accounting for the molecular mass transfer across phases. I coupled the CVD results with a pseudosteady-state flow equation to produce a well deliverability forecast.

2.1.2 Eagle Ford: Low-Permeability Gas Condensate

One of the main motivations for this study was to provide well deliverability forecasts from wells producing in the gas-condensate window of shale/low-permeability reservoirs. Located in south Texas, the Eagle Ford resource is one of the most prolific producers of hydrocarbons in the US. Geologically, the Eagle Ford shale resource has a downdip structure from north to south. As a result, the depth of the Eagle Ford is in the range of 2,500 ft in the north to 14,000 ft in the south. Temperature gradient, caused by the depth variation, impacts the thermal maturity of the petroleum fluids that are present in the formation. Oil and liquid-rich resources are more prevalent in the shallower regions in the north, while gas-condensate and dry gas become more prevalent in the deeper regions in the south.

As a formation, the Eagle Ford has a thickness ranging from 120 to 350 ft. The high carbonate and low clay content provides the brittleness that makes hydraulic fracturing stimulation easier (Pope et al. 2012). Production from the Eagle Ford is mostly through horizontal wells with multistage hydraulic fracturing.

Gong et al. (2013) divided the Eagle Ford shale play into eight production regions based on the geology, fluid type, and well performance (Figure 4). Though the Eagle Ford produces a great variety of hydrocarbon types, this work focused on the gas-condensate production region.

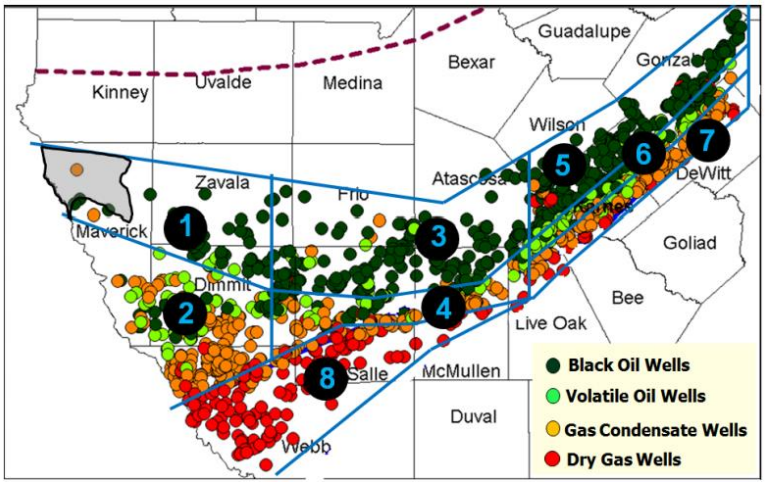

Figure 4 – Modified from Gong et al. (2013). The Eagle Ford is divided into eight production regions based on the fluid type, geology, and well performance. Production Region 2 (PR 2), a gas-condensate region, is located in the southern portion of Maverick county and western Dimmit county. The gas-condensate regions are located between the oil window in the north and the gas window in the south.

The composition of the gas-condensate modeled in this project matches that of Gong et al.'s Production Region 2 (PR 2), as presented in Table 2. The gas-condensate fluid sample was used in this work to create deliverability forecasts, which were validated through comparison with results from a commercial reservoir simulator.

Table 2 – Composition of gas-condensate production region 2 (Gong et al. 2013).

Component	Composition
N_2	0.07
CO_2	0.81
C_1	65.57
C_2	12.98
C_3	6.17
iC_4	1.50
nC_4	2.42
iC_5	1.08
nC_5	1.02
C_6	1.38
C_{7+}	7.04

C_{7+} Molecular Weight	177.11
C_{7+} Specific Gravity	0.8

2.2 Constant Volume Depletion Test

The constant volume depletion (CVD) test is a pressure/volume/temperature (PVT) experiment that is conducted in the laboratory for gas-condensate and volatile oil samples. The CVD test mimics the production mechanism of a gas-condensate reservoir by reservoir pressure depletion and fluid expansion. Information obtained from the CVD test can be directly used by engineers for the material balance relationship between average reservoir pressure and fluid recovery. Additionally, composition of the recovered fluids and the reservoir liquid (oil) saturation due to liquid dropout can be determined.

The regular laboratory CVD test is illustrated in Figure 5 for a gas-condensate sample, and the procedure is as follows:

1. A sample fluid is charged into a variable volume PVT cell at reservoir temperature and saturation pressure, which can be determined from a constant composition expansion (CCE). This initial measured volume is the reference volume.
2. Pressure is then decreased by increasing the volume of the PVT cell. As the cell pressure decreases, the fluid is allowed to expand, and a second phase evolves – liquid for gas-condensates or gas for volatile oils.
3. The volume of the PVT cell is decreased back to the initial (reference) volume, while simultaneously withdrawing the equivalent volume of vapor.
4. The liquid volume is measured as a fraction of cell volume, and provides the liquid saturation at cell pressure (Whitson and Torp 1981).
5. The cycle is then repeated until the desired ending pressure is reached.

As noted previously, this process can be applied to a volatile oil sample as well.

The vapor removed from the PVT cell is further expanded to standard conditions. The produced sample is then analyzed in the laboratory to obtain gas composition, moles produced (as a percentage of initial moles), and evaluation of heptanes-plus component.

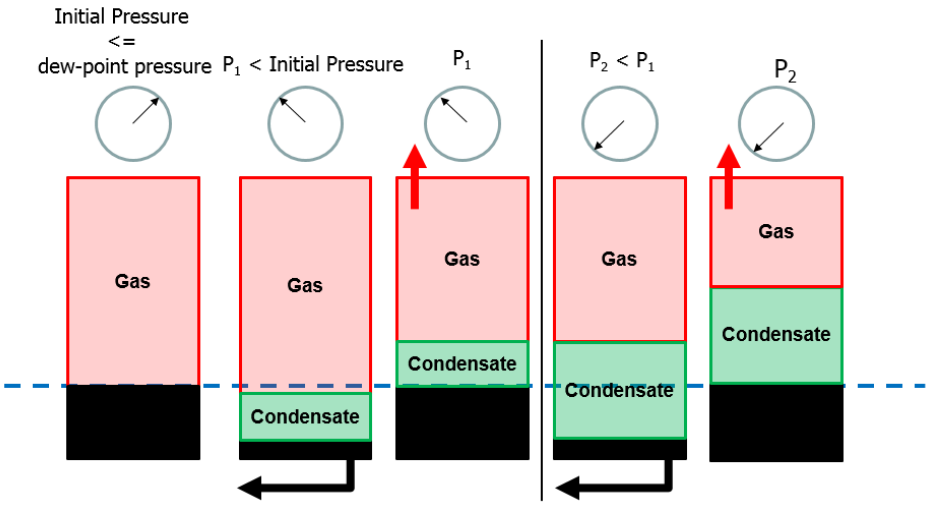

Figure 5 – Constant Volume Depletion (CVD) test illustration for a gas-condensate fluid sample.

In this work, I coded the CVD test in VBA. To simulate the phase behavior of multicomponent hydrocarbons, I calculated the phase equilibrium using the Peng-Robinson (PR EOS) equation of state with volume translation. The PR EOS and Vapor/Liquid equilibrium (VLE) are further described in the following subsections.

2.2.1 Equation of State

An equation of state (EOS) is a thermodynamic model which describes the phase behavior of a single component or mixture as a function of pressure, temperature, and composition. Equations of state can be used to calculate gas/liquid equilibria, with the assumption that the chemical potential of gas and liquid at equilibrium are the same.

Peng and Robinson (1976) introduced an equation of state model that improved upon the Soave-Redlich-Kwong (SRK) EOS (Soave 1972). At the time, the SRK EOS was popular with the industry due to its simplicity, but it had trouble predicting acceptable density values for liquid. Peng and Robinson improved this by proposing an EOS that improves liquid density prediction and provides accurate vapor pressure and equilibrium ratios. The PR EOS is presented in Eq. 2.1 with the attraction parameter (a) and van der Waals co-volume (b), shown in Eq. 2.2 and Eq. 2.3.

$$p = \frac{RT}{V_m - b} - \frac{a\alpha}{V_m^2 + 2bV_m - b^2} \tag{2.1}$$

$$a = 0.45724 \frac{R^2 T_c^2}{P_c^2} \tag{2.2}$$

$$b = 0.07780 \frac{RT_c}{P_c} \tag{2.3}$$

$$\alpha = \left[1 + m\left(1 - \sqrt{T_r}\right)\right]^2 = \left[1 + m\left(1 - \sqrt{\frac{T}{T_c}}\right)\right]^2 \tag{2.4}$$

where:

$$m = 0.37464 + 1.54226\,\omega - 0.2699\,\omega^2 \text{ for } \omega \leq 0.5$$

$$m = 0.037464 + 1.485\,\omega - 0.1644\,\omega^2 + 0.01667\,\omega^3 \text{ for } \omega > 0.5$$

The PR EOS can be represented in terms of the compressibility factor Z and is shown in Eq. 2.5, where the variables A and B are calculated using Eq. 2.6 and Eq. 2.7. The cubic form of the PR EOS is commonly used for computational purposes.

$$Z^3 - (1 - B)Z^2 + (A - 3B^2 - 2B)Z - (AB - B^2 - B^3) = 0 \tag{2.5}$$

$$A = \frac{a\alpha p}{R^2 T^2} \tag{2.6}$$

$$B = \frac{bp}{RT} \tag{2.7}$$

For a multicomponent fluid of N_c components, mixing rules must be used for the parameters $(a\alpha)_m$ and b_m. The mixing rules are described in Eq. 2.8 and Eq. 2.9, in which the subscripts i and j denote the component, while x indicates the component's mole fraction in the liquid phase (the same formula can be used for the gas phase). A quadratic mixing rule is used for parameter $(a\alpha)_m$, while a linear mixing rule is used for parameter b. The k_{ij} term represents the binary interaction coefficient between component i and j. The binary interaction coefficient is empirically determined and is used to improve EOS predictions.

$$(a\alpha)_m = \sum_{i=1}^{N_c} \sum_{j=1}^{N_c} x_i x_j \sqrt{a_i \alpha_i a_j \alpha_j}(1 - k_{ij}) \tag{2.8}$$

$$b_m = \sum_{i=1}^{N_c} x_i b_i \tag{2.9}$$

2.2.2 Vapor-Liquid Equilibrium (VLE)

The objective of the VLE calculation is to determine the phase or phases of a specified fluid composition at a given pressure and temperature in equilibrium. The PR EOS is used in this work for the VLE calculation. The compressibility factor and molar volumes for each phase can be derived from the VLE.

The fugacity coefficient is an important term in the VLE calculation. The fugacity coefficient for component i in a multicomponent fluid mixture is defined as the ratio of fugacity to partial pressure, and can be calculated using Eq. 2.10. In this work, I assume that the gas and liquid phases are under the same pressure, thus ignoring capillary pressure effects.

$$\ln(\hat{\varphi}_i) = \ln\left(\frac{\hat{f}_i^{\ell}}{x_i p}\right)$$

$$\ln(\frac{\hat{f}_i^{\ell}}{x_i p}) = \frac{b_i}{b}\left(Z^{\ell} - 1\right) - \ln\left(Z^{\ell} - B\right)$$

$$-\frac{A}{2\sqrt{2}B}\left[\frac{2\sum_{j=1}^{N_c} z_j \sqrt{a_i \alpha_i a_j \alpha_j}\left(1 - k_{ij}\right)}{\alpha} - \frac{b_i}{b}\right] \ln\left(\frac{Z + 2.414B}{Z - 0.414B}\right) \tag{2.10}$$

The VLE calculation is based on the condition of isofugacity, where the fugacity of a component is the same in the liquid and vapor phases, as described in Eq. 2.11.

$$\hat{f}_i^{l} = \hat{f}_i^{v} \tag{2.11}$$

The fugacity of the component can be expressed in terms of pressure (p) and the fugacity coefficient ($\hat{\varphi}$) as noted in Eq. 2.12 and Eq. 2.13. The superscripts v and l denote the vapor/gas phase and the liquid phase, respectively.

$$\hat{f}_i^l = x_i \hat{\varphi}_i^l p \tag{2.12}$$

$$\hat{f}_i^v = y_i \hat{\varphi}_i^v p \tag{2.13}$$

The equilibrium ratio (K_i) is the mole fraction of component i in the vapor phase (y_i), divided by the mole fraction of component i in the liquid phase (x_i). Setting the fugacities of the component equal and using the definition of the K-value, we obtain Eq. 2.14 for the equilibrium relationship.

$$K_i = \frac{y_i}{x_i} = \frac{\hat{\varphi}_i^l}{\hat{\varphi}_i^v} \tag{2.14}$$

VLE calculations imply material balance for each component. In Eq. 2.15, z_i is the overall composition of component i and f_v is the molar fraction of vapor. The mole fraction of component i in the liquid and gas phases is represented by x_i and y_i, respectively.

$$z_i = f_v y_i + (1 - f_v) x_i \tag{2.15}$$

A method proposed by Rachford Jr and Rice (1952) combines the equilibrium K-value ratio and the component's material balance. Combining Eq. 2.14 and 2.15 and solving for y_i and x_i, we get Eq. 2.16 and Eq. 2.17.

$$y_i = \frac{z_i}{1 - f_v + f_v K_i} \tag{2.16}$$

$$x_i = \frac{K_i z_i}{1 - f_v + f_v K_i} \tag{2.17}$$

The mole fractions in each phase must sum to unity, so the relationship in Eq. 2.18 can be established.

$$\sum_{i=1}^{N_c}(y_i - x_i) = 0 \tag{2.18}$$

The Rachford-Rice equation is established by substituting Eq. 2.16 and Eq. 2.17 into the mole fraction relationship in Eq. 2.18.

$$\sum_{i=1}^{Nc}(y_i - x_i) = \sum_{i=1}^{N_c}\frac{z_i(K_i - 1)}{1 + f_v(K_i - 1)} = 0 \tag{2.19}$$

There are several methods to the solve the VLE calculation (Mollerup and Michelsen 1992; Smith et al. 2005). The method used in this work is described in Firoozabadi (1999). Given pressure, temperature, and overall fluid composition, the VLE calculation is described below in seven main steps.

1. First, calculate an initial guess for the equilibrium ratio, K-value, for each component i. This can be done through using Wilson (1969) equation described in Eq. 2.20.

$$K_i = \frac{p_{c_i}}{p}\exp\left[5.37(1 - \omega_i)\left(1 - \frac{T_{c_i}}{T}\right)\right] \tag{2.20}$$

2. Then, use the Rachford-Rice equation to obtain the vapor molar fraction (f_v) in Eq. 2.21. This function is numerically well-behaved (monotonic) and thus suitable for computation.

$$\sum_{i=1}^{Nc}\frac{z_i(K_i - 1)}{1 + f_v(K_i - 1)} = 0 \tag{2.21}$$

3. Proceed to calculate the molar fraction of the component in the gas (y_i) and liquid (x_i) phases using Eq. 2.17 and Eq. 2.18.
4. Calculate the fugacity coefficient for gas ($\hat{\varphi}_i^v$) and liquid ($\hat{\varphi}_i^l$) phases using Eq. 2.10.
5. Update the K-value for each component i using Eq. 2.22.

$$K_i^{\text{new}} = K_i^{old}\left(\frac{\hat{\varphi}_i^v}{\hat{\varphi}_i^l}\right) \tag{2.22}$$

6. Test the convergence and error tolerance, ϵ.

$$\epsilon_i = \left|K_i^{new} - K_i^{old}\right| \tag{2.24}$$

$$\epsilon = \max(\epsilon_i) \tag{2.25}$$

7. If the convergence is not achieved, then update the K-values with Eq. 2.22, then repeat steps 2 through 7.

2.2.3 Volume Calculation for Hydrocarbons

The relative volumes of the hydrocarbon phases are important to determine saturations, as explained further in Chapter III. Once the vapor/liquid equilibrium is reached, the hydrocarbon volume can be calculated. The molar volume of the l and v phases can be calculated using Eq. 2.26 and Eq. 2.27, respectively.

$$V_{m_l}^{\text{EOS}} = \frac{Z^l(x_i, p, T)RT}{p} \tag{2.26}$$

$$V_{m_v}^{\text{EOS}} = \frac{Z^v(y_i, p, T)RT}{p} \tag{2.27}$$

Volumetric calculations with Peng-Robinson EOS often deviate from laboratory experiments. Péneloux et al. (1982) proposed a volume translation method to correct the volume calculation without changing the VLE calculation results. The volume translation

is done by introducing a correction term c_i, which is calculated using a shift factor (s_i) and b_i parameter for each component. The correction term for component i (c_i) is described in Eq. 2.28. The term b is the Peng-Robinson *c*-volume in Eq. 2.3.

$$c_i = s_i b_i \tag{2.28}$$

This overall correction term for liquid and vapor is then calculated using Eq. 2.29 and Eq. 2.30, respectively, for a fluid of component N_c.

$$c_l = \sum_{i=1}^{N_c} c_{l_i} x_i \tag{2.29}$$

$$c_v = \sum_{i=1}^{N_c} c_{v_i} y_i \tag{2.30}$$

In Eq. 2.31 and Eq. 2.32, the calculated correction term is used to shift the molar volume calculated through the EOS.

$$V_{m_l} = V_{m_l}^{\mathrm{EOS}} - c_l \tag{2.31}$$

$$V_{m_v} = V_{m_v}^{\mathrm{EOS}} - c_v \tag{2.32}$$

2.2.4 Viscosity Calculation for Hydrocarbons

Fluid viscosity required in all flow calculations. Using fluid properties calculated from the EOS, fluid viscosities are calculated using the LBC correlation presented in Lohrenz et al. (1964). This viscosity correlation is based on the theory of corresponding states using reduced density. This correlation is presented as a fourth-order polynomial in Eq. 2.33.

$$\mu = \mu_0 + \frac{1}{\xi}[(0.1023 + 0.023364\rho_r + 0.058533\rho_r^2 - 0.040758\rho_r^3 - 0.0093324\rho_r^4)^4 - 10^{-4}] \quad (2.33)$$

where

μ = viscosity (cp)

μ_0 = viscosity at atmospheric pressure (cp)

ξ = viscosity parameter (cp^{-1})

ρ_r = reduced molar density

The definitions of the terms in the LBC correlation are presented in Eq. 2.34 – Eq. 2.37. The reduced molar density is calculated as a ratio of molar density to pseudocritical molar density (Eq. 3.34). The pseudocritical molar density is calculated using the critical volume in Eq. 3.35.

$$\rho_r = \frac{\rho}{\rho_{pc}} \quad (2.34)$$

$$\rho_{pc} = \frac{1}{\sum_{i=1}^{N_c} z_i V_{c_i}} \quad (2.35)$$

$$\xi = \frac{T_{pc}^{1/6}}{M_w^{1/2}\ p_{pc}^{2/3}} \quad (2.36)$$

$$\mu_0 = \frac{\sum_{i=1}^{N_c} z_i \mu_i \sqrt{M_{w_i}}}{\sum_{i=1}^{N_c} z_i \sqrt{M_{w_i}}} \quad (2.37)$$

where

T_{pc} = pseudo-reduced temperature

p_{pc} = pseudo-reduced pressure

M_{w_i} = molecular weight of component i

z_i = molar composition of component i

V_{c_i} = critical volume of component i

The pseudocritical properties are calculated with the following equations.

$$T_{pc} = \sum_{i=1}^{N_c} z_i T_{c_i} \tag{2.38}$$

$$p_{pc} = \sum_{i=1}^{N_c} z_i p_{c_i} \tag{2.39}$$

The component viscosity (μ_i) for Eq. 2.37 can be obtained from the following correlations (Stiel and Thodos 1961), presented in Eq. 2.40.

$$\mu_i = \begin{cases} \dfrac{0.00034 T_{r_i}^{0.94}}{\xi}, & \text{if } T_{r_i} \leq 1.5 \\ \dfrac{0.0001776\left(4.58 T_{r_i} - 1.67\right)^{5/8}}{\xi}, & \text{if } T_{r_i} > 1.5 \end{cases} \tag{2.40}$$

From this calculation, we obtain the viscosity for the phases to be used in the flow equation coupled with the CVD.

2.3 Flow Equation

To produce a forecast of production, the material balance provided by the CVD must be coupled with a flow equation. In petroleum engineering, Darcy's law (1856) governs the flow of fluids in a porous medium that can be expressed as in Eq. 2.41.

$$q = -\frac{kA}{\mu}\frac{\partial P}{\partial L} \tag{2.41}$$

The derivations of the gas flow equation for transient, steady-state and pseudosteady-state flow are detailed by Economides et al. (2012). Due to large differences between the gas

rate at bottomhole and surface conditions, it is customary to report the gas rate in surface conditions as thousand standard cubic feet per day (MSCF/D). It is also common to use field units for variables in the flow equations, so a conversion constant is needed. Assumptions in this derivation include isothermal reservoir condition and homogeneous reservoir properties.

2.3.1 Transient Flow Equation

Transient flow occurs during the early life of the reservoir when boundary effects have not been felt (Figure 6). For very tight formations, such as shale, this flow period can last for months or years.

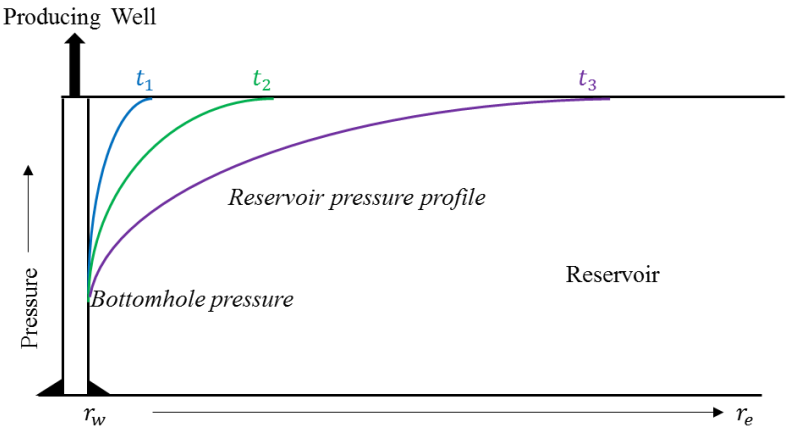

Figure 6 – Illustration of transient flow period. At this time, the effect of the boundary has not yet been felt and the well is under infinite-acting radial flow.

The transient flow equation for natural gas reservoirs with pseudopressure $[m(p)]$ can be described as in Eq. 2.42.

$$q_{gsc} = \frac{kh[m(p_i) - m(p_{wf})]}{1638T_R}\left[\log t + \log\left(\frac{k}{\phi(\mu c_t)_i r_w^2}\right) - 3.23\right]^{-1} \qquad (2.42)$$

where

q_{gsc} = gas flow rate at standard conditions (MSCF/D)

k = permeability (md)

h = reservoir height (ft)

p_i = initial reservoir pressure (psi)

p_{wf} = bottomhole pressure (psi)

T = reservoir temperature (^oR)

t = time (hours)

r_w = wellbore radius (ft)

ϕ = reservoir porosity (fraction)

μ = viscosity (cp)

c_t = total compressibility factor (psi^{-1})

2.3.2 Steady State Flow Equation

The gas well steady-state flow equation is valid for a reservoir with a constant pressure boundary, as illustrated in Figure 7.

`

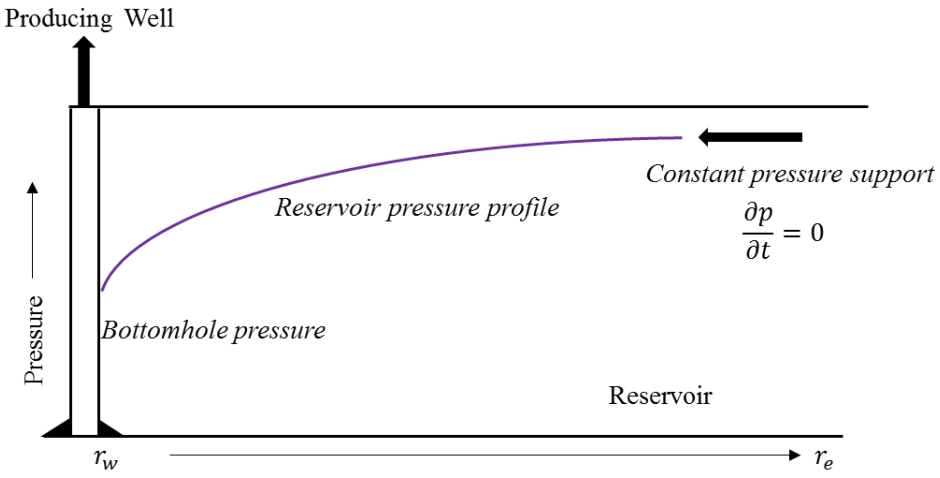

Figure 7 – Illustration of steady-state flow pressure profile. At this time, the well experiences a constant pressure support at the boundary. This pressure support commonly comes from an aquifer or injection wells.

A constant-pressure boundary indicates that the static pressure at the boundary remains constant, providing a simple solution to the gas flow equation as described in this subsection. Applying the correct unit considerations, the gas flow rate equation for a steady-state flow condition can be described as in Eq. 2.43. The definition of average pressure (p_{avg}) is given in Eq. 2.44.

$$q_{gsc} = \frac{kh\left(p_e^2 - p_{wf}^2\right)}{1424\overline{\mu Z}T\left[\ln\left(\frac{r_e}{r_w}\right) + s\right]} \tag{2.43}$$

$$p_{\text{avg}} = \frac{p_e + p_{wf}}{2} \tag{2.44}$$

where

$\bar{\mu}$ = viscosity (cp) evaluated at p_{avg}

$\bar{Z}$ = compressibility factor (dimensionless) at p_{avg}

r_e = reservoir radius (ft)

s = skin factor (dimensionless)

p_e = reservoir pressure (psi)

The evaluation of gas viscosity and compressibility at p_{avg} is an approximation. However, these gas properties are very dependent on pressure. We can use the definition of the pseudopressure for real gas $m(p)$, described in section 2.3.4, to better evaluate the gas properties. The equation for gas steady-state flow, with real gas pseudopressures, can be written as Eq. 2.45.

$$q_{gsc} = \frac{kh\left[m(p_e) - m\left(p_{wf}\right)\right]}{1424T\left(\ln\left(\frac{r_e}{r_w}\right) + s\right)} \tag{2.45}$$

2.3.3 Pseudosteady-State Flow Equation

The pseudosteady-state flow equation assumes that the pressure transient has reached the boundaries of the reservoir and that the pressure at the boundary is decreasing uniformly throughout the reservoir (Figure 8). The pseudosteady-state equation with pseudopressure for gas flow is provided in Eq. 2.46. Note that the main difference between steady-state and pseudosteady-state flow is the use of the average reservoir pressure ($\bar{p}$) in the calculation of pseudosteady state. This work assumes the pseudosteady-state flow for gas inflow. This pseudosteady-state equation is coupled with results from the CVD.

$$q_{gsc} = \frac{kh\left[m(\bar{p}) - m\left(p_{wf}\right)\right]}{1424\, T_R \left[\ln\left(\frac{r_e}{r_w}\right) + s\right]} \tag{2.46}$$

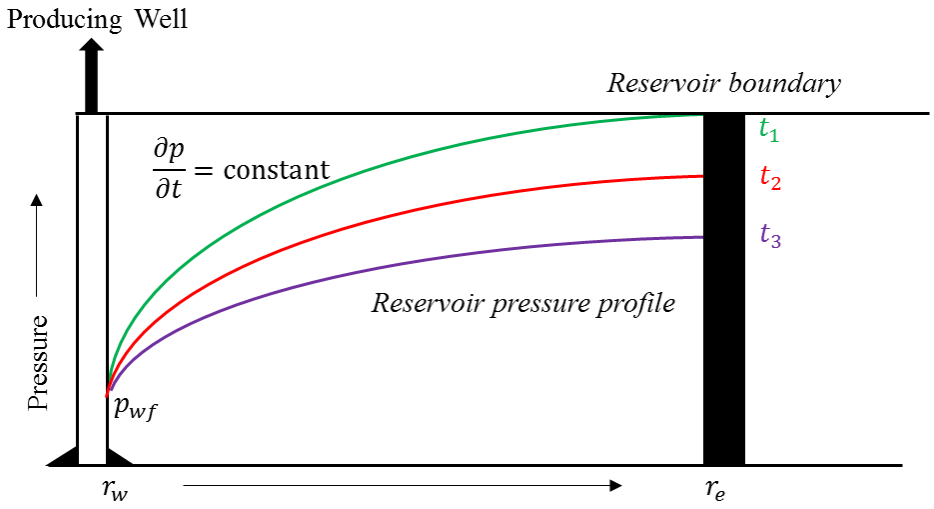

Figure 8 – Illustration of pseudosteady-state flow pressure profile. At this time, the effects of the outer boundary have been felt. The outer boundary prevents the flow fluid from into the reservoir.

2.3.4 Real-Gas Pseudopressure

Al-Hussainy and Ramey (1966) developed the concept of the real-gas pseudopressure that can be used in the radial gas flow equation. The real-gas pseudopressure is significant because gas properties—viscosity and compressibility—are strongly dependent on pressure. This new concept led to improvement in forecasting gas production due to better accuracy in predicting the pressure-dependent gas properties. The real-gas pseudopressure is defined in Eq. 2.47.

$$m(p) = 2\int_{p_o}^{p} \frac{p}{\mu Z} dp \tag{2.47}$$

The trapezoidal rule for numerical integration presented in Eq. 2.48 is used to program the pseudopressure in the model.

$$m(p) = 2\sum_{j=2}^{k} \frac{1}{2}\left[\left(\frac{p}{\mu Z}\right)_{j-1} + \left(\frac{p}{\mu Z}\right)_{j}\right](p_j - p_{j-1}) \tag{2.48}$$

In Eq. 2.43, k is the number of intervals between the pressure values p_o and p, while j denotes the intermediate calculation steps. Dake (1978) explained that if drawdown is very large, the pseudopressure method is more accurate in the flow calculations. In this work, I divided the range from p_o to p into 10 intervals, although the equation can be adjusted to accommodate larger pressure ranges. By doing this, I properly calculated the real-gas pseudopressures to be used in the radial flow equation. The viscosity (μ) and compressibility factor (Z) are calculated using the Peng-Robinson EOS and viscosity correlation previously mentioned.

2.3.5 Fracture as Equivalent Skin

Hydraulic fracturing completion is necessary to produce hydrocarbons from tight reservoirs. The impact of hydraulic fracture completions can be incorporated in the inflow equation as an equivalent skin effect (Prats 1961). This characterization of a hydraulic

fracture completion as an equivalent skin factor is associated with the fracture half-length (x_f) and dimensionless fracture conductivity (C_{fD}) of the hydraulic fracture (Eq. 2.54).

First, we introduce the concept of effective wellbore radius. The effective wellbore radius (r_w') can be defined as a relation of wellbore radius (r_w) to the skin factor (s_f), as in Eq. 2.49.

$$r_w' = r_w e^{-s_f} \tag{2.49}$$

Solving Eq. 2.49 for the skin factor, we can describe the skin factor as in Eq. 2.50.

$$s_f = -\ln\left(\frac{r_w'}{r_w}\right) \tag{2.50}$$

Prats (1961) proved that the effective wellbore radius generates a production behavior similar to a fractured well. He concluded that for high-conductivity fractures (C_{fD} approaching infinity) with small fracture penetration ratios (I_x approaching zero), the effective wellbore radius is half of the fracture half-length (Eq. 2.52), as illustrated in Figure 9. The penetration ration (I_x) is defined in Eq. 2.51.

$$I_x = \frac{x_f}{x_e} \tag{2.51}$$

$$r_w' = \frac{x_f}{2}\Big|_{\substack{C_{fD}\to\infty \\ I_x\to 0}} \tag{2.52}$$

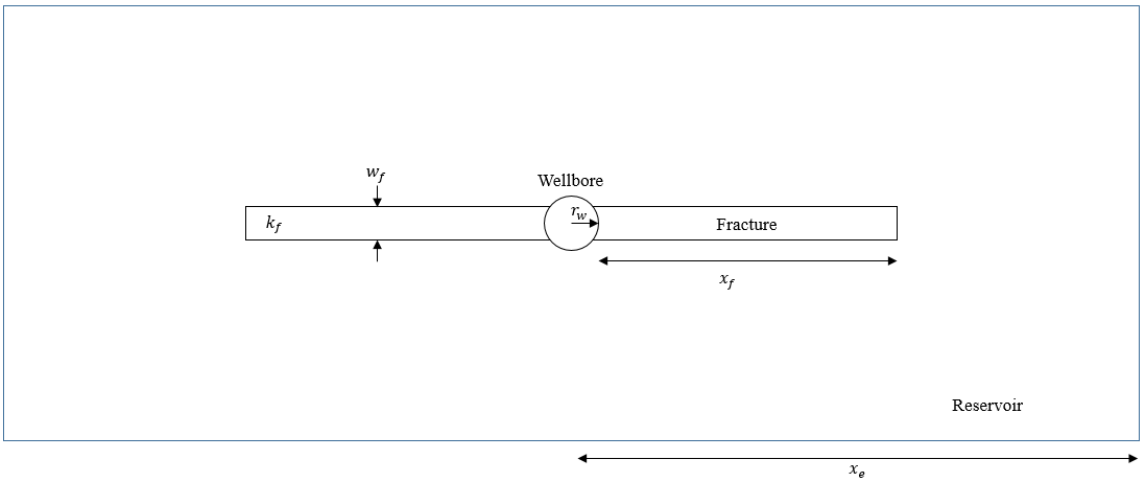

Figure 9 – Illustration of vertical fracture. Here, the wellbore radius is represented as r_w, the fracture half-length (x_f), and the reservoir half-length (x_e). The penetration ratio (I_x) is a ratio between the fracture and reservoir half-length as defined in Eq. 2.51.

Meyer and Jacot (2005) expanded this work and presented a simple analytical model for hydraulic fractures with finite-conductivity as an effective wellbore radius (r'_w), as in Eq. 2.53. The effective wellbore radius is defined using the dimensionless fracture conductivity that was introduced by Agarwal et al. (1998) and Cinco-Ley and Samaniego (1981), defined in Eq. 2.54. Typical values for finite-conductivity fractures are C_{fD} less than 300 (Economides et al. 2012) with the fracture flow capacity ($k_f w_f$) term less than 10,000 md-ft.

$$r'_w = \frac{x_f}{\frac{\pi}{C_{fD}} + 2} \tag{2.53}$$

$$C_{fD} = \frac{k_f w_f}{k x_f} \tag{2.54}$$

Using the relationships for effective wellbore radius (Eq. 2.53) and dimensionless conductivity (Eq. 2.54) and substituting them into the definition of equivalent skin factor in Eq. 2.50, we obtain Eq. 2.55. This concept of equivalent skin (s_f) does not apply when

the fracture half-length (x_f) approaches the well drainage area (r_e). Using this equation, we can model the fracture as an equivalent skin factor in the flow equations presented previously.

$$s_f = -\ln\left(\frac{\frac{x_f}{\frac{\pi}{C_{fD}}+2}}{r_w}\right) \tag{2.55}$$

where

k = reservoir permeability (md)

x_f = fracture half-length (ft)

k_f = fracture permeability (md)

w_f = fracture width (ft)

r_w = wellbore radius (ft)

r_w' = effective wellbore radius (ft)

C_{fD} = dimensionless fracture conductivity

s_f = dimensionless skin factor

I_x = fracture penetration ratio

x_e = drainage half-length (ft)

2.4 Adsorption and Relative Permeability

The mechanistic model in this work considers the impact of adsorption and relative permeability that occurs in the reservoir. The incorporation of these phenomena is explained in the following sections.

2.4.1 Adsorption Modeling

Shale resources have much smaller pores than conventional reservoirs (<100 nm). Wall/molecule interaction effects that result from the adsorption of hydrocarbon

molecules to the pore wall in shale reservoirs must be taken into account to properly model production.

I used the extended Langmuir (Kapoor et al. 1990) model to analyze the impact of multicomponent hydrocarbon mixture adsorption. This adsorption model is popular in the industry and simple to use, but it is thermodynamically inconsistent (Tóth 2003), as explained further in the following sections.

Langmuir Adsorption

Langmuir (1918) proposed an adsorption isotherm that varies with pressure and temperature. The Langmuir adsorption isotherm (Eq. 2.56) assumes a monolayer and describes single-component adsorption on a solid surface.

$$G_a^L = G_{sL}\frac{p}{1+p_L} \tag{2.56}$$

This adsorption model is easily calculated and popular in the petroleum industry to account for adsorbed gas. However, the monolayer assumption of the Langmuir isotherm is only valid in low pressures and causes thermodynamic inconsistency for high pressures. The monolayer assumption indicates that there is a finite number of molecules that is able to adsorbed to the solid surface. However, in the limiting case of equilibrium pressure nearing infinity, the finite number of molecules adsorbed cannot be proven, and is thus inconsistent with the Gibbs thermodynamics (Tóth 2003).

Extended Langmuir Adsorption Model

Kapoor et al. (1990) developed the extended Langmuir (EL) model for gas mixtures. This model is presented in Eq. 2.57. The Langmuir pressure and volume parameters are obtained from adsorption data of pure components through laboratory experiments. In a multicomponent adsorption system, the EL model assumes that each component competes

for the same adsorption site, rather than adsorbing independently. The total gas adsorbed is the summation of each component adsorbed in the monolayer.

$$G_a^{EL} = \sum_{i=1}^{N_c} G_{sL_i} \frac{y_i p}{p_{L_i}\left(1 + \sum_{j=1}^{N_c} y_j \frac{p}{p_{L_j}}\right)} \tag{2.57}$$

where

G_a^{EL} = adsorbed gas amount (scf/ton) using the EL model

G_{sL_i} = Langmuir volume coefficient of component i (scf/ton)

p_{L_i} = Langmuir pressure coefficient of component i (psia)

N_c = number of components

p = pressure (psia)

y_i = mole fraction of component i in the gas phase

Multicomponent Adsorption in Pore Space

Ambrose et al. (2012) argued that we must account for the presence of adsorbed molecules in shales. Since the adsorbed molecules are stored at a higher density than free gas, the amount of natural gas storage can be significant. They also assume that there is a fraction of the pore volume occupied by the adsorbed molecules, resulting in less void space for free molecules. This concept is illustrated in Figure 10, where the adsorbed gas is occupying a portion of the total void volume, decreasing the amount of void space left for the free gas.

Ambrose et al. (2012) developed a volumetric method which accounts for pore volumes occupied by adsorbed gas. Initially, the volumetric model only considers a single-component Langmuir adsorption model. Their work continued to incorporate multi-component adsorption with the extended Langmuir (Ambrose et al. 2011). Hartman et al. (2011) considered the thermodynamically-consistent ideal adsorbed solution (IAS) model

in place of the thermodynamically inconsistent EL model in their gas-in-place calculation. They found only marginal impact on the resulting data when compared with the EL model.

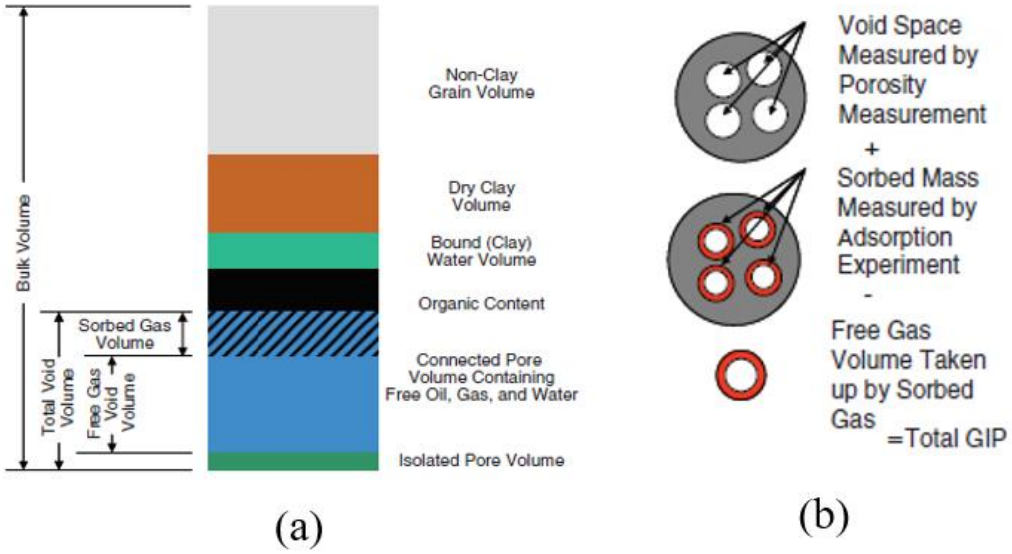

Figure 10 – a) Volumetric constituents of a typical gas-shale matrix; the hatched region describes the interplay between the adsorbed and total porosity (void volume), b) The volumetric concept of adsorbed molecules decreasing space for free gas to occupy (modified from Ambrose et al. (2012)).

Following the illustration in Figure 10, Ambrose et al. (2011) indicate that the total initial gas in place (G_t) can be described mathematically as the summation of free gas (G_f) and adsorbed gas (G_a), as shown in Eq. 2.58. The total gas adsorbed (G_a) is determined from Eq. 2.57. The proposed volumetric gas-in-place formula, with multicomponent adsorbed gas consideration, is described as Eq. 2.59. The constant 32.0368 is the conversion factor from cc/g to scf/ton.

$$G_t = G_f + G_a \tag{2.58}$$

$$G_t = 32.0368\frac{\phi(1-S_w)-\phi_a^{EL}}{\rho_b B_g} + \sum_{i=1}^{n} G_{sL_i}\frac{y_i p}{p_{L_i}\left(1+\sum_{j=1}^{n} y_j \frac{p}{p_{L_j}}\right)} \tag{2.59}$$

where

G_t = total gas in-place (scf/ton)

ϕ = porosity (fraction)

S_w = water saturation (fraction)

ϕ_a^{EL} = adsorbed porosity fraction using the extended Langmuir model

ρ_b = bulk rock density (g/cc)

B_g = gas formation volume factor (reservoir ft^3/standard ft^3)

G_{sL_i} = Langmuir volume coefficient of component i (scf/ton)

p_{L_i} = Langmuir pressure coefficient of component i (psia)

y_i = mole fraction of component i

p = reservoir pressure (psia)

In Eq. 2.59, the free-gas term accounts for the term ϕ_a proposed by Ambrose et al. (2011) to represent the void space occupied by the adsorbed gas. The adsorbed porosity fraction (ϕ_a) can be calculated using Eq. 2.60. The derivation of the conversion constant 1.318×10^{-6} is explained in Appendix A.

$$\phi_a^{EL} = 1.318\times10^{-6}\widehat{M}\frac{\rho_b}{\rho_{s_{\text{mix}}}}\left[\sum_{i=1}^{n} G_{sLi}\frac{y_i p}{p_{L_i}\left(1+\sum_{j=1}^{n} y_j \frac{p}{p_{L_j}}\right)}\right] \tag{2.60}$$

The adsorbed porosity fraction is calculated using an estimate of the mixture density ($\rho_{s_{\text{mix}}}$), shown in Eq. 2.61. Ambrose et al. (2011) recommended using the definition of the van der Waal's co-volume (b) that is shown in Eq. 2.62 to estimate the adsorbed phase density. Furthermore, they suggested using the pseudocritical pressure (p_{pc}) and

temperature (T_{pc}) to estimate b_{mix}. Calculations of T_{pc} and p_{pc} are done using Eq. 2.38 and Eq. 2.39. In this project, I used the linear mixing rule (Eq. 2.9) to calculate b_{mix}.

$$\rho_{s_{mix}} = \frac{\widehat{M}}{b_{\text{mix}}} \tag{2.61}$$

$$b^{\text{vdW}} = \frac{RT_c}{8p_c} \tag{2.62}$$

where

$\rho_{s_{\text{mix}}}$ = adsorbed density of mixture

$\widehat{M}$ = mixture molecular weight

b_{mix} = mixture co-volume b calculated using the mixing rule

b^{vdW} = van der Waal's co-volume

In this study, I considered the use of co-volume definition from Peng-Robinson (Eq. 2.3). Furthermore, we use the mixing rule (Eq. 2.9) to calculate b_{mix}. I found that using the Peng-Robinson co-volume definition results in a higher adsorbed-phase density. This higher density leads to a larger quantity of gas in place than using van der Waal's co-volume. This is shown in the multicomponent adsorption example presented later in this subsection.

As noted previously, the consideration of multicomponent adsorption is important to the estimation of adsorbed and free gas in the shale resource. Ambrose et al. (2011) compared the gas-in-place calculations considering multicomponent adsorption with a single-component (methane) adsorption assumption. The multicomponent adsorption leads to higher gas-in-place calculation than the single-component adsorption model. However, though the multicomponent model leads to larger gas capacity, the free gas capacity of the multicomponent model is lower than the single-component model.

Example Case

An example of the gas-in-place calculation using the EL multi-component adsorption calculation uses a synthetic gas composition (Table 3) and reservoir properties summarized in Table 4.

Table 3 – Composition of typical shale gas synthetically created based on Ambrose et al. (2011).

Component	z_i
C_1	0.86
CO_2	0.01
C_2	0.10
C_3	0.02
C_4	0.01

Table 4 – Example shale reservoir parameters. This is a synthetic case for extended Langmuir calculations.

Parameter	Value	
S_w	0.35	
ϕ	0.055	
p_{res}	4000	psia
T_{res}	180	°F
$Z_{initial}$	0.93204	
B_g	0.0042	ft^3/scf
ρ_b	2.5	g/cc

The Langmuir parameters (G_{sL} and p_L) are necessary in the calculation of the adsorbed gas. Langmuir parameters for small carbon chains are obtained from the literature. However, these measurements are less common for higher carbon chains. To estimate the Langmuir parameters for higher carbon chains, Ambrose et al. (2011) created an empirical formula for the Langmuir volume (Eq. 2.63) and Langmuir pressure in (Eq. 2.64). This empirical formula is based on the relationship of the Langmuir parameter with the carbon number (C_n) of the pure hydrocarbon component (Figure 11). The G_{sL} value presented in Table 5 is for a reservoir of 4% total organic carbon (TOC).

$$G_{sL} = 1537.5C_n + 358.33 \quad (2.63)$$

$$p_L = -359C_n + 1790.3 \quad (2.64)$$

Table 5 – Langmuir parameters for common shale gas at 180ºF and 4% TOC. Only the C_4 Langmuir volume and Langmuir pressure are estimated from the empirical relationship in Eq. 2.63 and Eq. 2.64, respectively Ambrose et al. (2011).

Component	G_{sL} (4% TOC) scf/ton	p_L psia
C_1	56	1562
C_2	91	811
C_3	179	844
C_4^*	*232	*355
CO_2	145	836

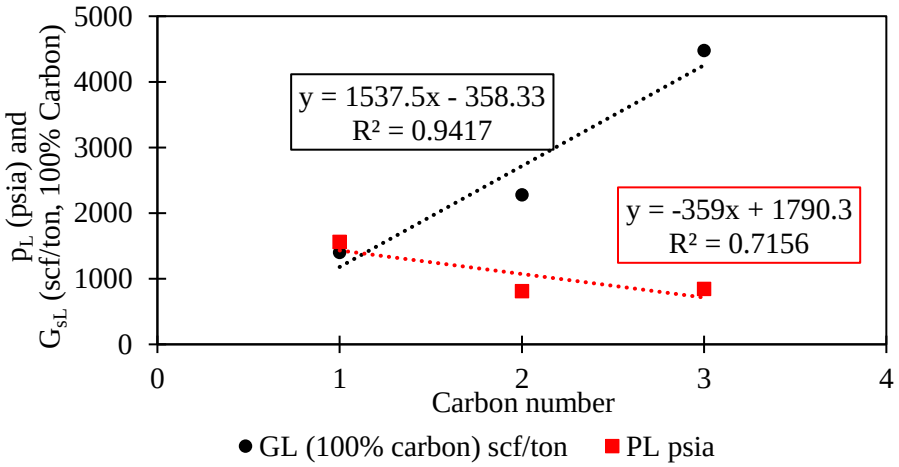

Figure 11 – Langmuir Parameter (G_{sL} and p_L) versus the carbon number of hydrocarbons. The empirical relationships were created by Ambrose et al. (2011) to estimate Langmuir parameters for butane. G_{sL}s are measured at 180ºF on a pure carbon surface.

Once suitable values for Langmuir volume and Langmuir pressure are established, we calculate the adsorbed gas amounts using Eq. 2.57. Figure 12 shows the EL adsorption

model for the gas sample. From this graph, we can derive information about the composition of the multi-component adsorbed phase (Table 6). The majority of the adsorbed component is methane (C_1), followed by ethane (C_2). It is interesting to note here that the adsorbed composition has very low CO_2 composition. Studies have indicated that carbon dioxide adsorbs more preferentially than methane (Gensterblum et al. 2014; Orr 2004).

Table 6 – Adsorbed-phase composition from synthetic shale gas example derived from the extended Langmuir adsorption model.

Component	Adsorbed Phase Composition
C_1	0.5654
CO_2	0.0317
C_2	0.2058
C_3	0.0775
C_4	0.1195

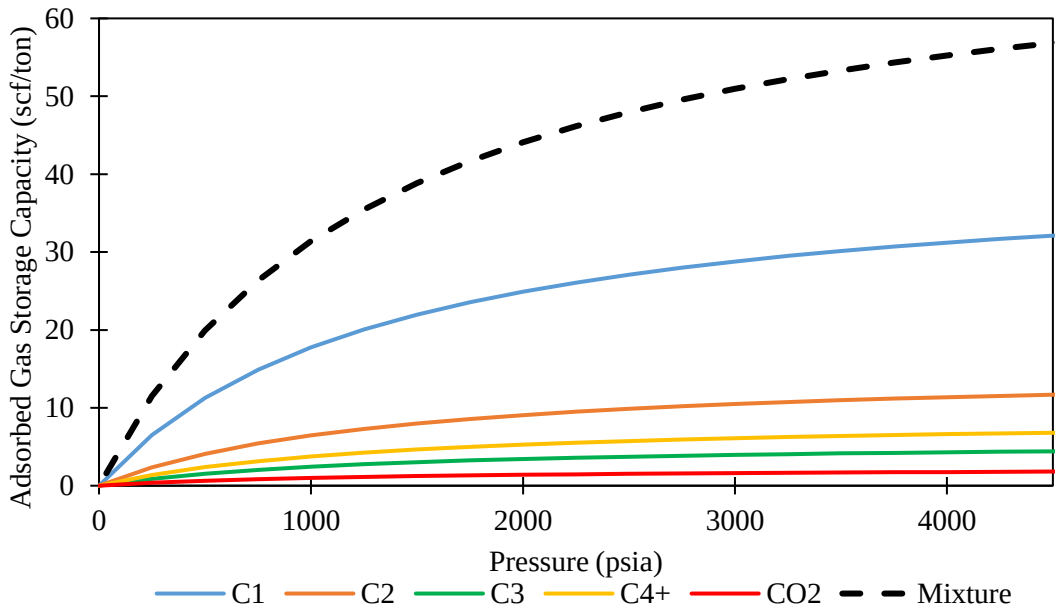

Figure 12 – Extended Langmuir adsorption model example created using properties of synthetic shale gas sample. Methane makes up most of the adsorbed composition in this synthetic example case.

Figure 13 illustrates the differences between the multicomponent and single-component adsorption assumption when calculating adsorbed gas amounts using the Langmuir model. We found that the single-component methane assumption estimates an adsorbed amount lower than the multicomponent assumption, decreasing the gas storage capacity of the rock.

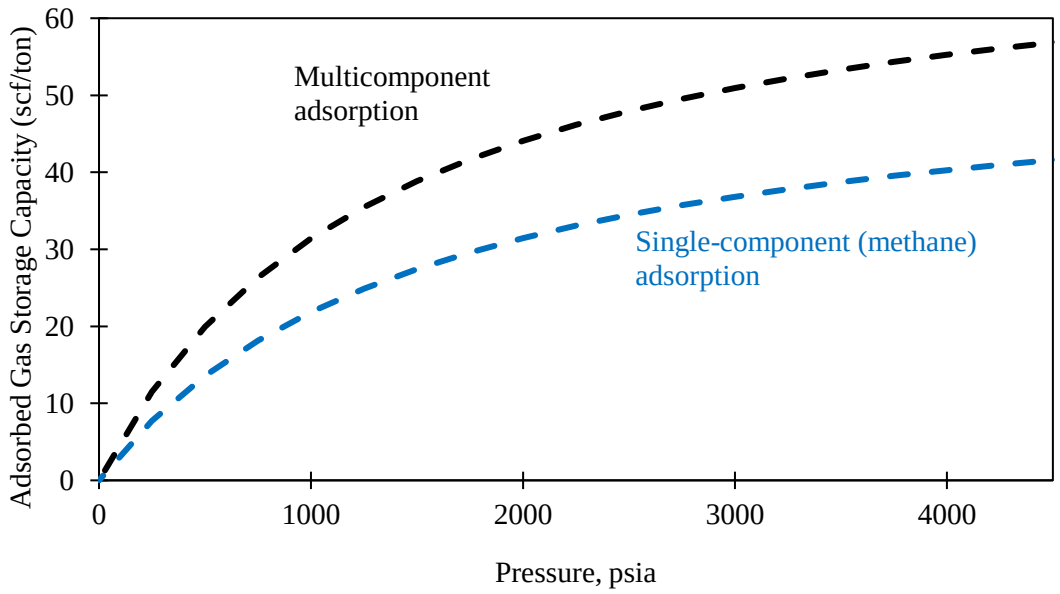

Figure 13 – Amount of gas adsorbed using the Langmuir model used for single-component and multi-component assumption. The single-component adsorption assumption results in a lower amount of gas adsorbed than using the multicomponent extended Langmuir model.

The total gas-in-place calculation was done using Eq. 2.59 and the results appear in Table 7. Comparing the total gas-in-place results, accounting for adsorption leads to a higher gas-in-place value than without adsorption. Also, incorporating the multicomponent adsorption leads to higher estimation of gas in place than only considering single-component methane adsorption. These calculations show the significance of adsorption on gas-in-place calculation.

As noted previously, the estimation of adsorbed phase density can be done using the molar volume divided by the co-volume. The co-volume definition can be provided by van der Waal's (vdW), presented in Eq. 2.62, or Peng-Robinson (PR), presented in Eq. 2.3. As stated previously, the mixture co-volume was calculated using the mixing rule (Eq. 2.9).

The PR co-volume (b) for adsorbed-density estimation results in a higher density value than the vdW co-volume. The higher density (ρ_s) estimation from the PR co-volume leads to a lower adsorbed porosity fraction (ϕ_a). The lower adsorbed-porosity fraction allows for greater space for free gas (G_f), and thus a larger value of total gas in place (G_t). In this work, we considered the PR co-volume definition (Eq. 2.3) to estimate the density of the adsorbed phase.

Table 7 – Results of calculation of gas in place using different adsorption assumptions and density calculation methods.

Assumptions	ρ_s (g/cc)	$\hat{M}_{ads}$ (lb/lb$_{mole}$)	ϕ_a (%)	G_t (scf/ton)	G_f (scf/ton)	G_a (scf/ton)
no adsorption	0	0	0	109.08	109.08	0.0
single component methane (vdW)	0.371	16	0.57	131.89	91.62	40.3
single component methane (PR)	0.596	16	0.36	138.48	98.21	40.3
multi-component EL (vdW)	0.449	26.98	1.09	130.94	75.69	55.2
multi-component EL (PR)	0.721	26.98	0.68	143.54	88.30	55.2

Further Discussion on Adsorbed Porosity Fraction

Ambrose et al. (2011) proposed a calculation to estimate the adsorbed pore fraction (ϕ_a) described in Eq. 2.60. They suggest that the pore space available for free gas should be decreased by subtracting ϕ_a from the total porosity. However, from the calculations in the previous chapter, values for the adsorbed porosity term seem rather high, causing significant decrease in free gas volume. Furthermore, the calculation of adsorbed volume is based on the Langmuir model, which assumes a monolayer adsorption. The monolayer assumption contributes to skepticism towards the value of ϕ_a. Also, the proposed formula

for ϕ_a in this calculation does not depend on pore size, which has a relation to the amount of adsorbed molecule.

Considering the assumption of the monolayer in the Langmuir and EL models, I did a simple calculation to check the amount of pore space that would be taken up by the adsorbed phase. The calculation is based on the size of a methane molecule (0.414 nm) and the size of shale pore diameter, 10 nm and 100 nm for the low and high cases, respectively (Nelson 2009), as shown in Figure 14. For this calculation, I assumed a cylindrical shape of unit height (Figure 15).

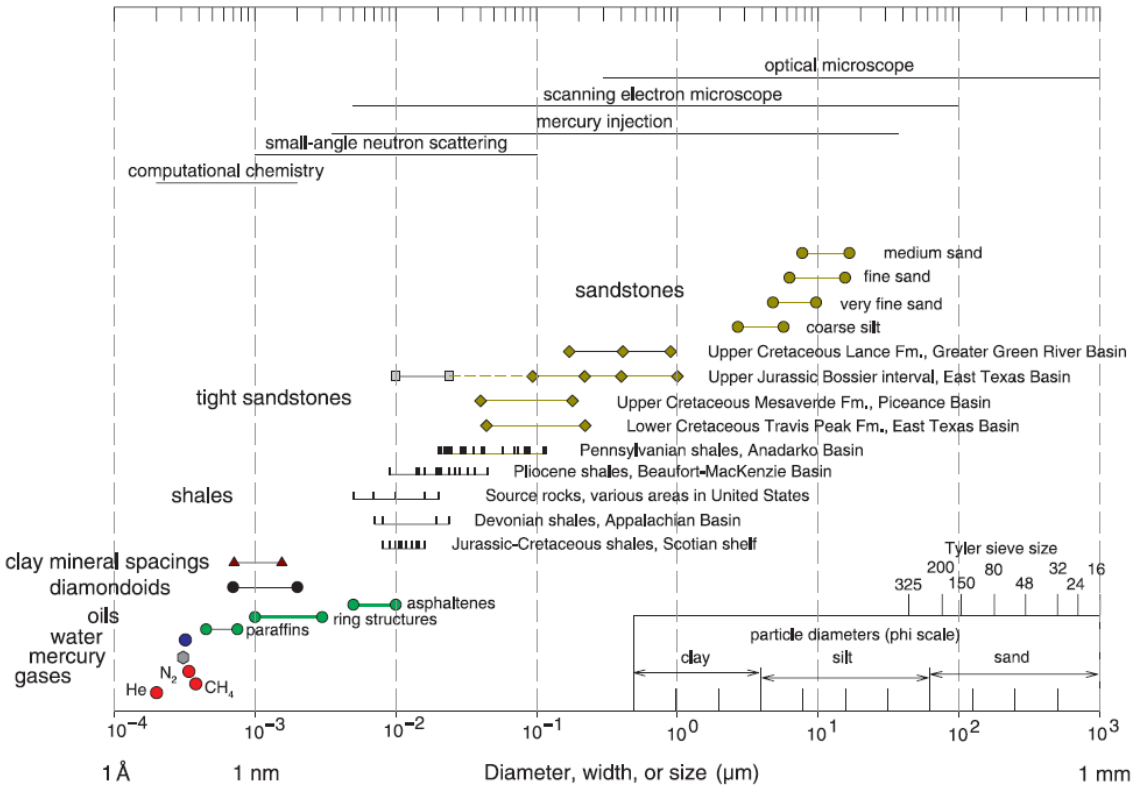

Figure 14 – Sizes of molecules and pore throats in different types of rocks (Nelson 2009). The diameter of methane is 0.414 nm. The diameter for shale is taken to be 10 nm and 100 nm for the low and high cases, respectively.

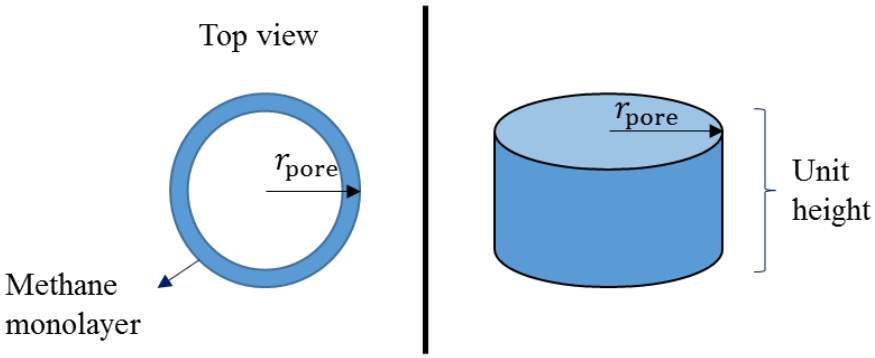

Figure 15 – Illustration of simple pore concept for monolayer calculation.

I calculated the pore volume reduction due to methane molecules adsorbed to the pore wall with Eq. 2.65.

$$V_{\text{free}} = \pi h\left(r_{\text{pore}} - D_{C_1}\right)^2 \tag{2.65}$$

where

V_{free} = volume of pore space for free gas

π = constant 3.142

h = unit height of 1

r_{pore} = radius of pore, taken to be 10 nm and 100 nm

D_{C_1} = diameter of methane, 0.414 nm

The results from this calculation are tabulated in Table 8. Furthermore, we calculated the theoretical adsorbed pore fraction considering the Langmuir monolayer assumption for a range of porosities (Table 9).

Table 8 – Result of pore volume reduction from adsorbed monolayer for shale pore throat size.

Pore Radius (nm)	Total Pore Volume (unit volume)	Pore Volume (free)	Monolayer (adsorbed) Volume (unit volume)	Volume Reduction (%)
100	31416	31156	260	0.83
10	314	289	26	8.11

Table 9 – Comparison of actual porosity and free-gas porosity for shale pore throat diameter of 10 nm and 100 nm. The effect of adsorption decreases with increasing pore size.

Actual Porosity	10-nm pore throat			100-nm pore throat		
	Bulk Volume (unit volume)	Porosity (free)	ϕ_a	Bulk Volume (unit volume)	Porosity (free)	ϕ_a
5%	6,283	4.59%	0.405%	628,319	4.96%	0.041%
6%	5,236	5.51%	0.487%	523,599	5.95%	0.050%
`7%	4,488	6.43%	0.568%	448,799	6.94%	0.058%
8%	3,927	7.35%	0.649%	392,699	7.93%	0.066%
9%	3,491	8.27%	0.730%	349,066	8.93%	0.074%
10%	3,142	9.19%	0.811%	314,159	9.92%	0.083%

Comparing the values obtained from this calculation with the values obtained using the method from Ambrose et al. (2011), we see that the latter method may only be valid for very small pores, around 10 nm. For pores larger (100 nm), we see method overestimates the pore space taken by the adsorbed molecules.

From the results, we can conclude that the reduction in pore space for free gas is more significant in the smaller pores. However, the significance of the pore reduction due to the adsorbed monolayer decreases in the larger pore throats. The mechanistic production model in this work does not include the pore size. In Chapter IV, the reservoir model used to validate this work is in the sandstone order, so the adsorbed porosity fraction is negligible.

2.4.2 Relative Permeability

Relative permeability is a concept that quantifies fractional flow phenomena occurring in multiphase flow systems. In this study, liquid (oil) and gas are the coexisting phases. The relative permeability is affected by various factors, including wettability and fluid saturation. This concept is represented by the relative permeability curve as a function of

the saturation of the reference fluid. The relationship between relative permeability (k_r), effective permeability (k_{eff}), and absolute permeability (k_{abs}) is shown in Eq. 2.66.

$$k_{\text{abs}} = \frac{k_{\text{eff}}}{k_r} \tag{2.66}$$

The absolute permeability is measured in the presence of a single-phase fluid flow. The effective permeability is used in the flow equation in the presence of multiphase flow. Based on the saturation of the CVD cell, we can adjust the production of the fluids (oil and gas) in accordance with the relative permeability curve.

Brooks-Corey Relative Permeability Model

The Brooks and Corey (1964) relative permeability model is presented as an option in the tool developed in this work to modify the CVD simulation. The equation for this model is

$$k_{r_o} = \left(\frac{S_o - S_{or}}{1 - S_{or}}\right)^{\frac{2+3\lambda}{\lambda}} \tag{2.67}$$

$$k_{r_g} = \left(\frac{1 - S_o}{1 - S_{or}}\right)^2 \left[1 - \left(\frac{S_o - S_{or}}{1 - S_{or}}\right)^{\left(\frac{2+\lambda}{\lambda}\right)}\right] \tag{2.68}$$

where k_{ro} is the relative permeability to oil (fraction), k_{rg} relative permeability to gas (fraction), S_o saturation of oil, S_{or} residual oil saturation, and λ the pore size distribution parameter. For narrow pore size distributions, λ is greater than 2, and for wide distributions, λ is less than 2. For studies in the Eagle Ford, values of 2.5 to 4.5 have been used to model the relative permeability (Honarpour et al. 2012; Whitson and Sunjerga 2012).

Using this model, I obtained a relative permeability curve of oil and gas (Figure 16**)**. By applying the relative permeability curves, I scaled the production of the existing fluids

based on their saturations. This incorporation assists in achieving an accurate forecasting result.

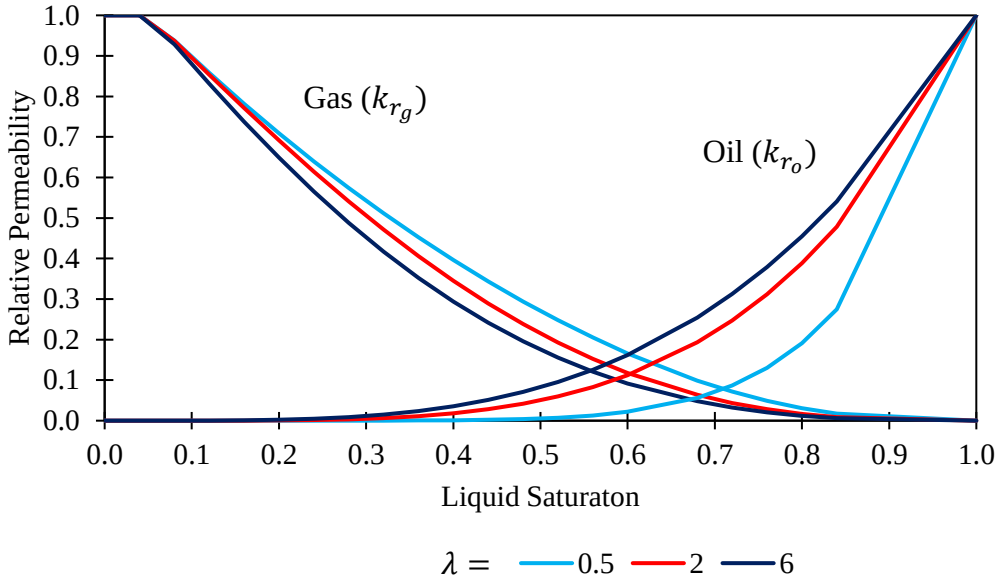

Figure 16 – Brooks and Corey (1964) relative permeability curve λ = 0.5, 2, and 6 and S_{or} = 0.05.

2.5 Software Used

Three main software packages used in this study are Microsoft Excel, VBA, ECLIPSE, and PVTi. Microsoft Excel supports programming through Microsoft's Visual basic for Applications (VBA). VBA enables the user to build user-defined functions and manipulate Excel spreadsheets. The relative ease of access and use of this software makes it ideal to conduct the study detailed in this work.

ECLIPSE (Schlumberger 2014) is a commercial numeric reservoir simulator. This simulator, which has the option to simulate reservoir models as black oil or compositional fluids, was used to validate the mechanistic model developed in this research. The

numerical reservoir simulator is governed by mass and energy conservation laws and fluid flow through porous media. Fluid equations-of-state and vapor/liquid equilibrium calculations were used in the compositional simulation.

PVTi is a commercial pressure/volume/temperature simulator (Schlumberger 2014). With PVTi, the user can define the composition of a fluid and conduct experiments including constant composition expansion (CCE), constant volume depletion (CVD), differential liberation (DL), etc. As a part of a reservoir simulation package, PVTi provides the user with an easy way to characterize the reservoir fluid compositionally for use in the compositional reservoir simulator. PVTi was used to validate the programed CVD simulation created in this study.

CHAPTER III

CONSTANT VOLUME DEPLETION (CVD)

This chapter presents the development of the constant volume depletion simulation in Microsoft Excel VBA. This test imitates the production of gas-condensate reservoirs and volatile oils from pressure depletion and gas expansion. As part of this research project, I programmed an algorithm to simulate a CVD test. The backbone of this simulation was a program written as a molar accounting process that combines vapor/liquid-equilibrium calculation and material balance. The results of the CVD test were validated with a commercial PVT simulator and showed good agreement.

In the second half of this chapter, we describe the modifications made to the new CVD test. The modifications include the ability to initialize the CVD test above saturation pressure and production of liquid with gas. These alterations to the programmed CVD test were necessary to mimic the fluids production from a gas-condensate reservoir. The CVD algorithm derived in this chapter provides the material balance basis for forecasting deliverability.

3.1 CVD Test in VBA

To simulate the CVD test in VBA, I broke down the CVD process into programmable parts. In essence, the constant volume depletion process requires four calculations to determine each pressure decrement:

1. Vapor/liquid-equilibrium
2. Fluid production to maintain constant volume
3. Remaining fluid recombination
4. Pressure decrement

These calculations can be repeated until a specified ending pressure is reached. The calculations conducted on each part are presented in this section.

As an initial step, the CVD simulation requires an input for initial fluid composition, total moles, and temperature. As with the CVD test conducted in the laboratory, the simulation begins at the dewpoint of the fluid sample. Beginning with information on composition (z_i), temperature (T), and pressure (p), the process simulates the CVD as a molar accounting process. The number of total, liquid, and gas moles are tracked throughout the CVD simulation.

3.1.1 Vapor/Liquid Equilibrium Calculation

The vapor/liquid-equilibrium calculation defines the properties of the fluid. First, the VLE is calculated with the PR EOS as described in 0. From the VLE, the compressibility factor (Z) and molar fractions of vapor (f_g) and liquid (f_o) are obtained. These values are used to calculate the volume of the existing fluid. The total volume inside the CVD cell is the summation of volume in the liquid and gas phases (Eq. 3.1 and Eq. 3.2). We also calculate viscosity using the Lorentz-Bray-Clark (LBC) correlation previously described.

$$V_t = V_o + V_g \tag{3.1}$$

$$V_t = f_o n_t V_{m_o} + f_g n_t V_{m_g} \tag{3.2}$$

where:

V_t = total volume of fluid

$V_{o,g}$ = volume of liquid (o) or vapor (g) phase

n_t = total moles in cell

$V_{m_{o,g}}$ = molar volume of oil (o) or gas (g) phase

In the initial step, VLE is conducted using the sample fluid composition (z_i), reservoir temperature, and dewpoint pressure. The volume calculated with the initial inputs is used as the reference volume (V_{ref}) for the CVD. The reference volume is kept constant throughout the constant volume depletion process. At this initial stage, the gas condensate exists in a single gas phase.

In the subsequent steps, pressures lower than the dewpoint are used in the VLE calculation. The decrease in pressure allows the charged fluid to expand, leading to a larger total fluid volume. The total volume at pressure step j is denoted as V^j.

3.1.2 Fluid Production

The fluid production step calculates the volume of gas that must be produced to maintain constant volume. This is done using Eq. 3.3 below.

$$V^j_{\text{prod}} = V^j - V_{\text{ref}} \tag{3.3}$$

where

V^j_{prod} = total volume that must be produced at pressure step j

V^j = total volume at pressure step j

V_{ref} = reference volume

Now, we determine the number of moles associated to the volume produced. Since only gas is produced from the PVT cell, the moles of gas produced must be calculated. We compute the produced moles of gas using Eq. 3.4.

$$n^j_{\text{prod}_g} = \frac{V^j_{\text{prod}}}{V^j_{m_g}} \tag{3.4}$$

where

$n^j_{\text{prod}_g}$ = moles gas produced at pressure step j

$V^j_{m_g}$ = molar volume of gas at pressure step j

Then, we calculate the moles produced from each component using Eq. 3.5.

$$n^j_{\text{prod}_g,i} = n^j_{\text{prod}_g}\, y^j_i \tag{3.5}$$

where

$n^j_{\text{prod}_{g,i}}$= moles gas produced at pressure step j from component i

y_i^j = composition of component i in the gas phase

The amount of moles produced, as well as the fluid's composition, are flashed to standard conditions. From this, we obtain the volume of gas and oil produced at standard pressure and temperature. Later, we use the produced volumes information to couple the CVD with the flow equation to create a relationship between volumes produced and time (production forecasting).

Then, the moles of gas produced are subtracted from the total moles of gas for each component (Eq. 3.6). The amount of moles remaining is kept for fluid recombination.

$$n_{g_i}^{j+1} = n_{g_i}^j - n_{\text{prod},i}^j \tag{3.6}$$

where

$n_{g_i}^j$ = moles of gas of component i at pressure step j

Eq. 3.7 and Eq. 3.8 computes the moles of component i in the gas (g) and oil (o) phase, respectively. The calculated moles of each composition is used in the next step, recombination.

$$n_{g_i}^j = n^j \, f_g^j \, y_i^j \tag{3.7}$$

$$n_{o_i}^j = n^j \, f_o^j \, x_i^j \tag{3.8}$$

where

n^j = total moles at pressure step j

f_g^j = molar fraction of vapor/gas at pressure step j

f_o^j = molar fraction of vapor/gas at pressure step j

x_i^j = composition of component i in the liquid phase

In summary, the information gathered from this production step includes the number of moles and composition of fluid produced and remaining. The flash calculation is used to calculate the volumes produced at standard conditions based on the moles produced. With the calculated composition and moles of the remaining fluid, we proceed to recombine the fluid for the next pressure step.

3.1.3 Fluid Recombination

The objective of recombination is to provide a new fluid composition input for the next VLE calculation. The fluid recombination is a simple addition of the remaining moles of each component. The moles remaining after production at pressure step $j+1$ is given by Eq. 3.9.

$$n_i^{j+1} = n_{g_i}^{j+1} + n_{o_i}^{j+1} \tag{3.9}$$

where

n_i^{j+1} = total moles of component i at pressure step $j+1$

$n_{o_i}^{j+1}$ = moles of component i in the liquid/oil (o) phase at pressure step $j+1$

In Eq. 3.9, the term $n_{g_i}^{j+1}$ is obtained from Eq. 3.7. In the conventional CVD, the fluid production comes only from the gas phase, while the oil phase remains in the PVT cell. This process is similar to the gas-condensate reservoir, where the main production comes from the gas phase. Thus, the total number of moles for each component in the liquid phase is unchanged. We calculate the moles of component i in the liquid phase using Eq. 3.8. The new fluid composition is calculated using Eq. 3.10.

$$z_i^{j+1} = \frac{n_i^{j+1}}{\sum_{i=1}^{N_c} n_i^{j+1}} \tag{3.10}$$

Through this recombination process, we obtain a new number for total moles (n^{j+1}) and a new fluid composition (z_i^{j+1}).

3.1.4 Pressure Decrement

In the pressure decrement step, we determine the next pressure (p^{j+1}). If the new pressure is above the specified ending pressure, the simulation performs calculations 1 through 4. If the ending pressure is reached, the simulation is terminated and the results printed.

A flow chart summarizing this process is presented in Figure 17. The programmed CVD was validated with a commercial PVT simulator (PVTi). The comparison resulted in an excellent match between the commercial simulator and our in-house simulation.

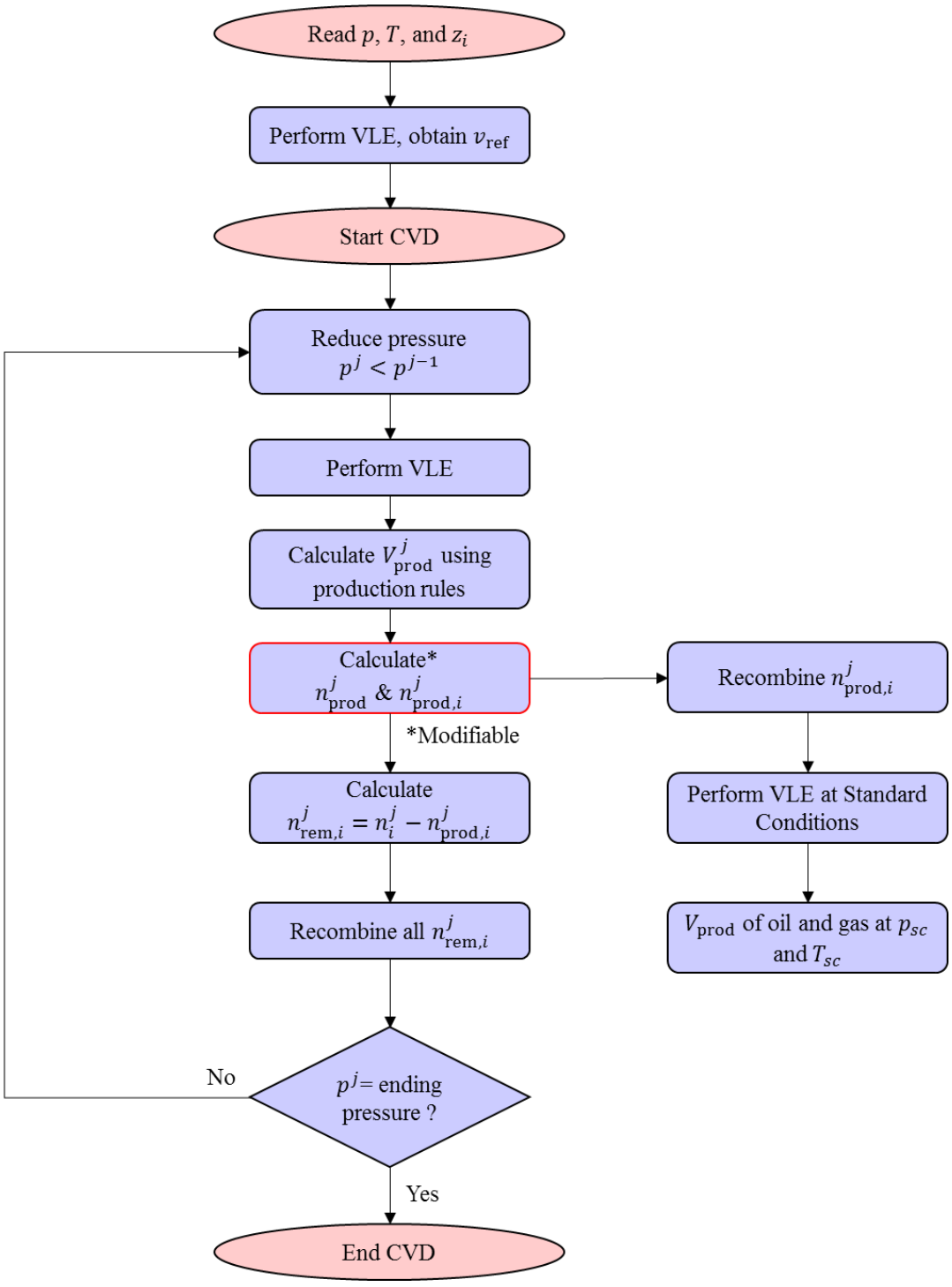

Figure 17 – Conventional constant volume depletion (CVD) simulation workflow implemented in VBA for this study.

3.2 Validation with Commercial PVT Simulator

I compared the constant volume depletion developed in this work to the commercial pressure/volume/temperature software, PVTi (Schlumberger 2014). The gas-condensate fluid composition (z_i) used for the validation is presented in Table 10. This fluid sample (taken from (Gong et al. 2013)) is representative of a fluid from the gas-condensate window of the Eagle Ford resource.

Table 10 – CVD composition used to compare developed CVD and commercial PVTi software. This shows characteristics of an 11 component gas-condensate fluid. The binary interaction parameters are all set to zero.

Component	Molecular Weight	p_c (psia)	T_c (°F)	ω	z_i	s	Z_{crit}	P
C_1	16.0	667.4	-116.9	0.008	65.54	-0.14427	0.28029	77.0
C_2	30.0	708.5	89.7	0.098	12.97	-0.10327	0.27448	108.0
C_3	44.1	615.9	205.6	0.152	6.17	-0.0775	0.28216	150.3
nC_4	58.1	551.3	305.4	0.193	1.50	-0.06198	0.27013	189.9
iC_4	58.1	529.2	274.6	0.176	2.42	-0.05422	0.26914	181.5
nC_5	72.2	489.5	385.3	0.251	1.08	-0.04177	0.29213	268.0
iC_5	72.2	491.0	368.7	0.227	1.02	-0.03028	0.26412	225.0
nC_6	86.0	477.2	453.5	0.275	1.38	-0.00729	0.27412	314.2
N_2	28.0	492.5	-232.8	0.040	0.07	-0.13133	0.28844	41.0
CO_2	44.0	1070.2	87.6	0.225	0.81	-0.04273	0.28419	78.0
C_{7+}	177.1	274.3	782.9	0.536	7.04	0.161911	0.30709	666.8

The phase envelope of the fluid sample is shown in Figure 18. The temperature of the experiment was set at 360°F. The CVD test was conducted from an initial pressure of 4,500 to 1,000 psia with 100-psi incremental pressure steps. The initial pressure of 4,500 psia is above the dewpoint pressure of 3,500 psia. At pressures above the dewpoint, the fluid exists as a single-phase gas. As pressure is decreased and falls below the dewpoint, liquid drops out, resulting in a two-phase fluid (gas and oil).

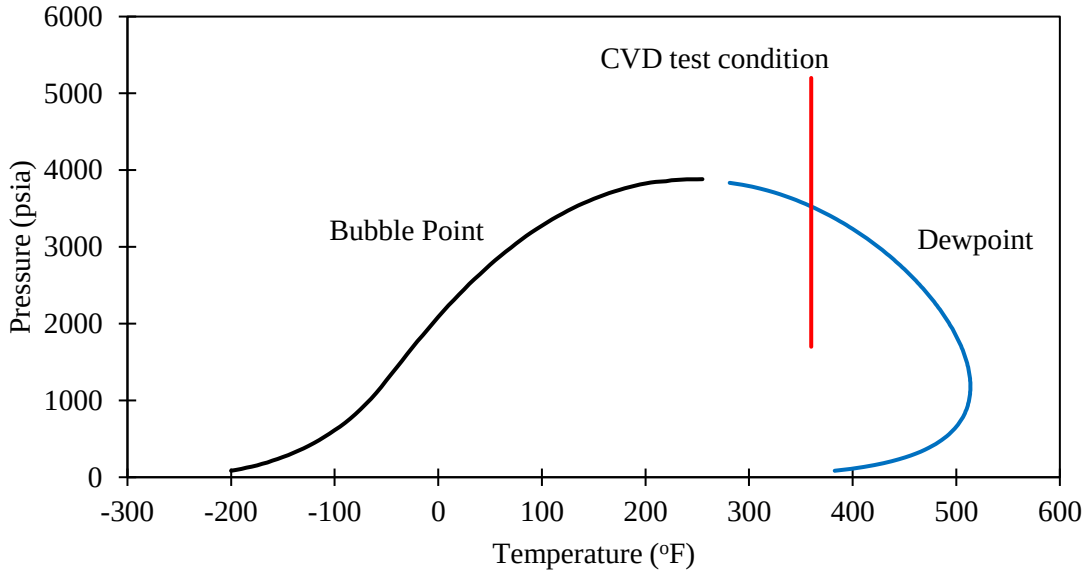

Figure 18 – Phase envelope of fluid mixture described in Table 10. The red line shows the CVD path crossing the dewpoint; thus, the fluid experiences retrograde condensation (liquid dropout). Computed by an in-house simulator developed by Valbuena Olivares (2011).

3.2.1 Comparison of Fluid Properties

The comparison of vapor molar fractions, phase molar volumes, phase compressibility factor (z), phase density, phase viscosity, and composition are shown in Figure 19 through Figure 24 below. The comparison across all of these factors shows great agreement between the CVD simulator developed in this study and the commercial simulator (PVTi). The error comparisons between the developed CVD test and commercial software are tabulated in Table 11. The error values are based on the average error of the properties calculated using Eq. 3.11 and Eq. 3.12.

$$\varepsilon = \frac{\left|\chi^{\mathrm{DEV}} - \chi^{\mathrm{SIM}}\right|}{\chi^{\mathrm{SIM}}} \tag{3.11}$$

$$\bar{\varepsilon} = \frac{\sum_{i=1}^{N} \varepsilon_i}{N} \cdot 100\% \tag{3.12}$$

where

ε = absolute error of value χ

χ^{DEV} = value from this work

χ^{SIM} = value from commercial PVT simulator

$\bar{\varepsilon}$ = average absolute error

N = number of values

Table 11 – Average error between developed CVD simulation and commercial PVT simulator.

	f_v	V_{m_o}	V_{m_g}	Z_o	Z_g	ρ_o	ρ_g	μ_o	μ_g
Developed CVD Error	0.2%	0.1%	0.2%	0.2%	0.3%	0.4%	0.5%	2.3%	0.4%

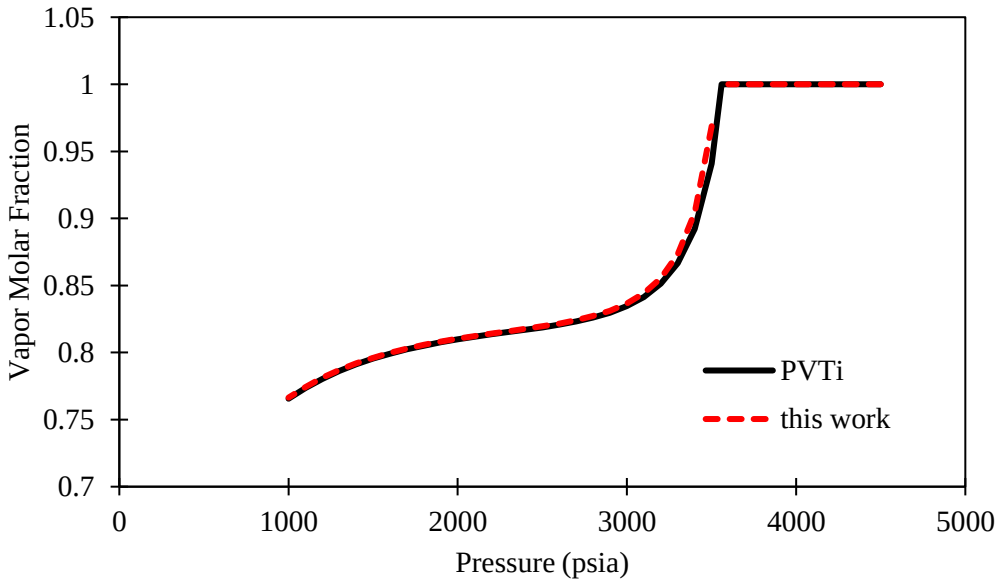

Figure 19 – Vapor mole fraction (f_v) of gas-condensate sample used to compare developed CVD test in VBA and commercial PVT simulator PVTi. The result shows good agreement between our algorithm and PVTi.

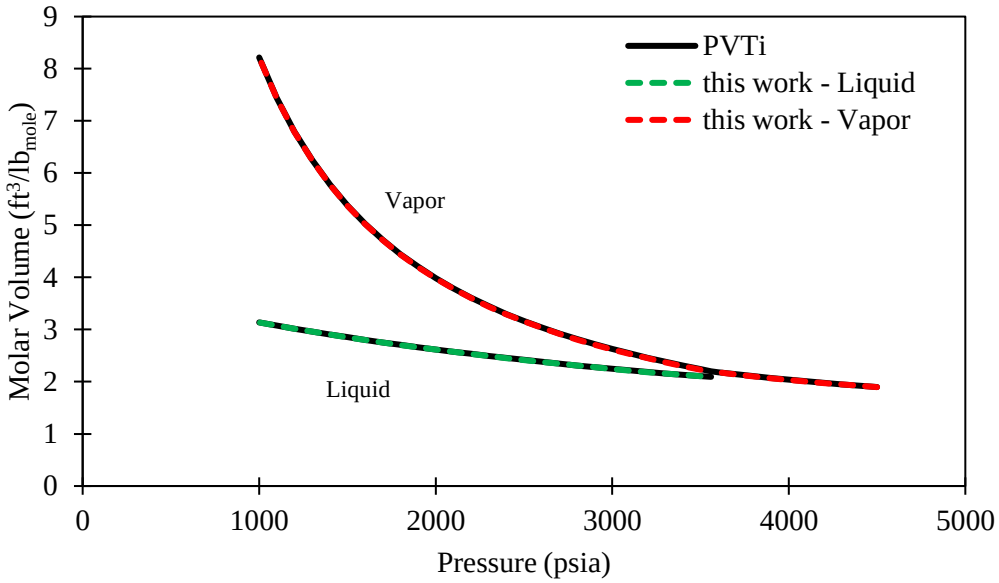

Figure 20 – Molar volume of liquid (green) and gas (red) phases in the CVD experiment. The comparison shows an excellent match between model and commercial results.

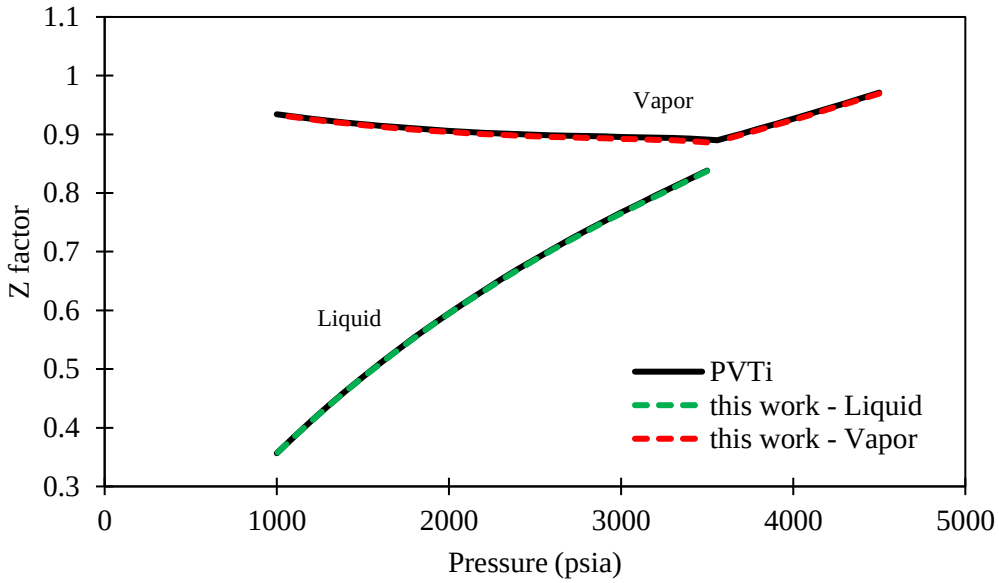

Figure 21 – *Z*-factor comparison between the commercial software PVTi and the CVD developed for this study shows excellent agreement in both liquid (green) and vapor (red) phases.

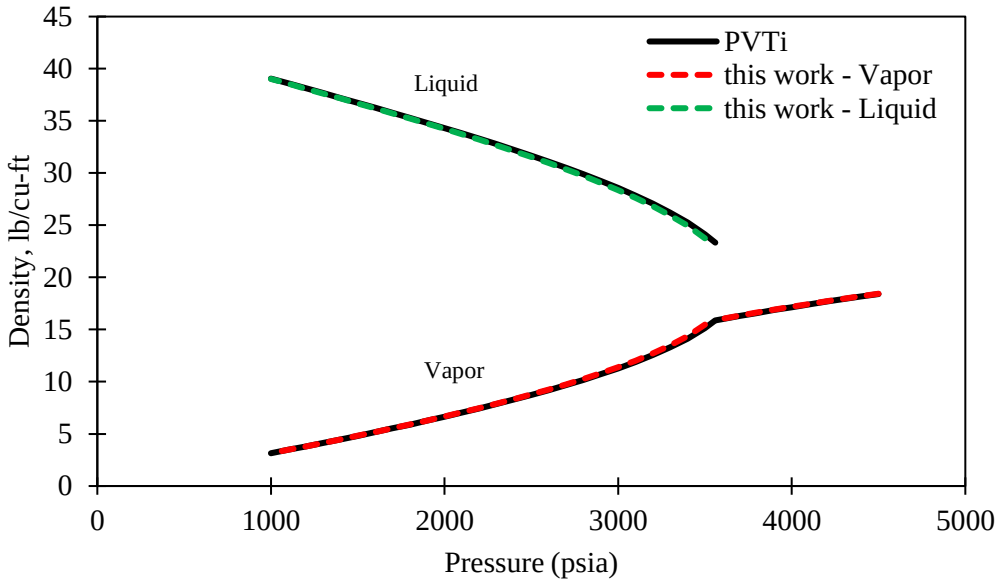

Figure 22 – Density of both phases throughout the CVD process. The result shows great agreement between the developed and the commercial results.

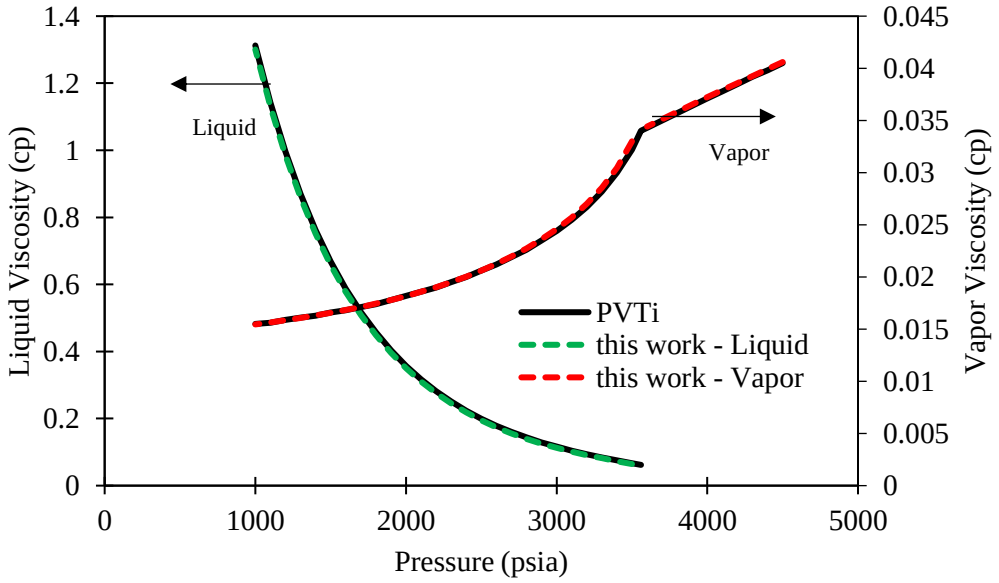

Figure 23 – Viscosity comparisons shows great agreement between the developed and commercial CVD.

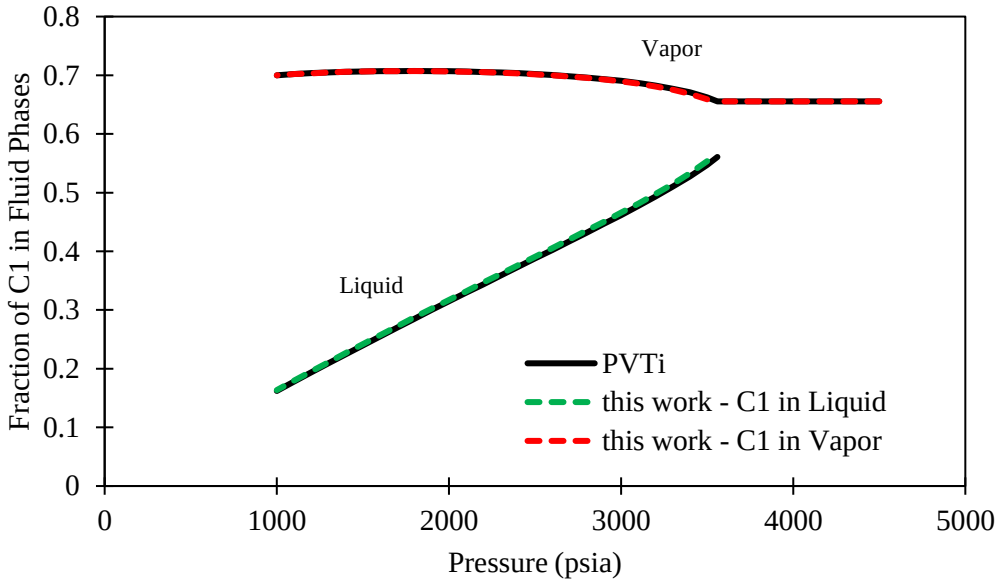

Figure 24 – This graph shows the methane fraction in the liquid (green) and vapor (red) phases of the fluid. The comparison shows great agreement with the commercial software.

3.3 Modified Constant Volume Depletion test

The ultimate goal of this research project is to couple the CVD with flow equations to simulate production from a gas-condensate reservoir. To enable this capability, I made several modifications to the CVD algorithm to better represent gas-condensate reservoirs: starting the simulation at pressures above the dewpoint pressure, assuming perfect-mixture production, considering the effects of relative permeabilities on production, and considering adsorption. Furthermore, the simulation is able to take into account user-defined relative permeability curves and parameters for the extended Langmuir adsorption model. These modifications are optional for use in the model.

3.3.1 Simulating at Given Initial Pressure

The traditional CVD test begins with the fluid charged at dewpoint pressure. However, for the case of gas-condensate reservoirs, the initial reservoir pressure is rarely the same as the fluid's saturation pressure at the reservoir temperature. Thus, we need to account for

any given pressure above or below the saturation point of the fluid as a starting point for pressure.

In the case of reservoirs with pressure above the dewpoint, as pressure depletes, the fluid begins as a single-phase gas. In this region of single-phase gas, the production stream coming from the reservoir has the same composition as the reservoir fluid. The fluid remains in the gas phase until pressure reduces below the dewpoint, when liquid will form. To account for this, the CVD algorithm is allowed to begin at any pressure above or below the dewpoint.

3.3.2 Perfect-Mixture Production Assumption

The perfect-mixture production assumption is a modification to the CVD test's method of fluid production. This assumption attempts to address the possibility of production from both the liquid and gas phases of the fluid.

The assumption of a perfect mixture treats the liquid and gas phases as equally producible. The production is based on the molar fractions of the fluid in the CVD cell. With this modification, instead of producing only from the gas phase, the production is from both gas and liquid phases, as illustrated in Figure 25.

The modification for this assumption is in the calculation of the moles produced. The moles produced are calculated using the molar volume of the mixture (V_{m_m}), described in Eq. 3.13. Here, the produced volume (V_{prod}) is obtain from Eq. 3.3. The mixture molar volume is calculated using Eq. 3.14. Here, the superscript j denoting the pressure step is omitted for clarity.

$$n_{\text{prod}} = \frac{V_{\text{prod}}}{V_{m_m}} \tag{3.13}$$

$$V_{m_m} = f_g V_{m_g} + f_o V_{m_o} \tag{3.14}$$

where

V_{m_m} = mixture molar volume

V_{m_o} = liquid/oil molar volume

V_{m_g} = vapor/gas molar volume

V_{prod} = volume to be produced (Eq. 3.3)

n_{prod} = moles to be produced

$f_{g,o}$ = molar fraction of gas (g) or oil (o) phase

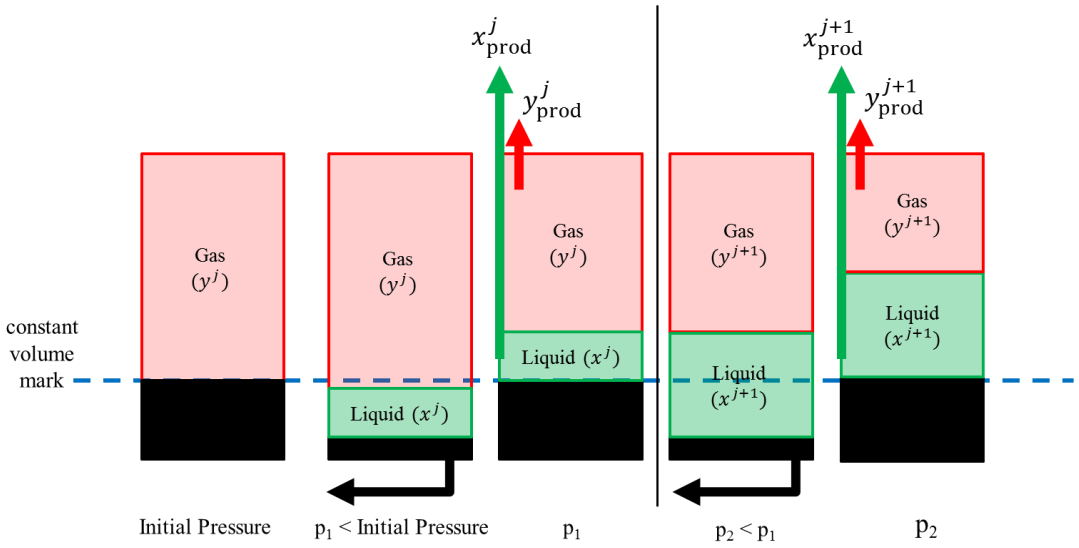

Figure 25 – Illustration of production scheme considering both liquid and gas production from CVD cell. Fluid produced based on perfect-mixture assumption or relative permeability.

The calculated produced moles are then proportioned to moles of gas (n_{prod_g}) and liquid (n_{prod_o}) produced. This is done by multiplying the produced moles, from Eq. 3.13, with molar fraction of the gas (f_g) and liquid (f_o), as described in Eq. 3.15.

$$n_{\text{prod}_g} = f_g \, n_{\text{prod}} \tag{3.15}$$

$$n_{\text{prod}_o} = f_o \, n_{\text{prod}}$$

We proceed to divide the moles produced from each phase to each component in the phases. Multiplying the produced moles of gas and liquid with the composition of the components in gas (y_i) and liquid (x_i), we obtain the moles to be produced from each component. These calculations are described in Eq. 3.16.

$$\begin{aligned} n_{\text{prod}_g i} &= y_i \, n_{\text{prod}_g} \\ n_{\text{prod}_o i} &= x_i \, n_{\text{prod}_o} \end{aligned} \tag{3.16}$$

Once the number of moles to be produced from each component is determined, we subtract this value from the total number of moles in the phases. The calculation for the remaining gas moles is described in Eq. 3.17. Similarly, an equation can be written for the liquid phase, described in Eq. 3.18. In the following equation, the superscript j is reintroduced to clarify the pressure step.

$$n_{g,i}^{j+1} = n_{g,i}^{j} - n_{\text{prod}_g i}^{j} \tag{3.17}$$

$$n_{o,i}^{j+1} = n_{o,i}^{j} - n_{\text{prod}_o i}^{j} \tag{3.18}$$

Then we recombine the remaining moles from gas and liquid through summation (Eq. 3.19). The moles remaining are used in the next VLE calculation at a lower pressure step.

$$n_i^{j+1} = n_{g,i}^{j+1} + n_{o,i}^{j+1} \tag{3.19}$$

where

n_i^{j+1} = total moles (remaining) of component i

3.3.3 Production According to Relative Permeability

In gas-condensate reservoirs, there is condensate (liquid) dropout in the reservoir as pressure falls below dewpoint pressure. If the saturation of liquid is high enough, liquid will flow to the wellbore and be produced along with the gas. The liquid's ability to flow can be controlled based on a relative permeability curve defined in the simulation.

In the relative-permeability production method, the assumption is that the production ratio between liquid and gas moles is dictated by the shape of the relative permeability curve that is specified by the user. This contrasts with the traditional CVD test, where production only comes from the gas phase of the fluid, or the perfect mixture assumption, where the portioning of the production is done through the phase molar fraction.

This modification is done on the fluid production step of the CVD simulation process. Once the volume to be produced is calculated from Eq. 3.3, the liquid saturation (S_l) is calculated to determine the relative permeabilities. The saturation of liquid is obtained by dividing the volume of liquid with the total volume of the fluid at the current pressure step. This saturation is calculated before fluid production, as in Eq. 3.20.

$$S_l = \frac{V_l^j}{V^j} \tag{3.20}$$

Based on the saturation, the relative permeability to gas (k_{rg}) and liquid (k_{ro}) is determined using a table lookup. This relative permeability information is used to determine gas (V_{prod_g}) and liquid (V_{prod_o}) volumes to be produced. The calculation for volume of gas and volume of liquid to be produced is done by multiplying the total volume to be produced with the normalized relative permeability of gas and liquid, respectively, shown in Eq. 3.21.

$$V^j_{\text{prod}_g} = V^j_{\text{prod}}\, k^j_{\text{rg}^*}$$
$$V^j_{\text{prod}_o} = V^j_{\text{prod}}\, k^j_{\text{ro}^*} \tag{3.21}$$

The normalized relative permeability (Eq. 3.22) is used to determine the liquid and gas volume produced because the summation of gas and liquid relative permeabilities seldom equals unity.

$$k_{\text{rg}^*} = \frac{k_{\text{rg}}}{k_{\text{rg}} + k_{\text{ro}}}$$
$$k_{\text{ro}^*} = \frac{k_{\text{ro}}}{k_{\text{rg}} + k_{\text{ro}}} \tag{3.22}$$

The next step is to translate the volume produced in terms of moles produced by dividing with gas (V_{m_v}) and liquid (V_{m_l}) molar volume, as in Eq. 3.23.

$$n^j_{\text{prod}_g} = \frac{V^j_{\text{prod}_g}}{V^j_{m_g}}$$
$$n^j_{\text{prod}_o} = \frac{V^j_{\text{prod}_o}}{V^j_{m_o}} \tag{3.23}$$

Once the produced moles are determined, the process is similar to the perfect-mixture assumption. We proceed to calculate the moles produced from each component. This process is described in Eq. 3.16, as previously presented.

$$n^j_{\text{prod}_g i} = y^j_i\, n^j_{\text{prod}_g}$$
$$n^j_{\text{prod}_o i} = x^j_i\, n^j_{\text{prod}_o} \tag{3.16}$$

The next step is to subtract the moles produced from the current total moles. This calculation is done using Eq. 3.17 and Eq. 3.18, presented previously in the perfect-mixture section. Finally, the remaining moles in both gas and liquid phases are recombined by adding the moles of the component in the gas and liquid phase as a new input into the VLE calculation for the next lower pressure step (Eq. 3.19). Figure 26 shows the flowchart of the modified CVD considering relative permeability production.

$$n_{g,i}^{j+1} = n_{g,i}^{j} - n_{\mathrm{prod}_g i}^{j} \tag{3.17}$$

$$n_{o,i}^{j+1} = n_{o,i}^{j} - n_{\mathrm{prod}_o i}^{j} \tag{3.18}$$

$$n_{i}^{j+1} = n_{g,i}^{j+1} + n_{o,i}^{j+1} \tag{3.19}$$

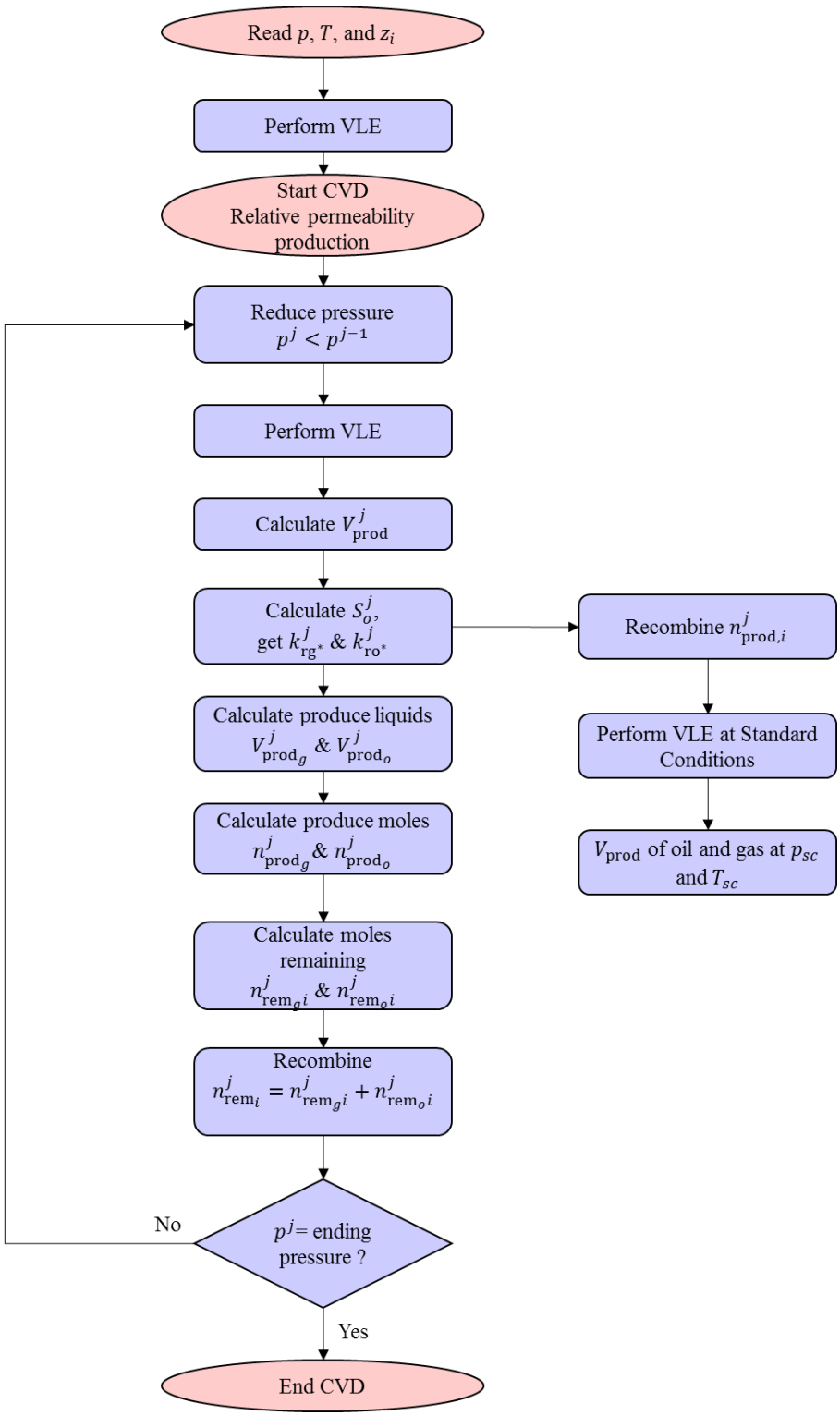

Figure 26 – Flowchart of modified CVD test with relative permeability production considerations.

3.3.4 Multicomponent Adsorption Coupling

The consideration of multicomponent adsorption is important in the calculation of gas-in-place (Ambrose et al. 2011; Hartman et al. 2011). As described in 0, the presence of adsorbed molecules increases the gas storage capacity of the reservoir by retaining adsorbed gas in a denser state. However, due to the small pore size of the shale resources, the portion of void space occupied by the adsorbed molecules cannot be ignored.

Ambrose et al. (2011) presented a volumetric calculation coupled with a multicomponent adsorption model that introduced an adsorbed-porosity fraction term to account for pore space taken by the adsorbed molecules (Eq. 2.60). In this work, I considered multicomponent adsorption with an extended Langmuir (EL) adsorption model. As noted previously, the EL adsorption model is commonly used in the petroleum industry, though it is not thermodynamically consistent. The thermodynamic inconsistency comes from the assumption of a finite number of adsorbed molecules as pressure nears infinity, which cannot be proven.

The EL adsorption model presented in Eq. 2.57 is calculated in terms of volume per rock mass (scf/ton). It can also be calculated in terms of moles per rock mass through the use of the real-gas law at standard temperature and pressure, shown in Eq. 3.24. By calculating adsorbed moles, we can directly add desorbed moles into the CVD cell.

$$n_a^{EL} = \frac{p_{sc} G_a^{EL}}{zRT_{sc}} \tag{3.24}$$

where:

G_a^{EL} = adsorbed gas volume (scf/ton)

n_a^{EL} = adsorbed gas moles (lb_{mole}/ton)

p_{sc} = pressure at standard conditions (14.7 psia)

z = compressibility factor = 1 at standard conditions

R = universal gas constant (10.73159 $\frac{ft^3 psia}{R\ lbmol}$)

T_{sc} = temperature at standard conditions (60°F or 520°R)

Furthermore, the contribution of desorbed gas is incorporated into the framework of the CVD program by adding the desorbed moles for each component into the remaining fluid at the fluid recombination stage (Figure 27). The moles of desorbed gas can be calculated through the EL model.

To obtain the moles desorbed at a pressure stage, we subtract the adsorbed moles in the current pressure step from the adsorbed moles from the previous one (Eq. 3.25). Since the EL adsorption model is multicompositional, this can easily be done for every existing component. The desorbed moles can be recombined with the remaining moles (Eq. 3.26). The recombined fluid is used in the next pressure decrement step.

$$n_{\mathrm{des}_i}^{\ j} = \left(n_{a_i}^{\ j-1} - n_{a_i}^{j}\right) \cdot m_{\mathrm{rock}} \tag{3.25}$$

$$n_{\mathrm{rem}_i}^{j} = n_{\mathrm{rem}_v i}^{j} + n_{\mathrm{rem}_l i}^{j} + n_{\mathrm{des}_i}^{\ j} \tag{3.26}$$

where:

$n_{\mathrm{des}_i}^{j}$ = amount of desorbed moles of component i at pressure j

$n_{a_i}^{\ j}$ = amount of adsorbed moles of component i at pressure step j

$n_{a_i}^{j+1}$ = amount of adsorbed moles of component i at pressure step $j+1$

$n_{\mathrm{rem}_i}^{j}$ = amount of moles remaining in CVD tank of component i

$n_{\mathrm{rem}_v i}^{j}$ = amount of moles remaining in CVD tank of component i in the vapor phase

$n_{\mathrm{rem}_l i}^{j}$ = amount of moles remaining in CVD tank of component i in the liquid phase

The adsorption can be incorporation into the CVD with any production assumption presented in the previous section (gas only, perfect-mixture, or relative permeability).

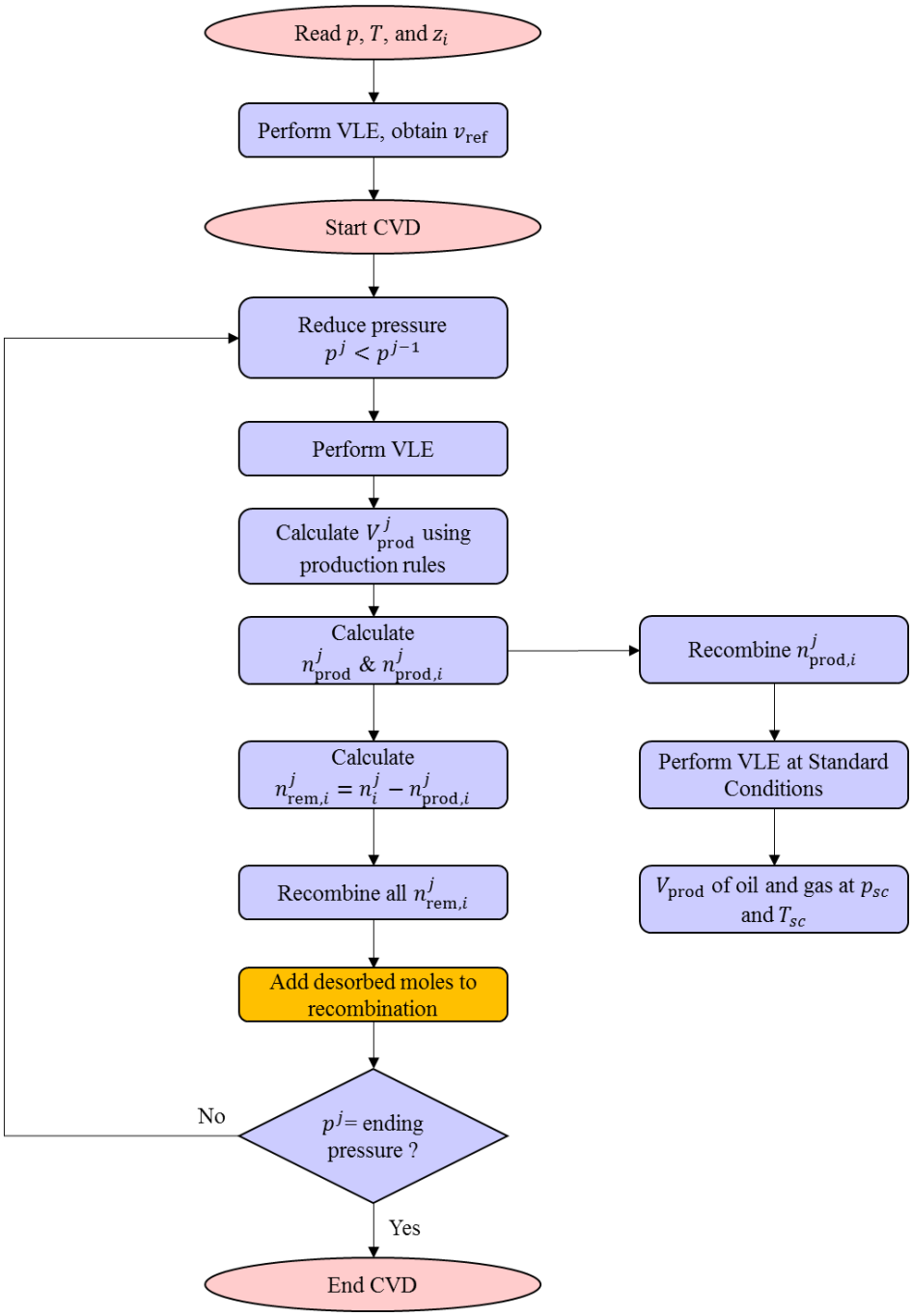

Figure 27 – Flowchart of CVD modified with contribution of desorbed fluid (yellow box). The desorbed fluid is added at the recombination step.

3.4 Comparison of Modified CVD Assumptions

I compared the results of the three different CVD production methods—gas only, perfect-mixture, and relative permeability—on the fluid production. The gas-only production follows the conventional CVD experiment, where only the gas (vapor) phase of the fluid is withdrawn to maintain constant volume. The perfect-mixture production withdraws fluid based on the molar fraction of the respective phase. Relative-permeability production produces fluid based on the liquid saturation of the cell. Thus, to apply this method, we need to specify a relative permeability curve as in Figure 28. The comparison runs from an initial pressure of 4,500 psia to a final pressure of 1,000 psia. The total initial mole volume is 100 mg-mole with a calculated reference volume of 11.98 cc at initial reservoir conditions. The produced volume reported in this section is calculated from the produced moles at every pressure decrement step, flashed to standard conditions (14.7 psia and 60^{o}F).

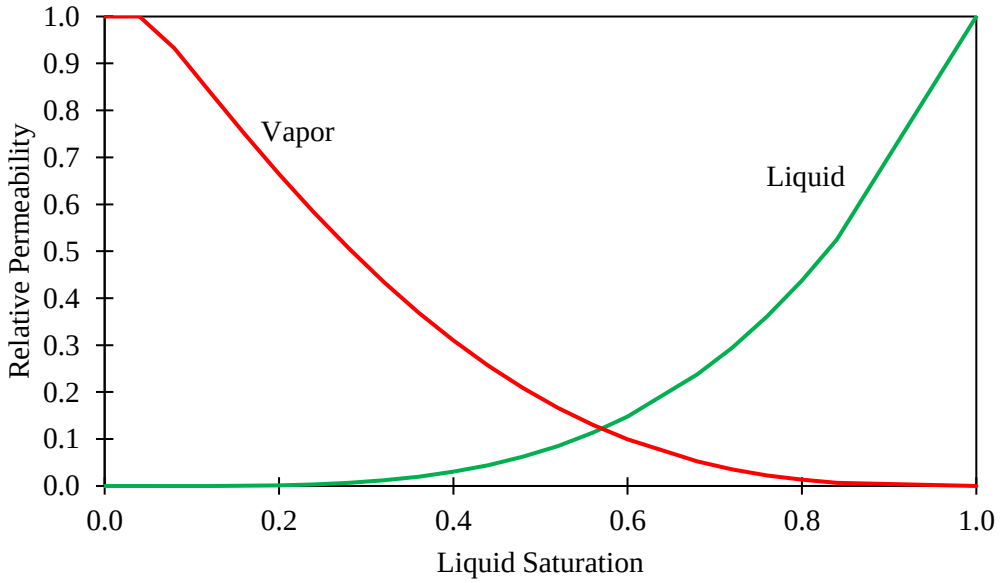

Figure 28 – Relative permeability curve for gas and oil fluid mixture. This relative permeability curve synthetically created using Eq. 2.67 and Eq. 2.68 ($S_{oc} = 0.05$ and $\lambda = 4$) and was used to compare the different production schemes of the CVD.

The comparison of gas production is presented in Figure 29 for an Eagle Ford fluid mixture with composition detailed in Table 10. The graph is presented as cumulative production of vapor (standard conditions) against pressure in reverse order. We can see that the vapor production of the three production schemes is very similar. The reason for this is that the vapor phase dominates the volume of the fluid mixture at every pressure stage. Thus, even in the perfect mixture and the relative-permeability mixture, the amount of fluid in the liquid phase is too small to significantly impact the vapor production.

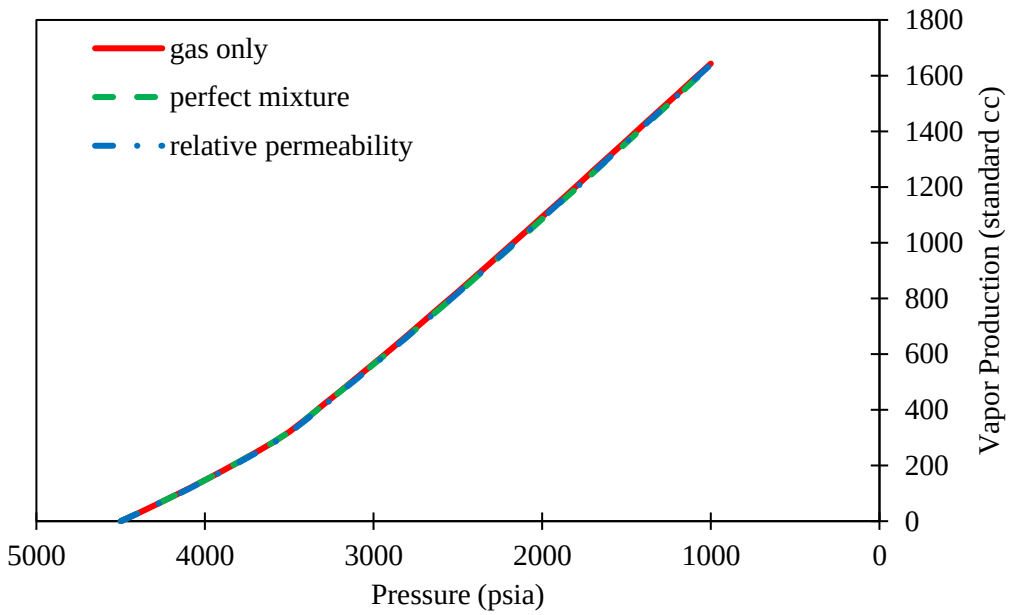

Figure 29 – Vapor production of example fluid composition considering the three production methods. The gas produced is flashed to standard pressure and temperature (14.7 psia and 60ºF).

The results of liquid production at standard conditions versus pressure appear in Figure 30. The first item to note in the produced-liquid graph is the scale of the volume, which is significantly different from the produced-vapor graph, which shows the domination of gas volume in the mixture. Also, since the produced liquid is shown at standard conditions,

the curves include liquid dropout from the vapor portion of the produced fluid. For this reason, the gas-only production method also produces liquid as pressure depletes.

From Figure 30, we observe that the perfect-mixture production method estimates a significantly higher liquid production than either the relative-permeability or gas-only production scheme. The perfect-mixture production method results in a higher produced liquid due to the assumption that the fluid system is not segregated, thus leading to a higher portion of liquid being produced. We compare this the production from relative permeability, which allows the production of liquid from CVD tank. Though the relative permeability method also allows for the production of liquid and gas, the production is governed by the saturation-dependent relative permeability curve. Since the saturation of the liquid does not build up significantly, the relative permeability values experience very small changes, thus leading to insignificant liquid production. We see very slight difference between the relative permeability-production curve and the gas-only production curve. The results of the cumulative gas and oil production from the three production rules are tabulated in Table 12.

Table 12 – Comparison of CVD cumulative fluid production from the proposed production rules.

CVD Production Rules	Cumulative Gas Produced (standard cc)	Cumulative Oil Produced (standard cc)
Conventional CVD	1643.17	0.60
Perfect-Mixture	1636.40	1.25
Relative Permeability	1639.56	0.62

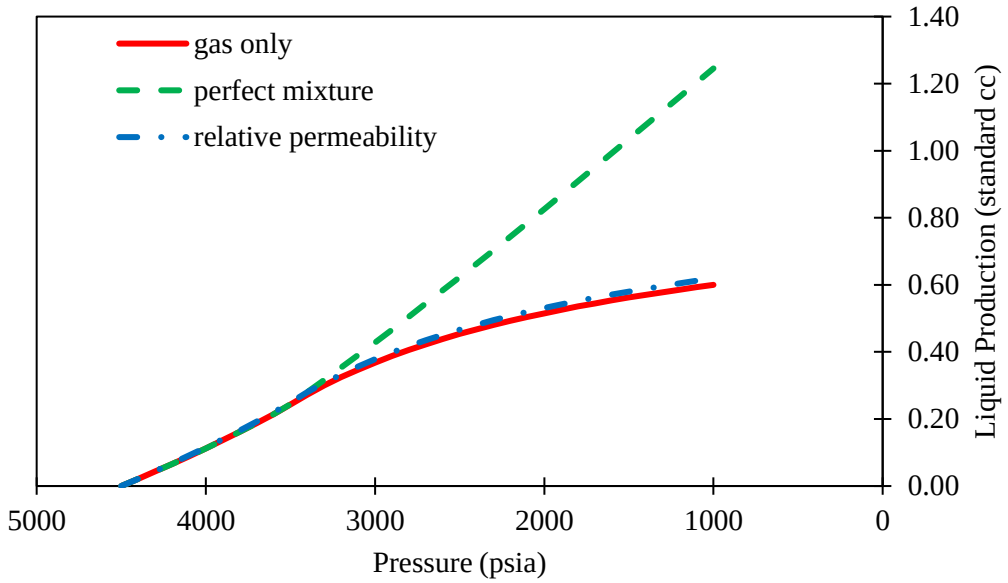

Figure 30 – Liquid production of example fluid composition comparing different production schemes. The liquid produced is flashed to standard pressure and temperature (14.7 psia and 60ºF).

3.4.1 Adsorption Coupling Comparison

In this section, we compare the impact of adsorption on the production from the CVD cell. We use the fluid model presented in Table 13 with reservoir temperature of 180ºF. The phase envelope of this fluid is shown in Figure 31, with the CVD pressure depletion path shown with the vertical red line that crosses the dewpoint. The reservoir model properties used in this comparison is presented in Table 14. We present the results in the form of cumulative gas production with pressure depletion in Figure 32.

Table 13 – Fluid model for adsorption comparison.

Component	M_w	P_c (psia)	T_c (°F)	ω	z_i	s	Z_{crit}	P
C_1	16.043	667.4	-116.9	0.008	65	-0.14427	0.28029	77
C_2	30	708.5	89.7	0.098	15	-0.10327	0.27448	108
C_3	44.1	615.9	205.6	0.152	8	-0.0775	0.28216	150.3
nC_4	58.1	551.3	305.4	0.193	6	-0.06198	0.27013	189.9
iC_4	58.1	529.2	274.6	0.176	5	-0.05422	0.26914	181.5
CO_2	44.01	1070.2	87.6	0.225	1	-0.04273	0.28419	78

Table 14 – Reservoir properties for adsorption comparison case.

r_e	1000	ft
h	30	ft
ϕ	0.10	fraction
S_w	0	fraction
ρ_{bulk}	156	lb/ft^3
T_{res}	180	^{o}F

The reservoir model is required because the calculation of adsorbed gas is based on volume or mass per ton of rock. The calculation to consider adsorption follows the explanation in 0. First, we create the extended Langmuir isotherm using Eq. 2.57. As noted previously, according to studies by Ambrose et al. (2012), adsorbed molecules have a finite size that occupies the pore space, thus taking away void space available for free gas. However, as we have explained in Chapter II, this is only valid for shale reservoirs with very small pores (10 nm). The impact of adsorbed molecules on the total void space gets less significant with larger size pores. Thus, in this work, I neglected the impact of pore space taken up by adsorbed molecules.

In the CVD program, only the free-gas components can be produced. The adsorbed components are desorbed according to the EL isotherm. The desorbed components are added to the free-gas mix after each associated pressure drop (as explained in Chapter 3.3.4).

Table 15 – Calculated gas in-place from adsorption, example case.

Free gas	1,272	MMSCF
Adsorbed gas	486	MMSCF
Total gas	1,758	MMSCF

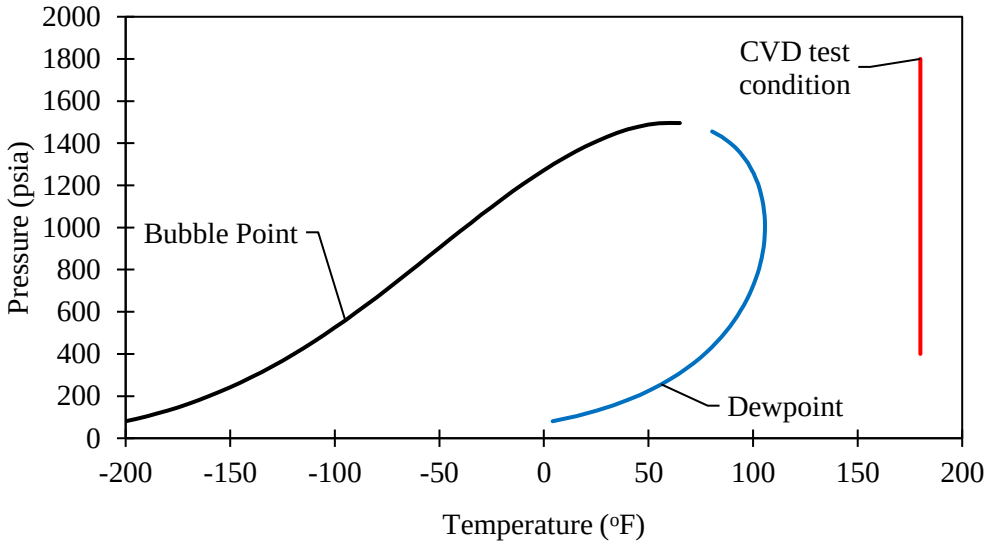

Figure 31 – Phase envelope of gas-condensate fluid presented in Table 13, created with the in-house PVT simulator developed by Valbuena Olivares (2011).

We studied the impact of adsorption for the gas-only production scheme from a CVD pressure of 1,800 psia to 400 psia. The results (Figure 32) show that the cumulative production considering adsorption is 20% higher than without adsorption. The desorption process depends on the extended Langmuir isotherm (Figure 33), which requires a significant decrease in pressure before a significant amount of gas is desorbed and available to be produced.

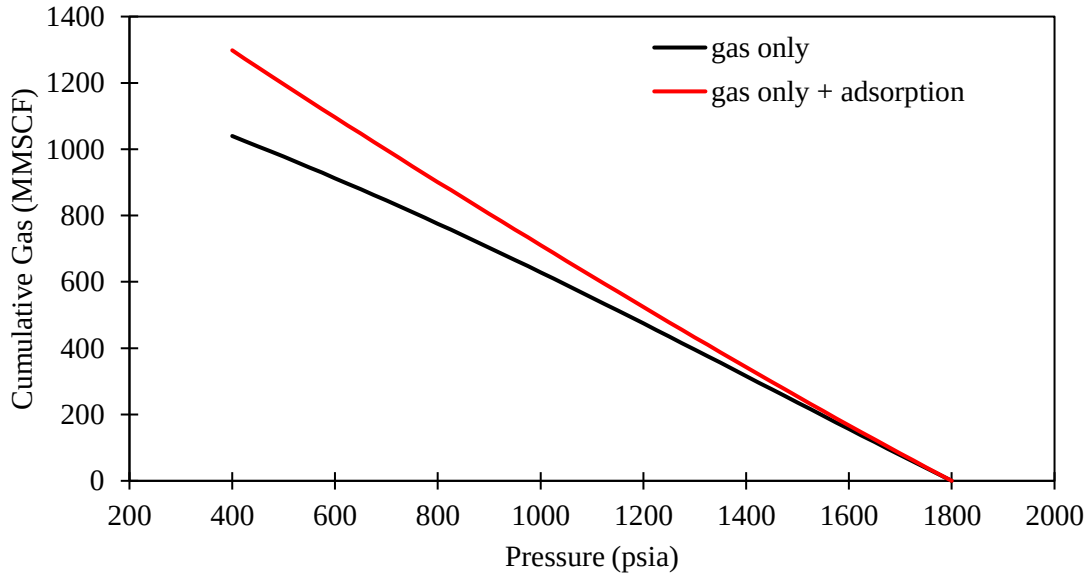

Figure 32 – Comparison of CVD results with and without the consideration of adsorption using the new methodology of adsorbed molecules occupying finite spaces in the pore.

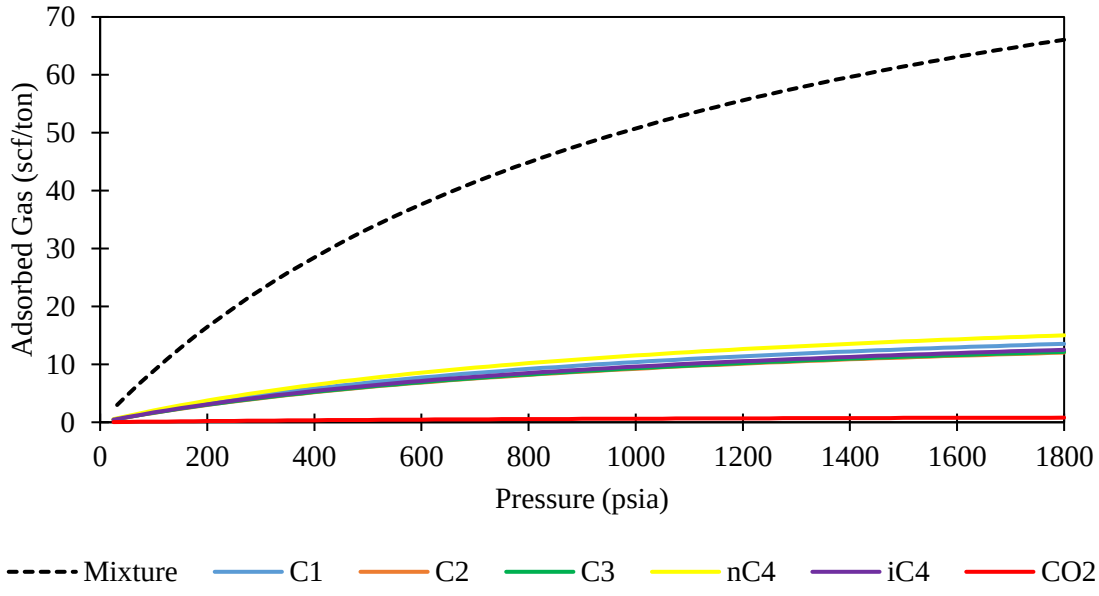

Figure 33 – Extended Langmuir isotherms created of gas mixture with composition in Table 13 and reservoir properties in Table 14.

In summary, the CVD test developed in this work produced results in good agreement with the commercial software PVTi. We assumed and programmed three different production methods (gas only, perfect mixture, and relative permeability) to mimic the production from gas-condensate reservoirs. Comparing the results from the different production assumptions, I found that the perfect mixture assumption produced significantly more oil than the other methods. Liquid saturation remaining below the critical saturation causes the results between the gas only and relative permeability productions to be very similar. Coupling the CVD test with adsorption yielded higher production volumes than the initial CVD model. However, as discussed in Chapter 2, the adsorbed molecules contribution is dependent on pore size. Coupling the CVD with the flow equation is detailed in the next chapter and provides a relation between production and time.

CHAPTER IV

MECHANISTIC PRODUCTION MODEL COUPLING

This chapter describes the coupling between the new CVD code and the radial flow equation to establish a time-production relationship. In this work, I assumed the pseudosteady-state flow equation to calculate gas rate. I considered three operating conditions in forecasting production from a gas condensate reservoir: constant production rate, constant bottomhole pressure, and constant drawdown pressure. Additionally, I incorporated a hydraulic fracturing completion into the flow equation, modeled as an equivalent skin factor. The induced fracture model is based on a finite-conductivity fracture.

The three well operating conditions are based on common practices implemented by operators in the field. Chokes are used in the industry to manage fluid production rates and control drawdown pressure. By choking a well, operators are able to maintain stable downstream pressure and provide the necessary reservoir backpressure to avoid formation damage from excessive drawdown (Guo et al. 2007). Chokes are also used to slow the rapid decline rates from wells producing in shale/low-permeability reservoirs, thus increasing the estimated ultimate recovery (EUR) of the well (Norris 2012; Okouma Mangha et al. 2011). Artificial lift systems (ALS) are also installed in the well to increase production. These systems are placed to maintain a constant bottomhole pressure on the well, thus allowing for larger fluid production. In tight reservoirs, operators often have to install artificial lift earlier due to the rapid decline (Lane and Chokshi 2014).

4.1 Mechanistic Model Parameters

The mechanistic-based production model requires specific user inputs to forecast production. This section details the required information to run the model which can be divided into three parts: reservoir properties, completion and operating conditions, and simulation parameters. The required information is used to calculate flow rate using the pseudosteady-state equation presented as Eq. 2.46.

$$q_{gsc} = \frac{kh\left(m(\bar{p}) - m(p_{wf})\right)}{1424T\left(\ln\left(\frac{r_e}{r_w}\right) + s\right)} \quad \text{(Eq. 2.46)}$$

4.1.1 Reservoir Properties

Information regarding the reservoir is necessary for the forecasting model. These properties are listed in Table 16. Initial reservoir pressure and reservoir temperature are required as inputs for the CVD calculation. The reservoir radius, height, and porosity are used to calculate the void space available for the fluid. This model does not consider the presence of water in the reservoir. Skin factor can be added to account for reduction of flow due to formation damage. To consider adsorption, the reservoir bulk density and the total organic content (TOC) are required to properly incorporate the extended Langmuir model in the developed simulation. The user may also input values for Langmuir pressure and volume parameter of pure components.

Table 16 – Reservoir properties necessary to forecast production.

Reservoir Information		
Initial Reservoir Pressure	*user input*	psia
Reservoir Temperature	*user input*	^{o}F
Reservoir Radius	*user input*	ft
Reservoir Height	*user input*	ft
Permeability	*user input*	md
Porosity	*user input*	fraction
Initial Water Saturation	*user input*	fraction
Skin	*user input*	dimless.
Rock Properties		
Bulk Density	*user input*	g/cc
TOC	*user input*	%

4.1.2 Completion and Operating Conditions

The next items that are required are the well completion and operating constraints. Wellbore radius (r_w) is requested in feet for the inflow equation. The operating condition of the well is governed by user inputs in Table 17. The user may conduct the production forecasting under a constant rate, constant bottomhole flowing pressure, or constant drawdown pressure condition.

For the constant-rate condition, a production rate (in MSCF/D) is requested to constrain the well to the specified gas rate. Additionally, a minimum bottomhole pressure value is required to limit the depletion of the well. For this case, if a specified rate cannot be achieved, the simulation implements a constant minimum bottomhole-pressure production constraint. The economic limit is also a constraint on the well operations, requested in MSCF/D. The simulation terminates when the economic limit is reached.

A constant-bottomhole-pressure constraint can be established by entering a value for the "Constant BHP" value. The simulation conducts the calculation for gas rate at the constant BHP specified until other constraints are reached, such as economic limit or time. A constant drawdown operating condition constraint is also available by entering a value of

drawdown pressure in psia. Similar to the constant-bottomhole-pressure constraint, the simulation calculates for gas rate.

To consider a hydraulic fracture completion of finite conductivity, the model requests inputs for fracture half-length (x_f) in feet, fracture permeability (k_f) in milidarcies, and fracture width (w_f) in feet. The calculations for effective wellbore radius and equivalent skin factor for fractures are described in 0.

Table 17 – Completion details and operating condition inputs.

Wellbore Properties		
Wellbore Radius	*user input*	ft
Operating Conditions		
Production Rate	*user input*	MSCF/D
Minimum BHP	*user input*	psia
Economic Limit	*user input*	MSCF/D
Constant BHP	*user input*	psia
Constant Drawdown	*user input*	psia
Fracture Geometry		*(on/off)*
- as an equivalent skin effect, s_f		
r_w effective (r_w')	*calculated*	ft
Fracture Characteristics		
x_f	*user input*	ft
k_f	*user input*	md
W	*user input*	ft
C_{fD}	*calculated*	
s_f	*calculated*	

4.1.3 Simulation Parameters

The third group of values to be filled in is the simulation preferences. Here, the user is asked for additional run options relating to the CVD mechanism. Adsorption, as explained in previous chapters, can be coupled with the CVD. Relative-permeability curves can be implemented. The relative permeability option also considers condensate banking modeling to be calculated and used in the flow equation calculation (0). The simulation

can also be conducted using the pseudopressure $[m(p)]$ or the average pressure $(\bar{\mu}, \bar{Z})$ approach.

The user is free to input the pressure decrements to be used in the CVD mechanism and the length of the simulation time in years. The simulation will be terminated if the forecasting time is over the specified value or reached the specified constraints defined previously.

Table 18 – Additional simulation parameters

Run Options		
Adsorption	**on/off:**	*(on/off)*
Relative Permeability	**on/off:**	*(on/off)*
Pressure equation:	**average/pseudo**	*(average/pseudo)*
Perfect-mixture	**on/off:**	*(on/off)*
Model Properties		
Pressure decrements (psia)		*user input*
Simulation time (years)		*user input*

4.2 Coupling Flow Equation and CVD

This model takes three main steps to forecast the production of a gas-condensate reservoir: initialization of the reservoir model, calculation of rate according to specified constraints, and calculation of material balance time. Through these steps, we can couple the CVD results with the flow equation to obtain a relationship of production with time.

4.2.1 Reservoir Model Initialization

The first step is the initialization of the reservoir model. The void space for the reservoir is obtained by using a cylindrical volumetric calculation (Eq. 4.1).

$$V_R = \pi r_e^2 h\, \phi \tag{4.1}$$

where

V_R = volume of reservoir pores available for fluid (ft^3)

r_e = reservoir radius (ft)

h = reservoir height (ft)

ϕ = porosity (fraction)

Compute the number of moles, at initial reservoir conditions, using the real gas law relationship in Eq. 4.2.

$$n_R = \frac{p_R V_R}{z_R R T_R} \tag{4.2}$$

where

n_R = moles in the reservoir (lb_{mole})

p_R = reservoir pressure (psia)

T_R = reservoir temperature (^oR)

V_R = reservoir volume (ft^3)

z_R = z-factor of the fluid at p_R and T_R (dimensionless)

R = universal gas constant ($10.73 \frac{\text{psia ft}^3}{\text{R lb}-\text{mole}}$)

The calculated total initial moles (n_R) are then distributed according to the initial fluid composition to initialize the reservoir. After the initialization process, the CVD program is executed. As explained in Chapter III, the produced fluid volumes at every pressure step are calculated and recorded at standard conditions (14.7 psia and 60^oF). The next step is to calculate rate and create a relation between production and time. This coupling is described in the next subsection.

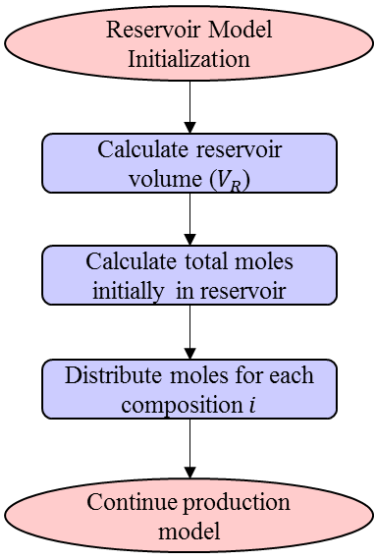

Figure 34 – Flowchart of initialization of reservoir model to prepare for the CVD calculation.

4.2.2 Production Methods

The second step is calculating the gas flow rate at each pressure step. To represent the different production methods implemented in the field, this study considered the following production constraints:

a. Constant bottomhole flowing pressure
b. Constant-gas-rate production
c. Constant drawdown pressure

The main goal of this step is to calculate a gas rate using the pseudosteady-state flow equation. Once gas rate is obtained, time of production can be computed. This is done by dividing total gas produced, from the CVD, by the gas rate calculated at the pressure step. The time that is obtained from this method is often referred to as material balance time (MBT) described in the final step.

The following subsections detail the implementation of the operating constraints. As mentioned previously, this work assumes pseudosteady-state flow. The simplified formula

for pseudosteady-state flow is presented in Eq. 4.3, with pseudopressure $[m(p)]$ from Eq. 2.47. The constant C represents the constant values in the pseudosteady-state flow equation (Eq. 4.4).

$$q_g = \frac{\left[m(\bar{p}) - m(p_{wf})\right]}{C} \tag{4.3}$$

$$C = \frac{1424 T_R \left[\ln\left(\frac{r_e}{r_w}\right) + s\right]}{kh} \tag{4.4}$$

$$m(p) = 2\int_{p_o}^{p} \frac{p}{\mu Z} dp \tag{2.47}$$

Constant Bottomhole Pressure

We use a constant value for bottomhole flowing pressure (p_{wf}) and the pseudosteady-state flow equation to calculate for gas rate. When bottomhole pressure is constant, the calculation for gas rate (q_g) is a straightforward calculation using Eq. 4.3. The calculated gas flow rate is at standard conditions (14.7 psia and 60°F) in units of MSCF/D. The average reservoir pressure ($\bar{p}$) is assumed to be the pressure of the CVD tank at the current pressure step. The bottomhole pressure (p_{wf}) is from user input and kept constant.

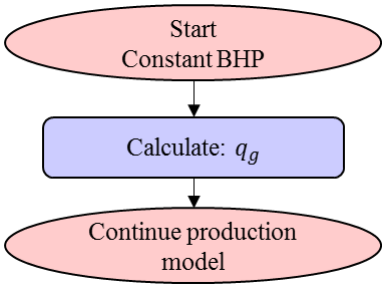

Figure 35 – Constant bottomhole pressure flowchart. The calculation is straight forward to obtain rate, since reservoir pressure and bottomhole pressure are known.

Constant Gas Rate

The objective of the constant-gas-rate constraint is to obtain a reasonable bottomhole pressure that can accommodate the gas rate requested by the user. This calculation is done using the radial pseudosteady-state flow equation (Eq. 4.3) for the calculation. With the reservoir pressure ($\bar{p}$) and gas rate (q_g) as knowns for the flow equation, the constant gas rate program solves for bottomhole pressure (p_{wf}). This rearrangement of the flow equation is presented in Eq. 4.5 with the average-pressure approach. The equation uses viscosity ($\bar{\mu}$) and gas compressibility factor ($\bar{Z}$) evaluated at average pressure as defined in Eq. 4.6. The calculation is conducted for every pressure drop of the CVD model. This assumption is valid for low drawdown pressures, where gas properties variations are small.

$$p_{wf} = \bar{p} - \left(\frac{q_g C \overline{\mu Z}}{2p_{\text{avg}}}\right) \tag{4.5}$$

$$p_{\text{avg}} = \frac{\bar{p} + p_{wf}}{2} \tag{4.6}$$

The calculation in the constant-gas-rate operating condition requires an initial guess for bottomhole pressure and an iteration process to achieve the correct value for bottomhole pressure. This is because the gas properties, viscosity (μ) and compressibility factor (Z), depend on the bottomhole pressure.

The iteration process for bottomhole pressure is as follows:

1. Guess bottomhole pressure (p_{wf}^{k}).
2. Calculate viscosity and z-factor at average pressure (p_{avg}).
3. Calculate new bottomhole pressure (p_{wf}^{k+1}) using Eq. 4.5. If the calculated p_{wf} is negative (unrealistic), the program changes the operating condition to implement a constant minimum bottomhole pressure.
4. Test convergence of the bottomhole pressure value with tolerance (ϵ_{pwf}):

$$\frac{\left|p_{wf}^{k+1} - p_{wf}^{k}\right|}{p_{wf}^{k}} < \epsilon_{pwf} \tag{4.7}$$

5. If convergence is not achieved, set new a bottomhole pressure as a guess for the next iteration. Repeat Steps 2 to 4 until bottomhole pressure value convergences.

The flow chart for the constant gas rate operating condition is presented in Figure 36. After confirming that the specified gas flow rate is achievable, the rate is used to calculate material balance time.

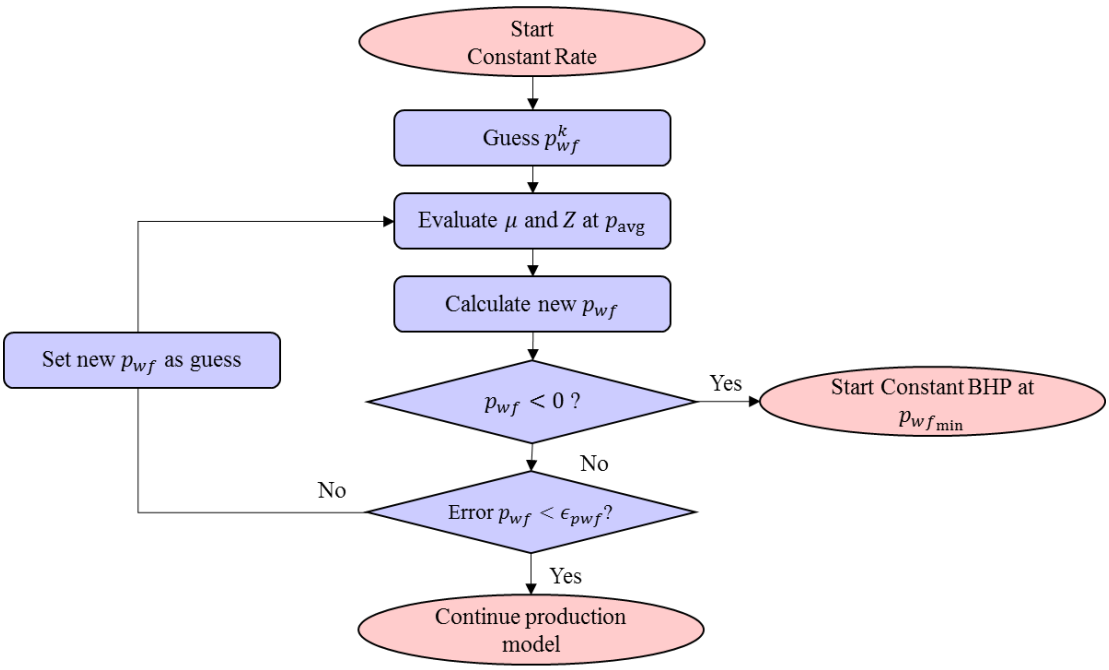

Figure 36 – Flow chart for constant-gas-rate operating condition. An iteration is required to obtain the correct value for bottomhole pressure that is associated with the specified gas rate.

Constant Drawdown Pressure

A constant drawdown pressure can be coded into the mechanistic model as a constant difference between reservoir pressure ($\bar{p}$) and bottomhole pressure (p_{wf}) to calculate the gas rate (q_g). The calculation in the constant-drawdown-pressure production method is similar to the constant-bottomhole-pressure constraint. The user sets the drawdown pressure (p_{draw}) and the program calculates the bottomhole pressure according to Eq. 4.8.

$$p_{wf} = \bar{p} - p_{\mathrm{draw}}^{\mathrm{MECH}} \tag{4.8}$$

where

p_{wf} = bottomhole flowing pressure (psi)

$\bar{p}$ = average reservoir pressure (psi)

$p_{\mathrm{draw}}^{\mathrm{MECH}}$ = drawdown pressure in the mechanistic model (psi)

Once the bottomhole pressure value is obtained, the gas rate is calculated using the pseudosteady-state flow equation presented in Eq. 4.3.

$$q_g = \frac{\left[m(\bar{p}) - m\left(p_{wf}\right)\right]}{C}$$

The flow chart to represent the constant drawdown operating condition is presented in Figure 37.

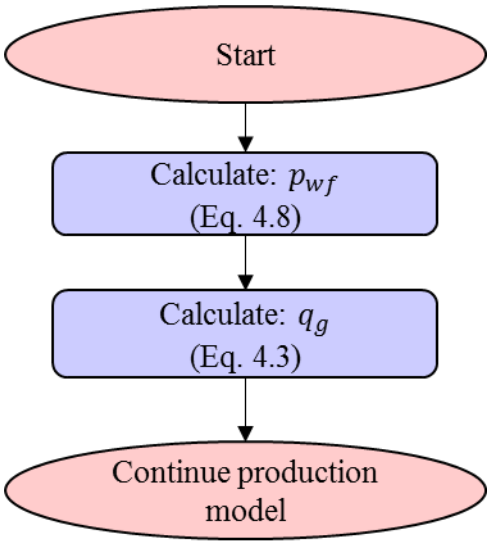

Figure 37 – Flowchart for constant drawdown pressure constraint.

4.2.3 Material Balance Time and Oil Rate

The final step in the coupling process is the calculation of production time. The new mechanistic model uses the volume of produced fluid from the CVD and the gas rate calculation to obtain production time. The calculation of material balance time (t_p) is described in Eq. 4.9, where *j* symbolizes the pressure step. The total production time at pressure step *j* is the summation of the production times calculated using Eq. 4.10.

$$\Delta t_p^j = \frac{\Delta G_p^j}{q_g^j} \tag{4.9}$$

$$t_p^j = \sum_{j=1}^{j} \Delta t_p^j \tag{4.10}$$

where:

Δt_p^j = production time (days) for pressure step *j*

ΔG_p^j = produced gas volume (MSCF) for pressure step *j* obtained from the CVD

q_g^j = calculated gas rate (MSCF/D) at pressure step *j*

Once we calculate the time for production of each pressure decrements, we can achieve a relationship between production and time and then plot the reservoir pressure, bottomhole pressure, gas rate, and volumes versus time to achieve a plot that is more familiar to reservoir engineers. We can also calculate the oil-phase production rate by dividing the produced oil volume by the material balance time, shown in Eq. 4.11.

$$q_o^j = \frac{\Delta N_p^j}{\Delta t_p^j} \tag{4.11}$$

where:

ΔN_p^j = produced oil volume (STB) for pressure step j obtained from CVD

q_o^j = produced oil rate (STB/day) at pressure step j

The general workflow of the coupling between the CVD mechanistic basis and the flow equation is presented in Figure 38.

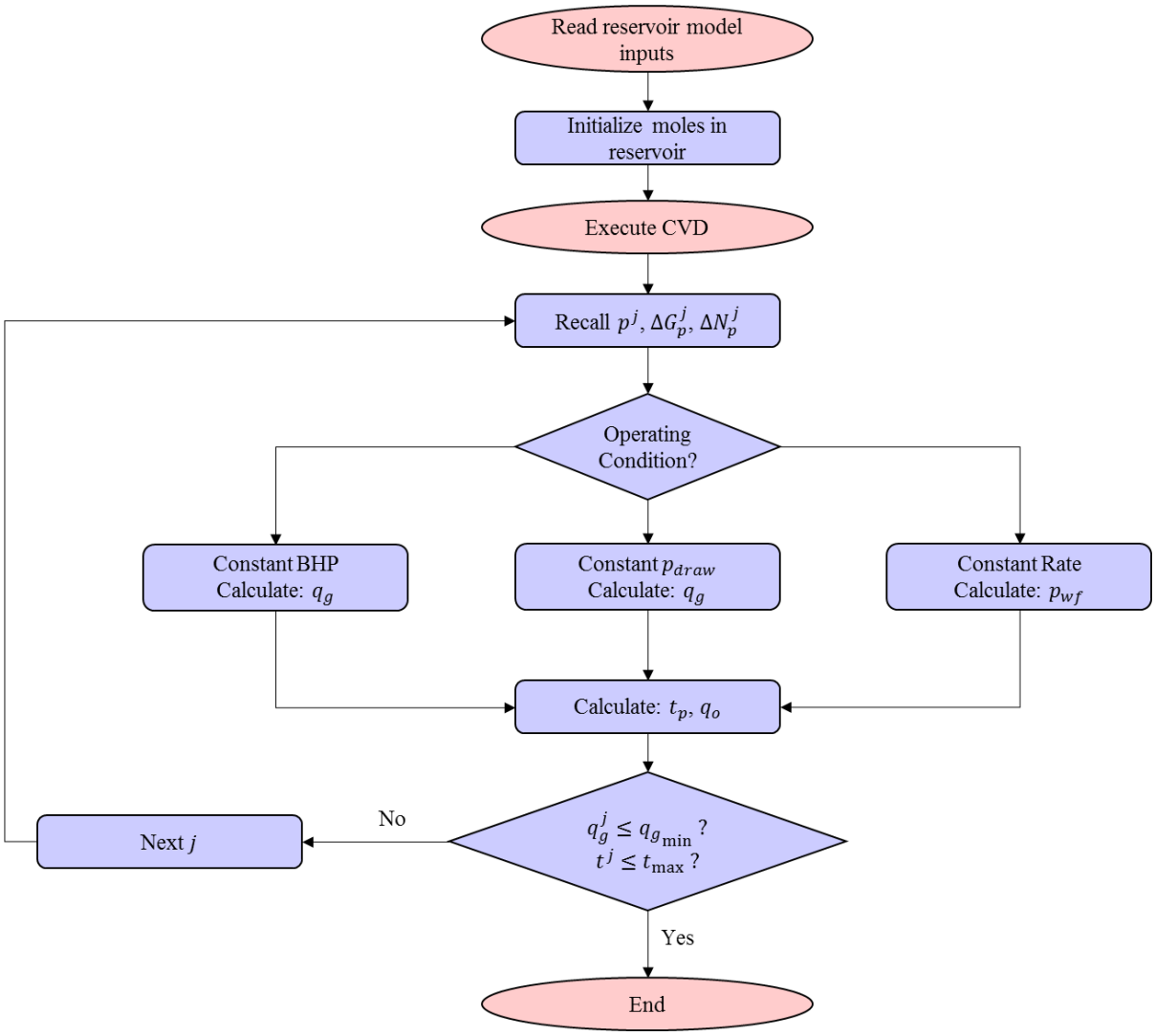

Figure 38 – General workflow of mechanistic model, coupling the CVD and production schemes to produce a relationship between production and time.

4.2.4 Comparative Study with Commercial Simulator

Next we compare the results produced by the developed mechanistic production model with a commercial compositional reservoir simulator. Three test cases were used to validate the results of the CVD-based model. The cases were designed to investigate the operating condition constraints programmed into the developed forecasting model. The three cases are:

1. Production at constant rate followed by minimum bottomhole pressure constraint
2. Production with a hydraulic fracturing completion and under a minimum-bottomhole-flowing-pressure constraint
3. Production at constant drawdown pressure

The fluid composition used in the simulation is described in Table 10, which is taken from the Eagle Ford gas-condensate window (Gong et al. 2013). This fluid composition was also used previously to validate the developed CVD test in Chapter III. To recall, the fluid composition is 65% C_1, 13% C_2, 6% C_3, followed by smaller amounts of heavier components. For this specified reservoir temperature (360°F), the dewpoint pressure is 3,560 psia.

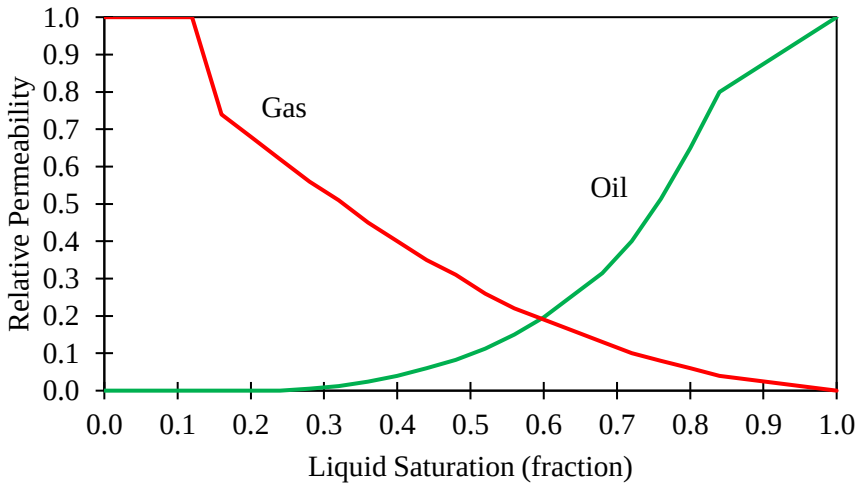

Figure 39 – Relative permeability curve created for the reservoir model in the comparison cases.

Synthetic homogeneous reservoir models were created for each comparison cases. I assume the reservoir model is fully saturated with hydrocarbon (gas) with zero water

saturation. The relative permeability saturation curve used in the model is described in Figure 39.

For each case, I compared the average pressure, bottomhole pressure, and gas and oil production between the mechanistic model and the commercial simulator. I calculated the average absolute error of the mechanistic model using Eq. 4.12 and Eq. 4.13.

$$e_i = \frac{\chi_i^{\mathrm{MECH}} - \chi_i^{\mathrm{SIM}}}{\chi_i^{\mathrm{SIM}}} \tag{4.12}$$

$$E = \sum_{i=1}^{N} |e_i| \cdot \frac{1}{N} \times 100\% \tag{4.13}$$

where

e_i = error between mechanistic forecast and commercial simulator

χ^{MECH} = value (p_{avg}, p_{wf}, $q_{g,o}$, G_p, N_p) from mechanistic model

χ^{SIM} = value (p_{avg}, p_{wf}, $q_{g,o}$, G_p, N_p) from commercial simulator

E = average absolute error

N = number of values

Case 1 – Constant Rate and Minimum Bottomhole Flowing Pressure Constraint

In this case, I compared production from a gas-condensate reservoir using a single well with constant gas rate of 100 MSCF/D and a minimum bottomhole flowing pressure of 2,800 psia. The well is producing from the center of the reservoir. The operational constraints of the producing well are summarized in Table 20. The well starts production above the dewpoint pressure (single-phase gas), and continues production below the dewpoint, into the two-phase region. The production is presented in Figure 40.

The synthetic reservoir model has an initial pressure of 5,200 psia and temperature of 360°F. This initial condition is above the dewpoint pressure of the reservoir fluid (Figure 40). The reservoir area is 80 acres, or 1,053-ft radius, with a thickness of 20 ft. This model

is a homogeneous reservoir permeability of 0.2 md and porosity of 20%. The properties for this synthetic reservoir model are summarized in Table 19. The model created for the commercial reservoir simulator a shown in Figure 41.

Table 19 – Reservoir properties of synthetic reservoir for comparison Case 1.

p_{res} (initial)	5200	psia
T_{res}	360	^{o}F
r_e	1053	ft
h	20	ft
k	0.2	md
ϕ	0.2	fraction
$Skin\ Factor$	0.0	dimensionless

Table 20 – Operational constraint for comparison Case 1.

r_w	0.365	ft
q_g	100	MSCF/D
p_{wf} minimum	2800	psia
q_g minimum	0.2	MSCF/D
p_{sc}	14.7	psia
T_{sc}	60	^{o}F

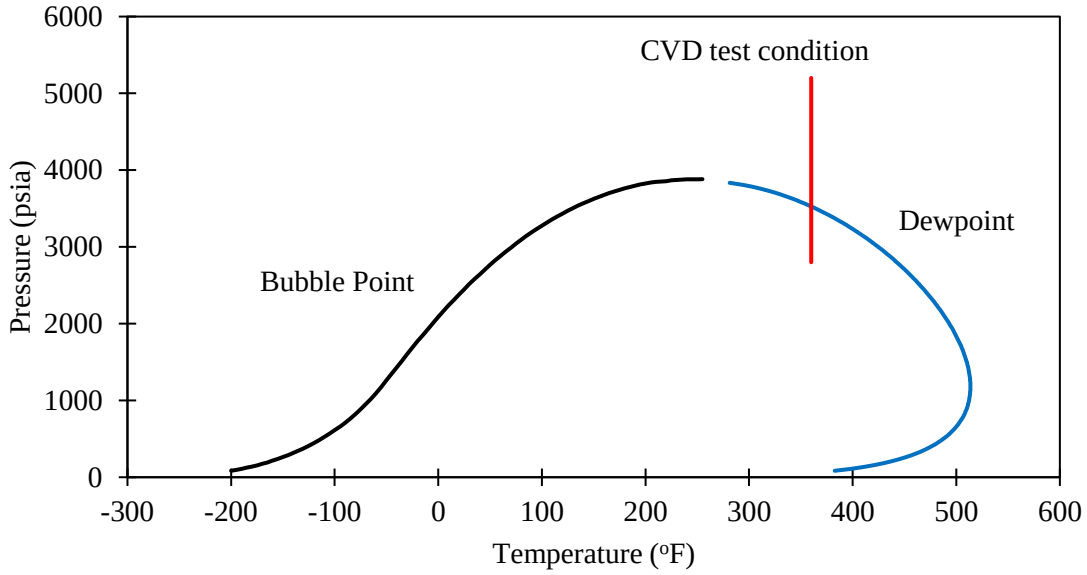

Figure 40 – Phase envelope of fluid used in comparison Case 1. Created using in-house simulator developed by Valbuena Olivares (2011).

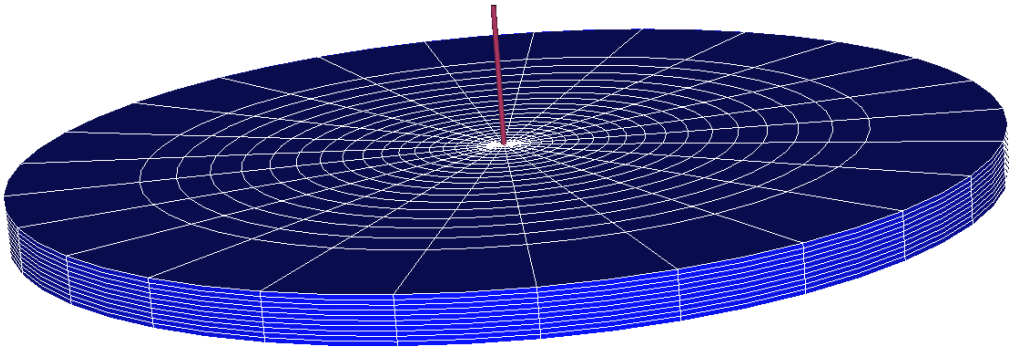

Figure 41 – Reservoir model created in the commercial reservoir simulator for comparison Case 1. The model is the same size as the mechanistic model (80 acres with r_e=1,053 ft). This model is a cylinder of height 20 ft (height exaggerated in the picture). The well is producing from the center of the cylindrical reservoir.

To create the mechanistic model forecast, I implemented the three CVD production options (described in Chapter III). To recall, these production options are the gas-only,

perfect-mixture, and relative-permeability schemes. The results from the CVD are coupled with the pseudosteady-state flow equation to create production forecasts. The predictions from the mechanistic model are compared to the results obtained from a commercial compositional reservoir simulator (Figure 42 through Figure 47).

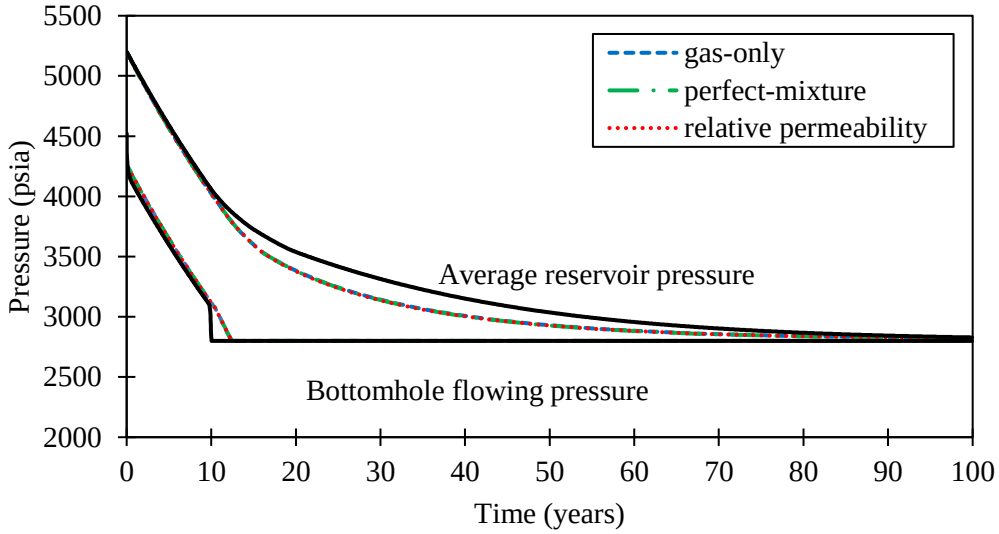

Figure 42 – Case 1: Comparison of average reservoir pressure and bottomhole pressure between developed mechanistic model and commercial reservoir simulator.

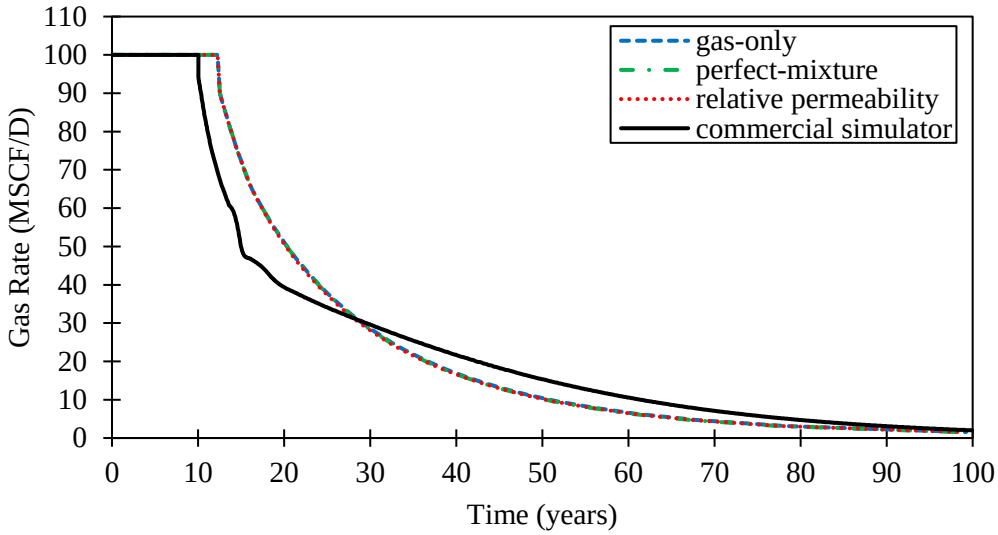

Figure 43 – Case 1: Comparison of gas production rate between developed mechanistic model and commercial reservoir simulator.

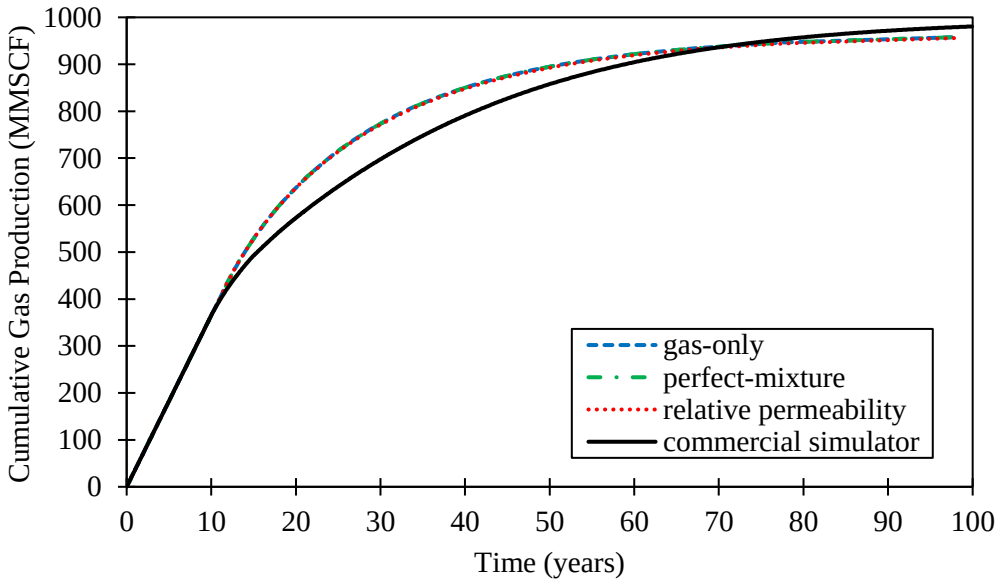

Figure 44 – Case 1: Comparison of cumulative gas production between developed mechanistic model and commercial reservoir simulator.

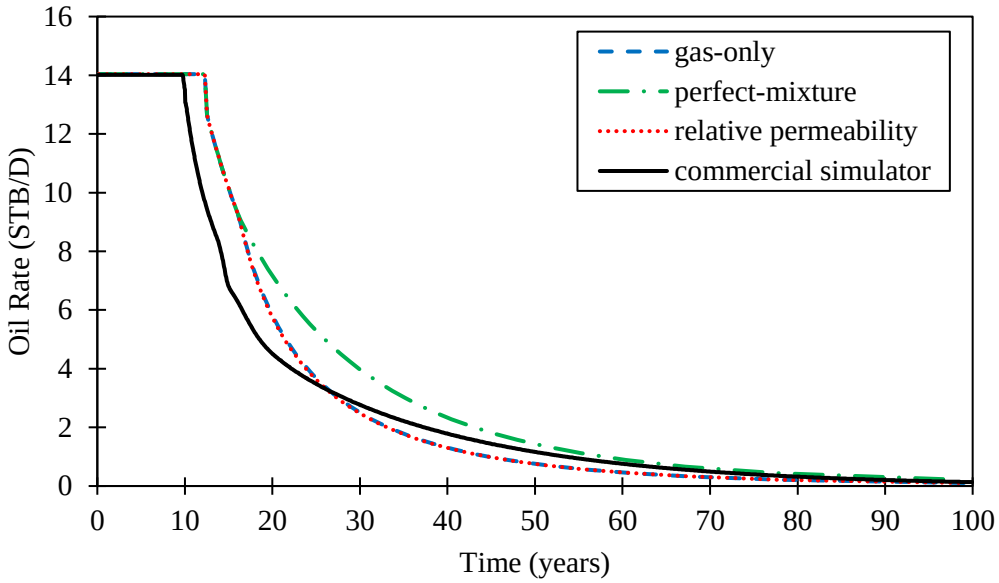

Figure 45 – Case 1: Comparison of oil production rate between developed mechanistic model and commercial reservoir simulator.

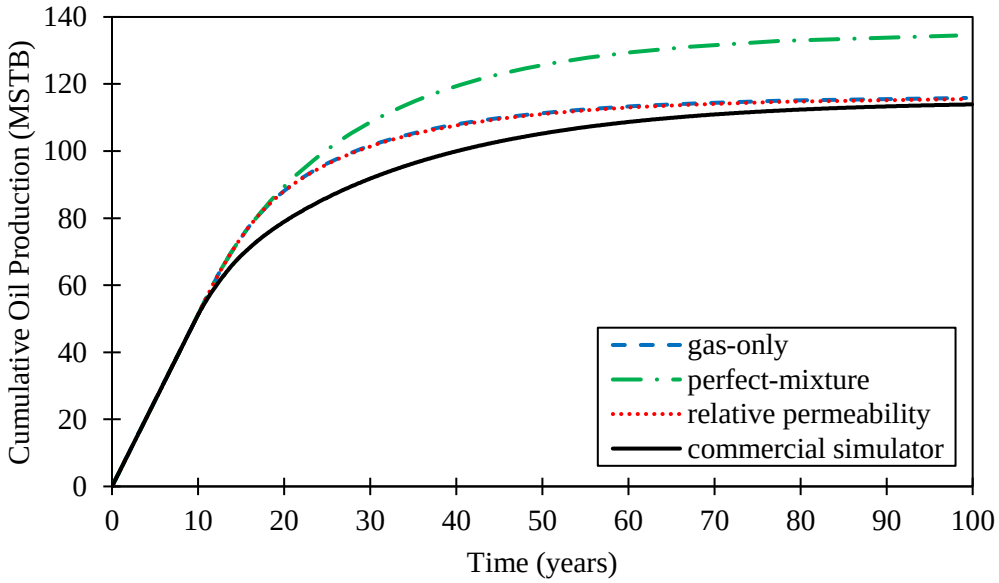

Figure 46 – Case 1: Comparison of cumulative oil production between developed mechanistic model and commercial reservoir simulator.

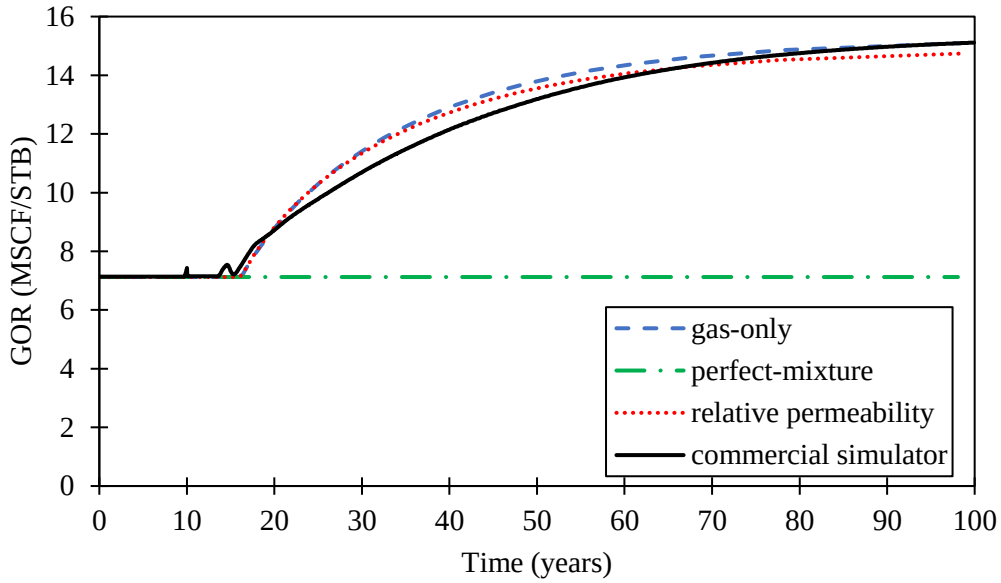

Figure 47 – Case 1: Comparison of produced gas/oil ratio between developed mechanistic model and commercial reservoir simulator.

The average absolute errors between the mechanistic and the commercial simulator forecast are tabulated in Table 21. In the gas-only production scheme, the mechanistic model provides good predictions for cumulative production of gas and oil, with 3.9% and 4.1% difference from the commercial simulator. The fluid rate predictions have a higher average error at 13.4% for gas rate and 14.4% for oil rate. Applying the relative-permeability production scheme provides forecasts similar to the gas-only production method. The perfect-mixture production scheme provides similar results for gas and pressure predictions, but it overestimates oil production.

The similarity between the gas-only and relative-permeability production can be explained by looking at the liquid saturation buildup in the CVD tank. Liquid saturation levels in the CVD tank did not reach critical oil saturation (S_{oc}); thus, the oil phase in the CVD tank was not produced. This led to majority gas production, which resulted in forecasts similar

to the gas-only production. This observation suggests that a majority of the oil produced comes from the gas phase that is brought to the surface.

Table 21 – Average error (Eq. 4.12) of the three production methods used for comparison Case 1. The gas-only and relative-permeability production provide similar error values, while the perfect-mixture production provides larger deviations.

Production Method	P_{avg}	q_g	G_p	q_o	N_p	GOR
Gas Only	2.0%	13.4%	3.9%	14.4%	4.1%	1.7%
Perfect Mixture	2.0%	13.6%	3.9%	19.9%	6.3%	9.8%
Relative Permeability	2.0%	13.5%	3.8%	14.3%	4.1%	1.5%

The forecast created by the developed mechanistic model follows the trend from the commercial reservoir simulator. The disagreement between the commercial simulator and the mechanistic model occurs as the average reservoir pressure decreases below the dewpoint pressure. The deviation is apparent in Figure 42, 10 years into the production forecast. In the forecasts of all other rates—gas (Figure 43), oil rate (Figure 45), cumulative oil (Figure 44), gas production (Figure 46)—and the disparity between the mechanistic model and the commercial simulator also begins after 10 years of production, when average reservoir pressure drops below the dewpoint.

We suspect this disagreement is due to the presence of multiphase flow caused by condensate accumulation in the near-wellbore area (condensate banking). This is simulated in the reservoir simulator as an increase liquid saturation in the grid blocks surrounding the wellbore (Figure 48a). The presence of condensate accumulation near the wellbore hinders the flow of gas because of the multiphase flow effect.

The CVD-based mechanistic production model developed in this study considers the reservoir as a single tank (Figure 48b). As the reservoir pressure falls below the dewpoint

pressures, liquid also accumulates in the CVD-based model. However, the saturation buildup is conceptually spread out through the entire CVD-based reservoir, thus not creating a condensate bank that significantly impacts the production.

To account for condensate banking, I developed an approach to estimate the liquid saturation of the condensate bank. The approach is based on a smaller CVD tank to represent the near-wellbore region. The saturation buildup in the small tank is based on a fluid-replenishment method. This allows for the accumulation of liquid that resembles the buildup in the reservoir simulator. Using the estimation of liquid saturation, I implemented a relative-permeability value in the calculation of the flow equation, thus improving the forecasts.

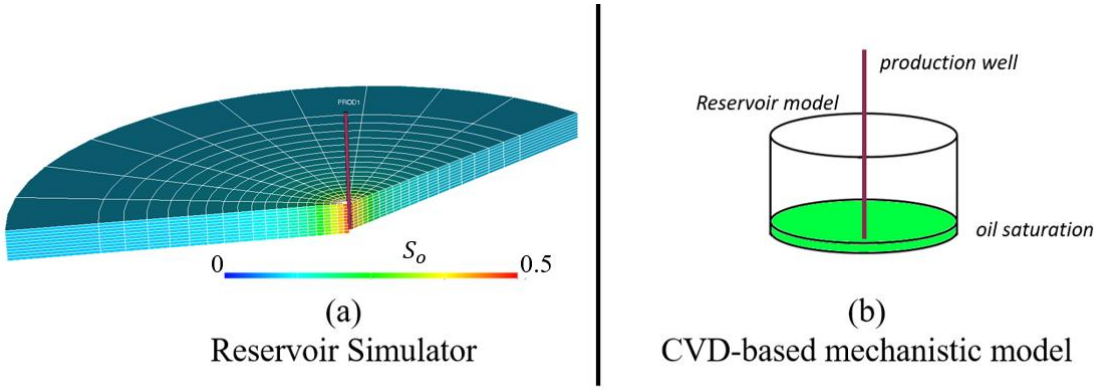

Figure 48 – a) Reservoir simulator grid blocks showing the increase of liquid (oil) saturation around the near-wellbore as the well is produced. b) Conceptual illustration of CVD-based mechanistic model. The oil saturation is conceptually spread out through the entire reservoir, thus not creating a condensate bank.

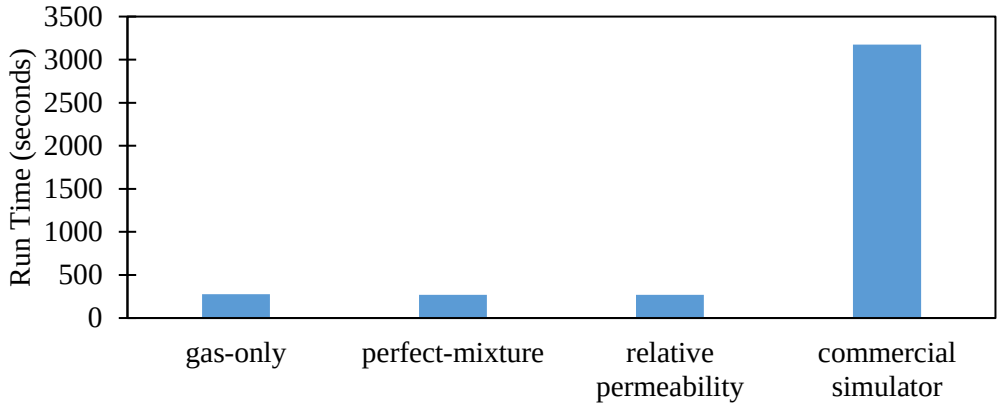

Figure 49 – Comparison of simulation times of developed mechanistic model and commercial simulator.

Figure 49 compares the simulation run times between the developed model and the commercial simulator. The developed model is orders of magnitude faster than the commercial model, achieving the goal of creating a fast method in forecasting gas-condensate production. Note that the time to complete the simulation run in the mechanistic model only depends on the size of the pressure decrements specified and the composition of the fluid. This contrasts with the commercial reservoir simulator, where reservoir properties such as size and permeability affect the time of the simulation run.

Case 2 – Hydraulic Fracturing with Minimum Bottomhole Pressure Constraint

The second comparison case used the same fluid and reservoir properties as Comparison Case 1, but added a well that is completed with a finite-conductivity hydraulic fracture with characteristics summarized in Table 22. The commercial simulator used a Cartesian reservoir with an area equivalent to the mechanistic model (80 acres) producing from a square reservoir with length of 1,866 ft. The well is located in the center of the reservoir and the hydraulic fracture has the same specifications as reported in Table 22. This reservoir model is presented in Figure 50. The hydraulically fractured well is produced at a constant bottomhole flowing pressure of 2,800 psia.

Table 22 – Case 2: Hydraulic fracture properties for comparison between mechanistic model and reservoir simulator.

Fracture Properties:		
Half-length (x_f)	111	ft
Permeability (k_f)	10000	md
Width (w_f)	0.04	ft
Calculated:		
Dimensionless fracture conductivity (C_{fD})	18	
Effective wellbore radius (r'_w)	51	ft
Equivalent skin factor (s_f)	-4.94	

Taking lessons from the first comparison case, here I only used the gas-only CVD production method to couple with the flow equation. I tested the relative-permeability CVD production scheme and produced the same results as the gas-only production method. The perfect mixture was not tested in this comparison case because it had been previously shown to overestimate the oil production. The results from the CVD-based mechanistic model are compared versus the results from the reservoir simulation in Figure 51 through Figure 54.

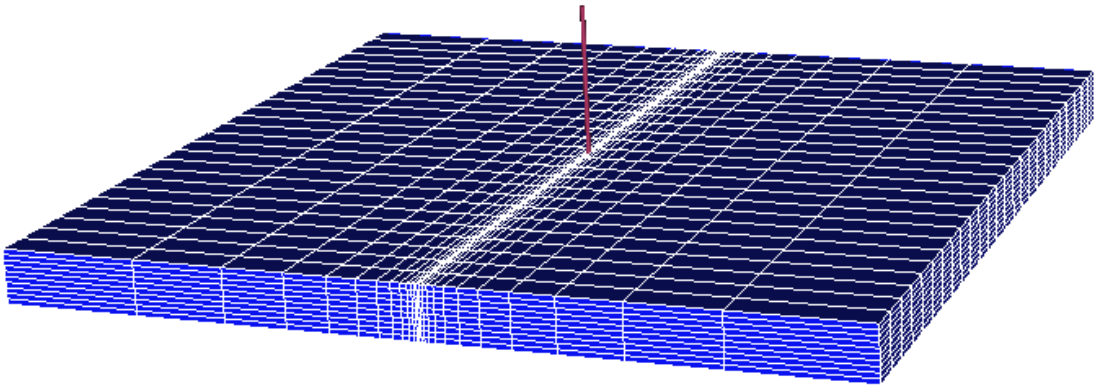

Figure 50 – Reservoir model created in the commercial reservoir simulator for comparison Case 2. The model is the same size as the mechanistic model (80 acres with x_e=1,866 ft). This model is a cube of height 20 ft (height exaggerated in the picture). The well is producing from the center of the square reservoir. A fracture with 10,000-md permeability, 0.04-ft width, and 111-ft half-length is modeled.

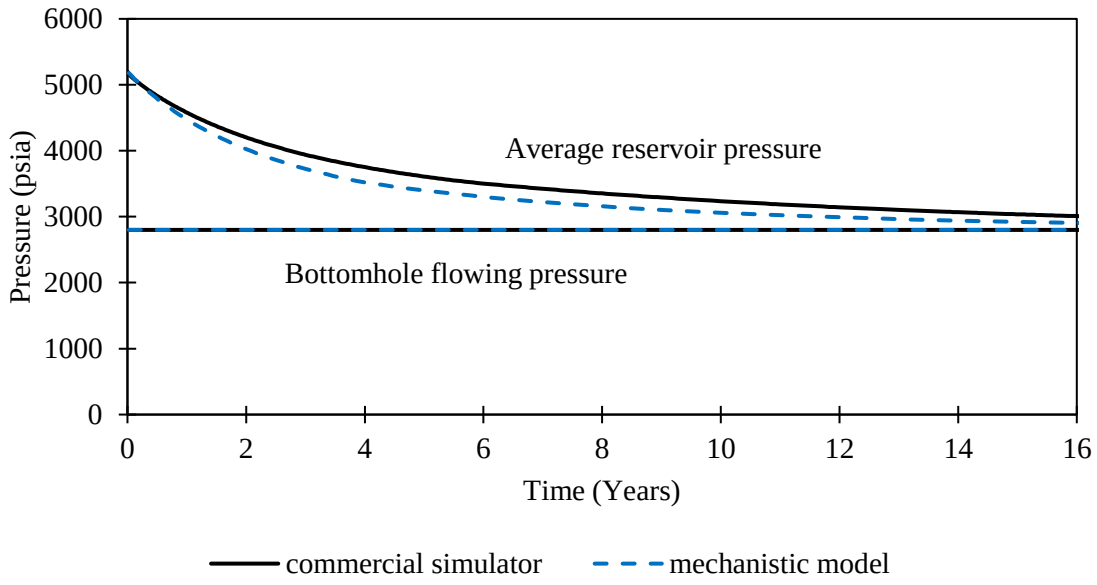

Figure 51 – Case 2: Comparison of reservoir pressure and bottomhole pressure between mechanistic model and reservoir simulator considering hydraulic fracturing completion.

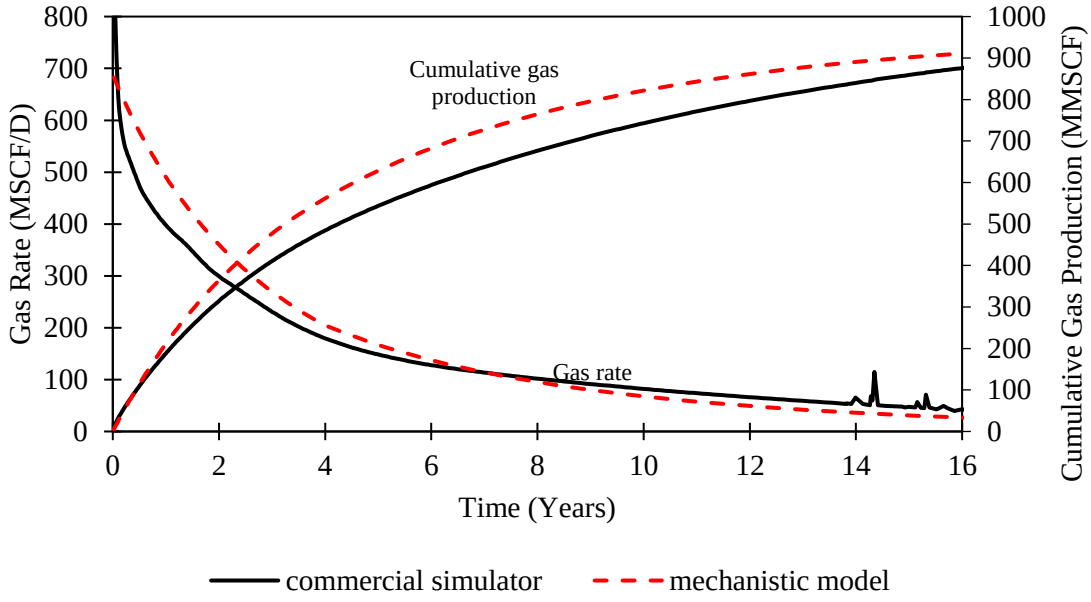

Figure 52 – Case 2: Comparison of gas rate and cumulative gas production between mechanistic model and reservoir simulator considering hydraulic fracturing completion.

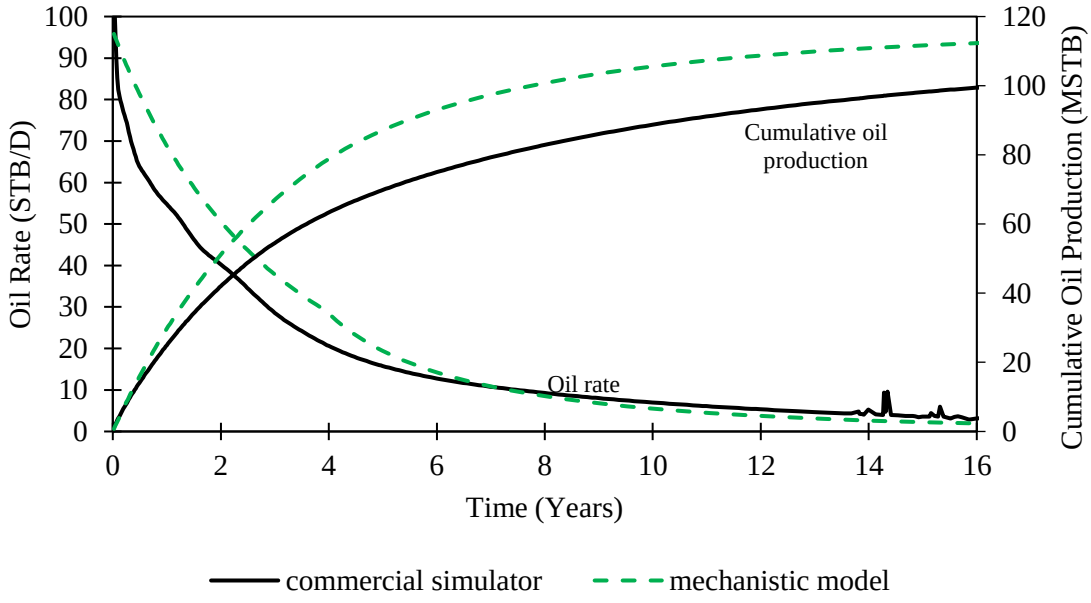

Figure 53 – Case 2: Comparison of oil rate and cumulative oil production between mechanistic model and reservoir simulator considering hydraulic fracturing completion.

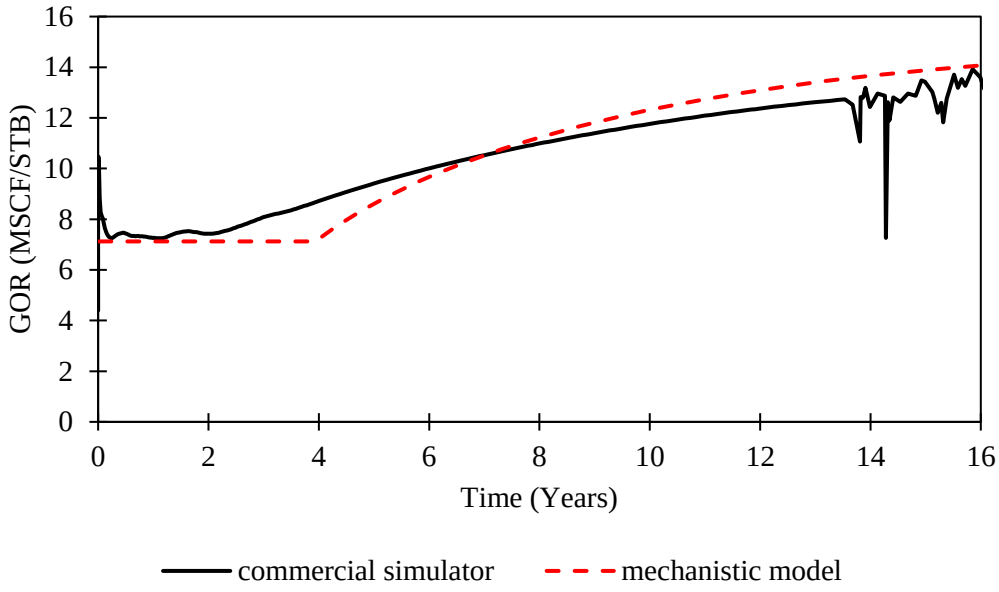

Figure 54 – Case 2: Comparison of gas/oil ratio between developed mechanistic model and commercial reservoir simulator considering hydraulic fracturing completion.

With the hydraulic fracturing completion, the mechanistic model was able to provide a forecast trend similar to the commercial simulator. However, the differences between the commercial simulator and the mechanistic model are larger than in the case where hydraulic fracturing is not considered (Case 1). The average absolute errors between the forecasts from the commercial and mechanistic models are tabulated in Table 23.

Table 23 – Average error of the three production methods used for comparison Case 2. Average error is calculated using Eq. 4.12.

	P_{avg}	q_g	G_p	q_o	N_p	GOR
Mechanistic model	3.7%	17.7%	13.3%	24.0%	19.3%	6.1%

From the comparison, the trends of the models are similar, but the mechanistic model tends to overestimate the production of hydrocarbons by about 19%, which is most apparent in the oil production forecast (Figure 53). The mechanistic model also estimates a higher flow rate than the reservoir simulator. This overestimation from the mechanistic model is also seen in the gas rate and gas cumulative forecasting.

We suspect this overestimation from the mechanistic model is due to the large calculated effective wellbore radius. With the fracture properties (Table 22) and the method presented by Meyer and Jacot (2005), the calculated effective wellbore radius (r'_w) is 51 ft. This calculated r'_w results in a very large equivalent flow area compared to the original wellbore radius (r_w) of 0.365 ft. This effective wellbore radius causes the mechanistic model production forecasts to be significantly higher than the commercial simulator forecasts. Using a smaller effective wellbore radius will serve to better match the predictions from the commercial simulator. Also, simulating the fracture as multiple wells in the mechanistic model may serve to better the production forecasts. This task remains for future work.

Case 3 – Constant Drawdown Pressure Constraint

The third case considered production from a well under constant drawdown pressure. Similar to previous cases, the composition of the reservoir fluid for this comparison is described in Table 10, taken from the Eagle Ford gas-condensate region. The reservoir and well operational constraints for the mechanistic and commercial model are detailed in Table 24. I considered a single well producing from the 40-acre reservoir area under a 300-psi constant drawdown pressure. The reservoir model created in the commercial simulator is presented in Figure 55. I compared the average reservoir pressure and the bottomhole flowing pressure, the gas and oil production rate, and cumulative rate (Figure 56 through Figure 60).

Table 24 – Reservoir properties and well operation constraint for constant drawdown comparison (Case 3)

p_{res} (initial)	5200	psia
T_{res}	360	^{o}F
r_e	745	ft
h	20	ft
k	0.2	md
ϕ	0.2	fraction
$Skin\ Factor$	0.0	dimensionless
r_w	0.365	ft
q_g	100	MSCF/D
p_{draw}	300	psi

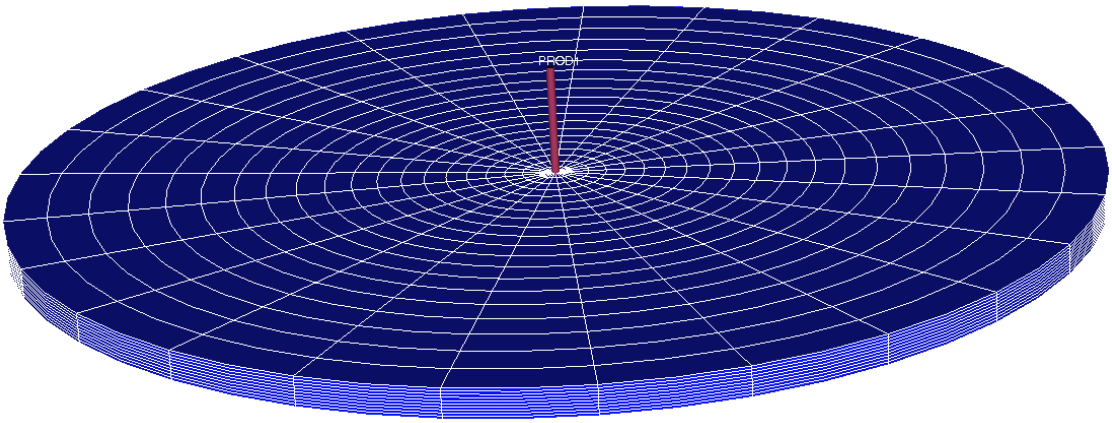

Figure 55 – Reservoir model created in the commercial reservoir simulator. The model is the same size as the mechanistic model (r_e=745 ft). This model is a cylinder of height 20 ft. The model is divided into 10 layers, 25 segments in the theta direction, and 20 in the radial direction.

.

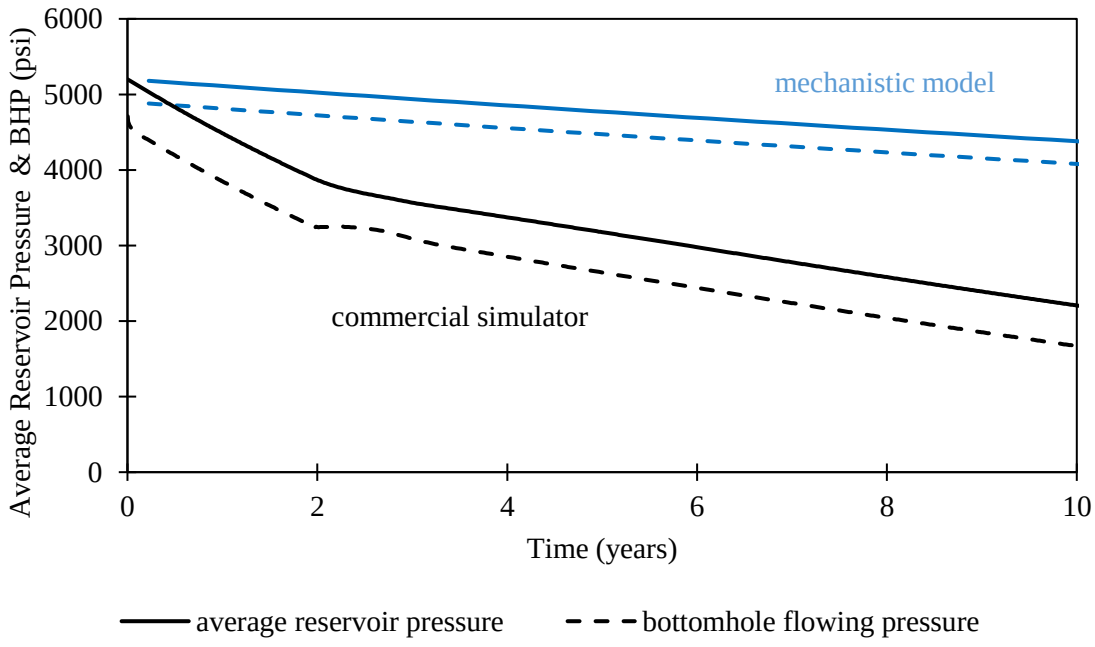

Figure 56 – Case 3: Comparison of reservoir pressure and bottomhole pressure between the mechanistic model and the reservoir simulator under constant drawdown pressure.

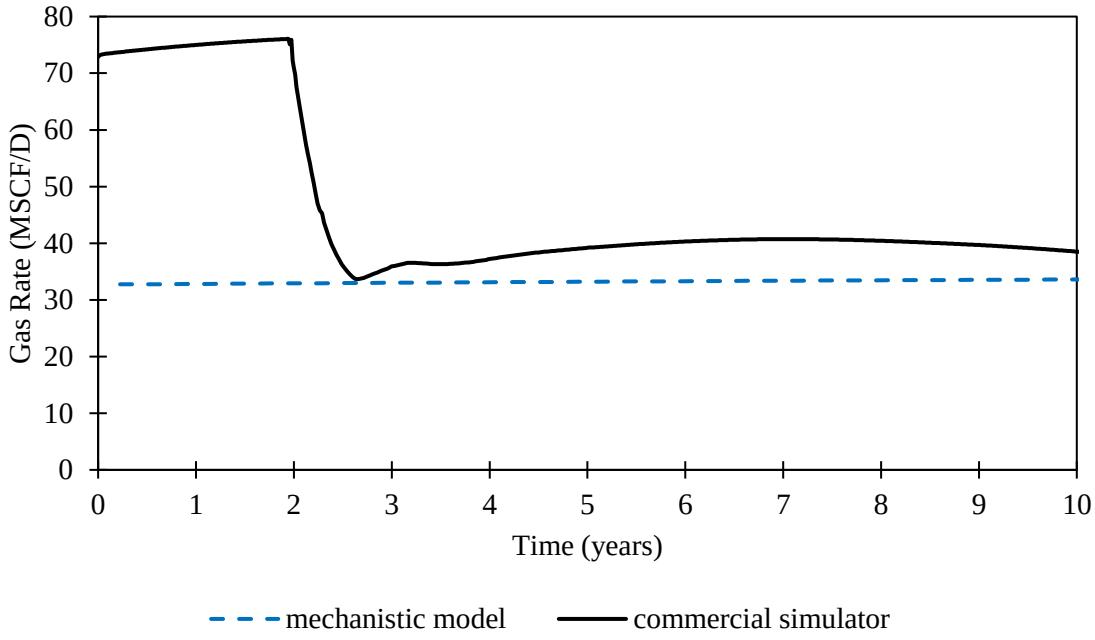

Figure 57 – Case 3: Comparison of gas rate between the mechanistic model and the reservoir simulator under constant drawdown pressure.

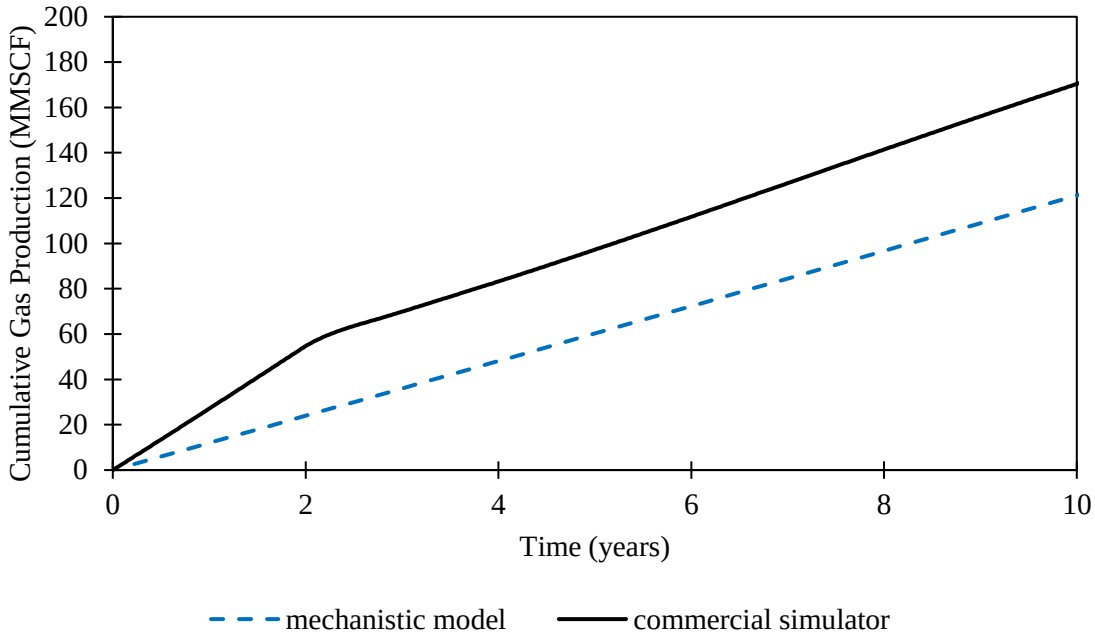

Figure 58 – Case 3: Comparison of cumulative gas production between the mechanistic model and the reservoir simulator under constant drawdown pressure.

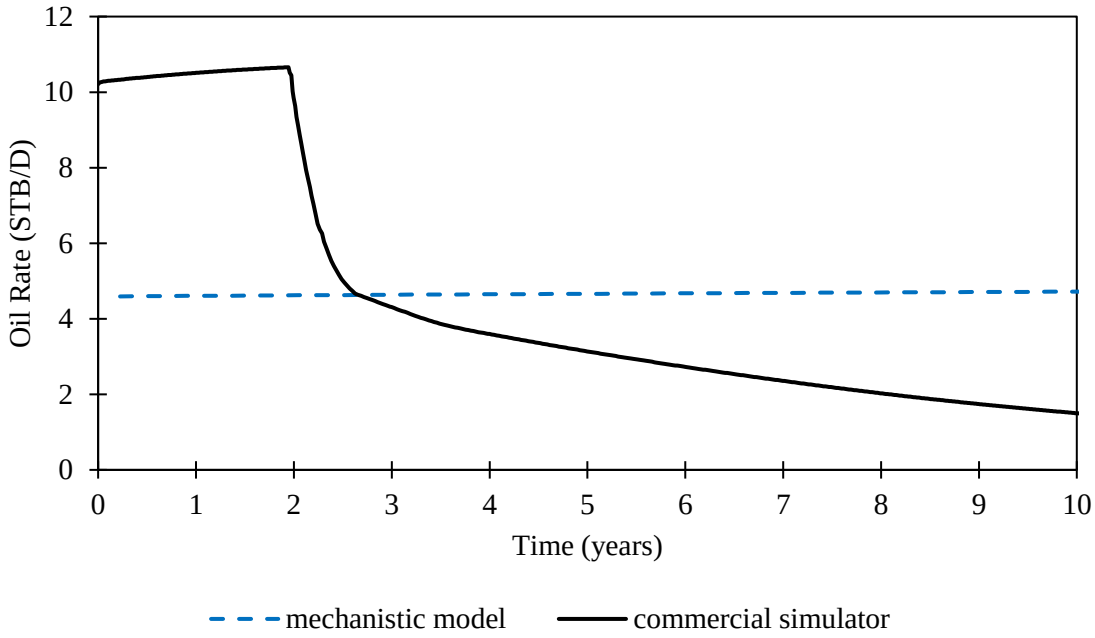

Figure 59 – Case 3: Comparison of oil rate between the mechanistic model and the reservoir simulator under constant drawdown pressure.

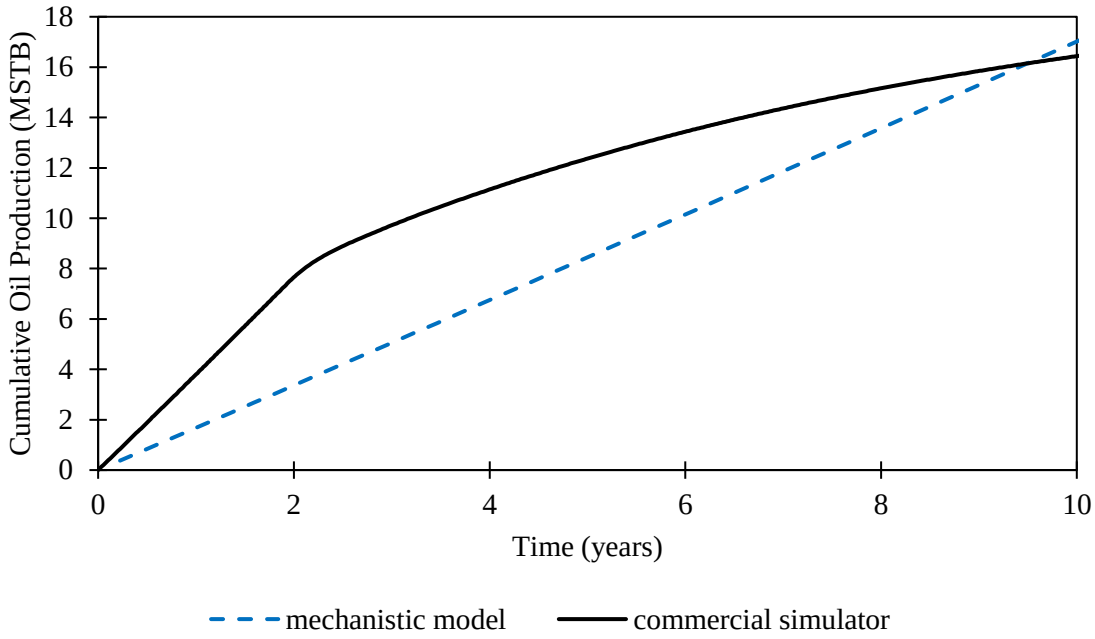

Figure 60 – Case 3: Comparison of cumulative oil production between the mechanistic model and the reservoir simulator under constant drawdown pressure.

The difference between the results from the commercial simulator and our developed mechanistic model was significant. The mechanistic model was not able to produce the same trend as the commercial reservoir simulator. This disagreement is caused by different definition of drawdown between the commercial reservoir simulator and the mechanistic model (Figure 61).

In the mechanistic model, the drawdown pressure is the difference between the average reservoir pressure ($\bar{p}$) and the bottomhole pressure (p_{wf}). In the gridded reservoir simulator, the drawdown pressure is defined as the difference between the pressure of the grid block adjacent to the well (p_{cell}) and the bottomhole pressure (p_{wf}) as shown in Figure 61. This causes a discrepancy between the drawdown pressure set for the reservoir simulation model and the mechanistic model. The result is that the reservoir simulation experiences a larger pressure difference between average and bottomhole pressure for the same "drawdown" pressure value. These problems are detailed in the comparative study (Case 3).

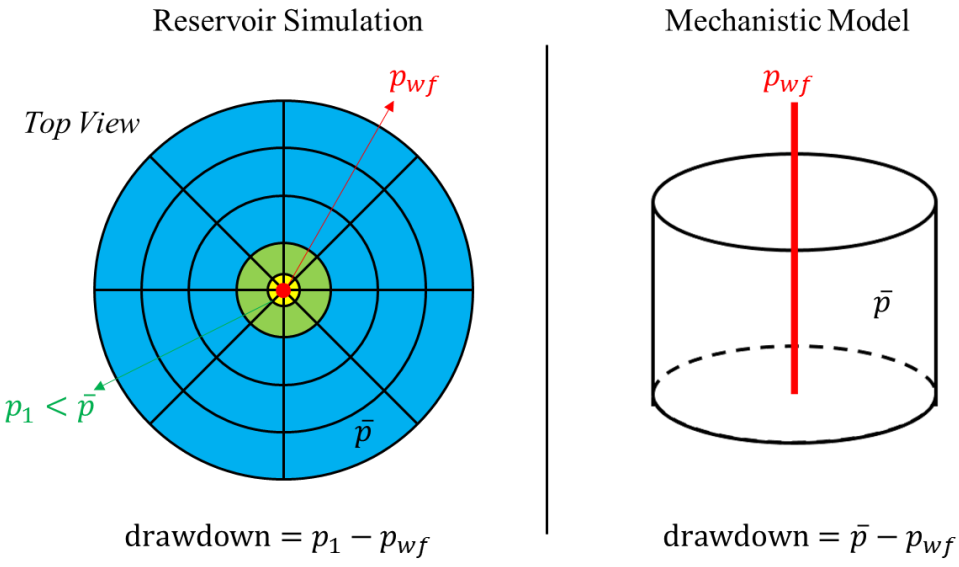

Figure 61 – Different definition of drawdown pressure between reservoir simulation and mechanistic model.

Pseudodrawdown

To remedy for this disparity between the mechanistic model drawdown definition and the commercial reservoir simulator, I introduced a pseudodrawdown pressure based on the relationship between average reservoir pressure and bottomhole flowing pressure in the reservoir simulator, as defined in Eq. 4.14. This definition is similar to the drawdown definition for the mechanistic model (Eq. 4.8).

$$p_{pd} = \bar{p}^{\mathrm{COM}} - p_{wf}^{\mathrm{COM}} \tag{4.14}$$

where

p_{pd} = pseudodrawdown pressure

$\bar{p}^{\mathrm{COM}}$ = average reservoir pressure obtained from the commercial simulator

p_{wf}^{COM} = bottomhole flowing pressure obtained from the commercial simulator

Figure 62 is a graph of pseudodrawdown versus time, created from the commercial simulator results. The results in Figure 62 are based on a homogeneous reservoir model of 0.2-md permeability with an area of 40 acres and a height of 20 ft (Table 24). The composition of the reservoir fluid is from the Eagle Ford fluid described in Table 10. I implemented five drawdown pressures to a well producing from the center of the cylindrical reservoir model.

From Figure 62, we observe two main behaviors of the pseudodrawdown:

1. Each of the five drawdown pressures implemented in the commercial model has two distinct stabilized values for pseudodrawdown. In the early life of the well's production, the pseudodrawdown value stabilizes at a higher value. This is followed by a second stabilized pseudodrawdown value that is lower. Further observation concludes that the pseudodrawdown behavior can be divided into times before and after average reservoir pressure falls below the dewpoint pressure. The decrease in

pseudodrawdown value may be attributed to the existence of two-phase fluid in the reservoir or liquid buildup in the near wellbore.

2. The differences between the stabilized pseudodrawdown values are more prominent for the larger drawdown pressure. For the 500-psi drawdown pressure implemented in the commercial simulator, the pseudodrawdown has a difference of 180 psi between the first and second stabilized sections, while for the 100-psi drawdown pressure, we obtain only a 20-psi difference between the two stabilized sections.

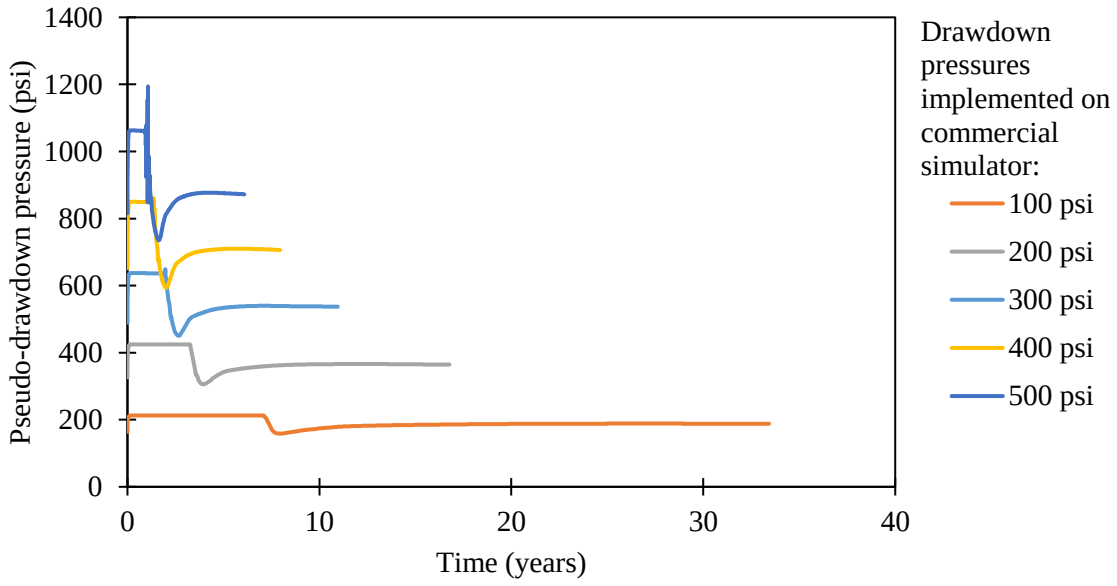

Figure 62 – Pseudodrawdown pressure of a well producing at a constant drawdown pressure in the center of a 40-acre gas-condensate reservoir using commercial reservoir simulator.

For this study, I averaged the values of the pseudodrawdown pressures and plotted them versus the drawdown implemented in the commercial model, ignoring the different drawdown values before and after bottomhole pressure falls below the dewpoint (Figure

63). This produces a linear relationship between reservoir simulation drawdown and average pseudodrawdown pressure, shown in Eq. 4.10.

$$\overline{p_{pd}} = 1.768 p_{\mathrm{d}}^{\mathrm{COM}} - 15.51 \tag{4.15}$$

$$\overline{p_{pd}} = \frac{\sum_{i=1}^{N_{pd}} p_{pd_i}}{N_{pd}} \tag{4.16}$$

where:

$\overline{p_{pd}}$ = average pseudo-drawdown pressure (psi)

$p_{\mathrm{d}}^{\mathrm{COM}}$ = drawdown pressure of reservoir simulation (psi)

N_{pd} = number of pseudo-drawdown pressure

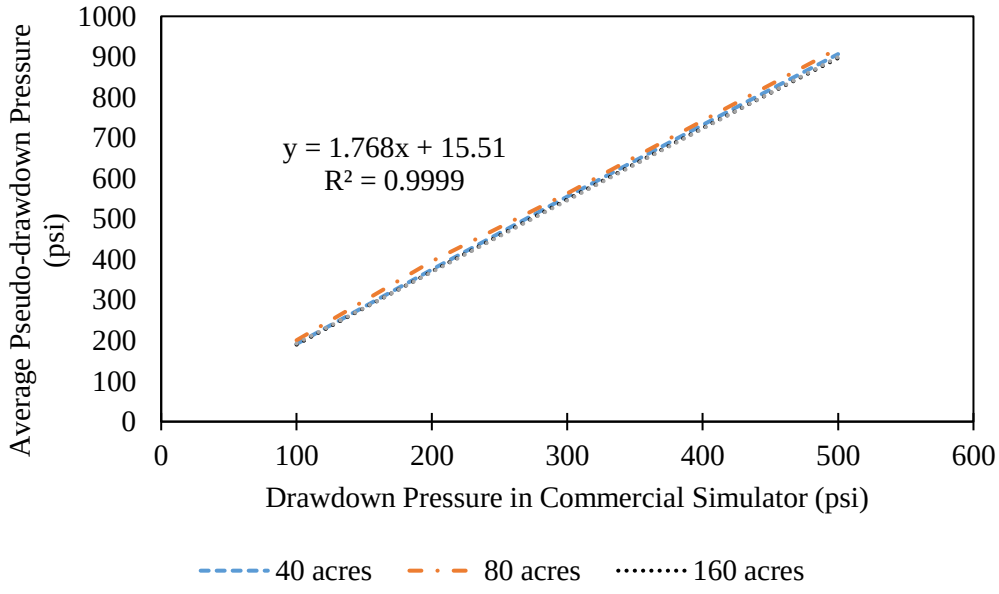

Figure 63 – Average pseudodrawdown pressure versus drawdown pressure implemented in the commercial model. The study was conducted using three reservoirs of different sizes, while imposing five different constant-drawdown-pressure values in the commercial simulator. Reservoir size seems to not affect the relationship of average pseudodrawdown and drawdown pressure.

I also investigated the effect of permeability on the relationship between average pseudodrawdown pressure and drawdown pressure. For this study, I used the same 40-acre homogeneous reservoir and varied the permeability and found that the relationship between average pseudodrawdown pressure and drawdown pressure is also not affected by the different permeability (Figure 64).

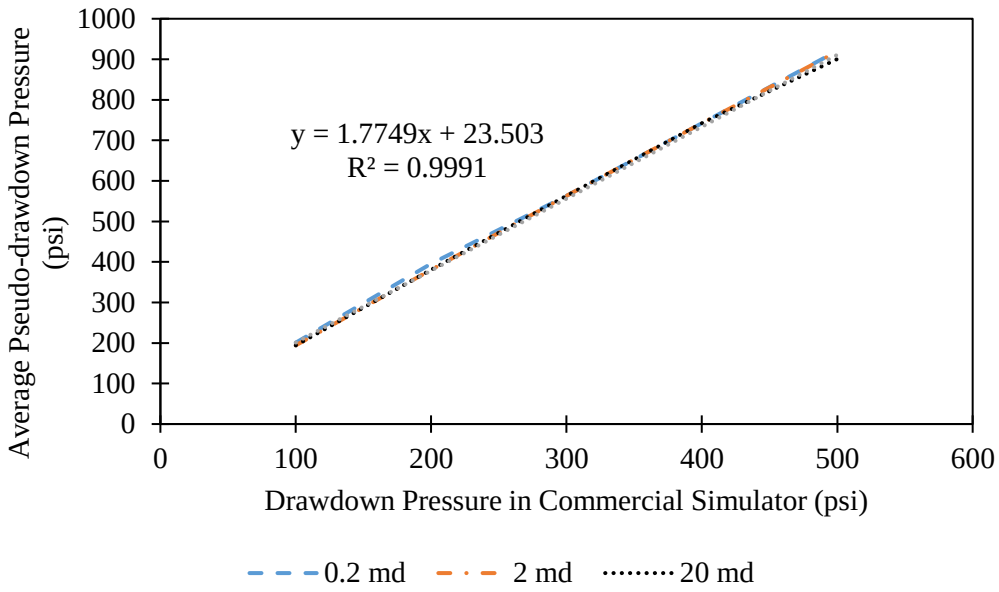

Figure 64 – Pseudodrawdown pressure versus drawdown pressure at different permeability values.

Using Pseudodrawdown Pressure

The pseudodrawdown pressure was implemented to obtain a better forecast comparison with the commercial reservoir simulator. The pseudodrawdown pressure is calculated using Eq. 4.14, which gives the value of 555 psi used as the drawdown pressure in the mechanistic model. In the forecasts comparing the pseudodrawdown pressure value with the results from the commercial reservoir simulator (Figure 65 through Figure 69), the commercial simulator is still under a drawdown pressure of 300 psi.

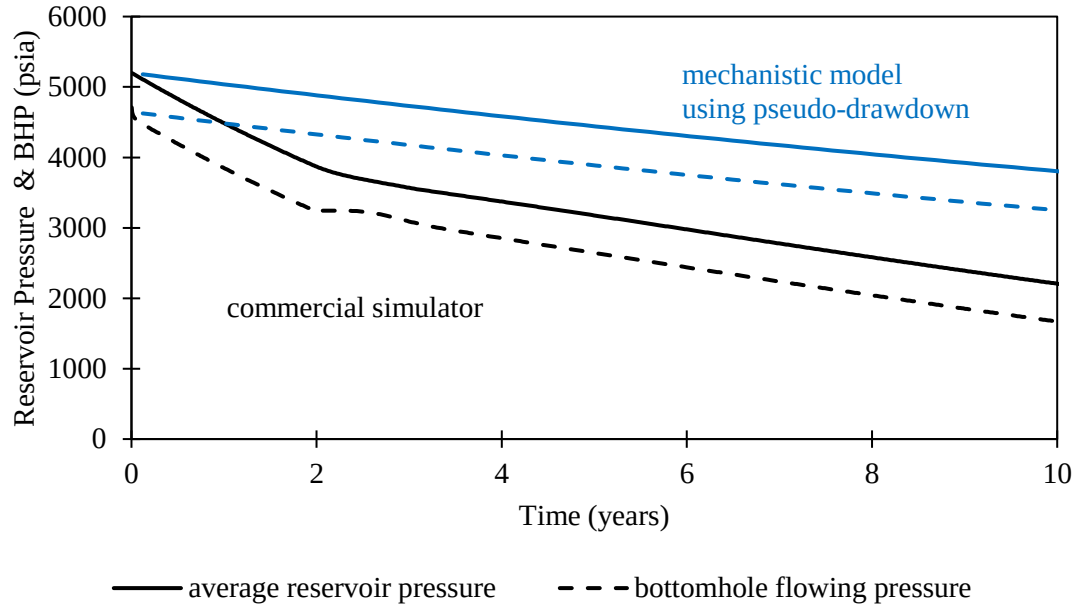

Figure 65 – Case 3 with pseudo-drawdown pressure: Comparison of reservoir pressure and bottomhole pressure between the mechanistic model and the simulator under constant drawdown pressure. The comparison shows that the mechanistic model cannot produce the same trend as the commercial model.

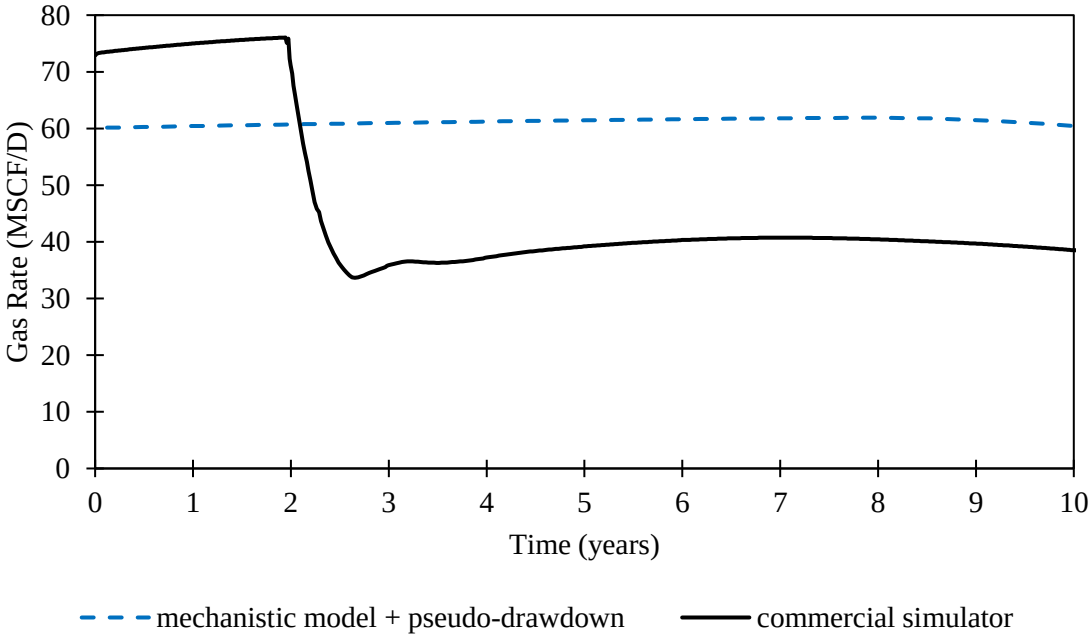

Figure 66 – Case 3 with pseudodrawdown pressure: Comparison of gas rate for the mechanistic model and the reservoir simulator under constant drawdown pressure.

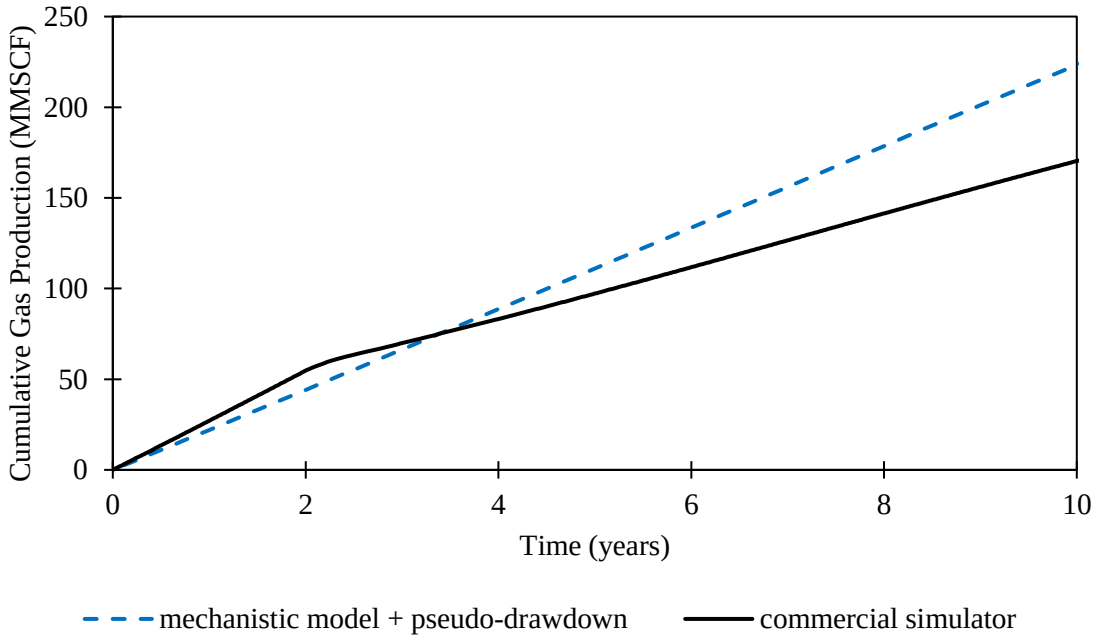

Figure 67 – Case 3 with pseudodrawdown pressure: Comparison of cumulative gas production between the mechanistic model and the reservoir simulator under constant drawdown pressure.

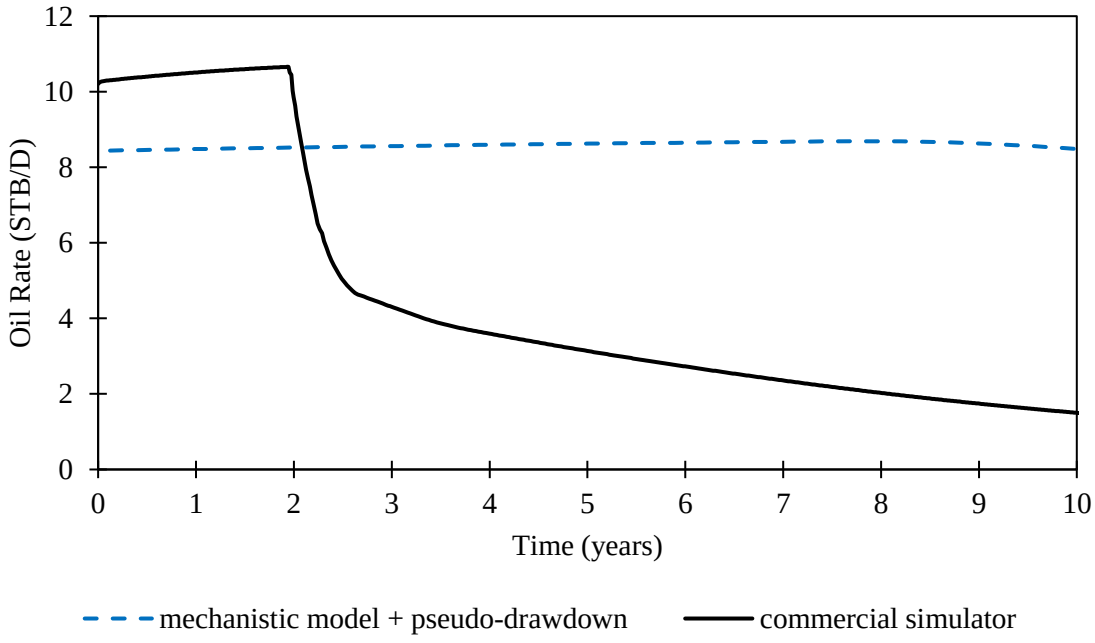

Figure 68 – Case 3 with pseudodrawdown pressure: Comparison of oil rate under constant drawdown pressure.

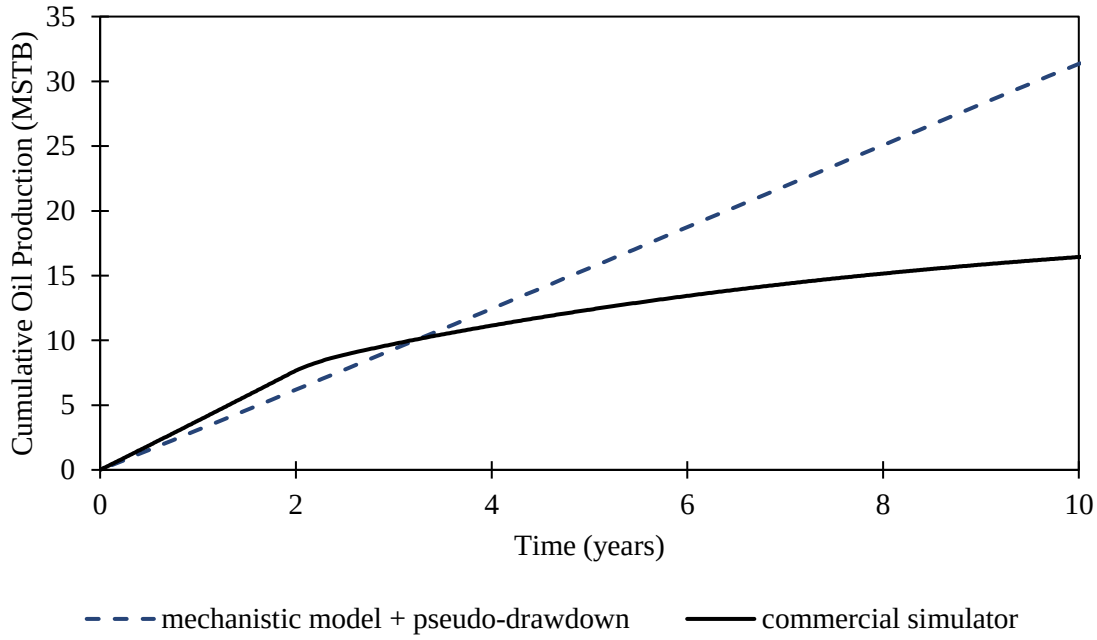

Figure 69 – Case 3 with pseudodrawdown pressure: Comparison of cumulative oil production under constant drawdown pressure.

Using the pseudodrawdown pressure in the mechanistic model still led to large deviations in results compared to the commercial simulator. The main reason for the deviation is apparently caused by averaging the value of pseudodrawdown before and after average reservoir pressure falls below dewpoint pressure (Figure 62). Further improvements can be made by implementing different pseudodrawdown pressures depending on the average reservoir pressure.

In summary, the mechanistic model currently is not able to accurately forecast results for a well producing at constant drawdown pressure. This is due to the different definition and implementation of drawdown pressure between the commercial reservoir simulator and the mechanistic model. The mechanistic model represents the reservoir as a single cylindrical tank, while the reservoir simulator divides the reservoir into multiple grid blocks. Implementing the pseudodrawdown pressure was not enough to correct the results.

For future work, we recommend developing a multiple pseudodrawdown pressure to adjust the forecasting results. Also, further work is needed to determine how to accurately model production from a well under drawdown pressure. This might include studies on the effects of the reservoir fluid composition and initial reservoir pressure.

4.3 Functionalities of CVD-Based Forecasting

4.3.1 Well Spacing

Well spacing is important to economically drain the reservoir. With this information, operators may choose the desired spacing for the field plan of development. Forecasting reservoirs of different sizes using the mechanistic model allows users to graph the recovery factor of gas and oil versus time and contribute to the reservoir management process.

The example below forecasts a well producing from different reservoir sizes and plots the recovery factors versus time. The reservoir properties are from comparison Case 1; the reservoir area (spacing) is 40 acres, 80 acres, and 160 acres. The well is producing at a constant bottomhole flowing pressure of 2,800 psi from the center of the well. The gas recovery factor is calculated using Eq. 4.17, while the oil recovery factor is calculated using Eq. 4.18. Here, the initial gas and oil in place are determined by flashing the initial overall fluid to standard conditions.

$$RF_g = \frac{G_p}{G_{\text{initial}}} \cdot 100\% \tag{4.17}$$

$$RF_o = \frac{N_p}{N_{\text{initial}}} \cdot 100\% \tag{4.18}$$

where

$RF_{g,o}$ = gas (g) or oil (o) recovery factor (%)

G_p = gas cumulative production (MMSCF)

G_{initial} = initial gas in-place (MMSCF)

N_p = oil cumulative production (MSTB)

N_{initial} = initial oil-place (MSTB)

The example of recovery factor comparison is presented in Figure 70 and Figure 71. As expected, the smaller spacing (reservoir area) results in faster oil and gas recovery. The advantage to the mechanistic model is that it quantifies and estimates production using different spacing quickly, thus making the decision process easier. Using the mechanistic model, this recovery factor can be calculated quickly and the results can be used to contribute to the development plan for producing from gas-condensate reservoirs.

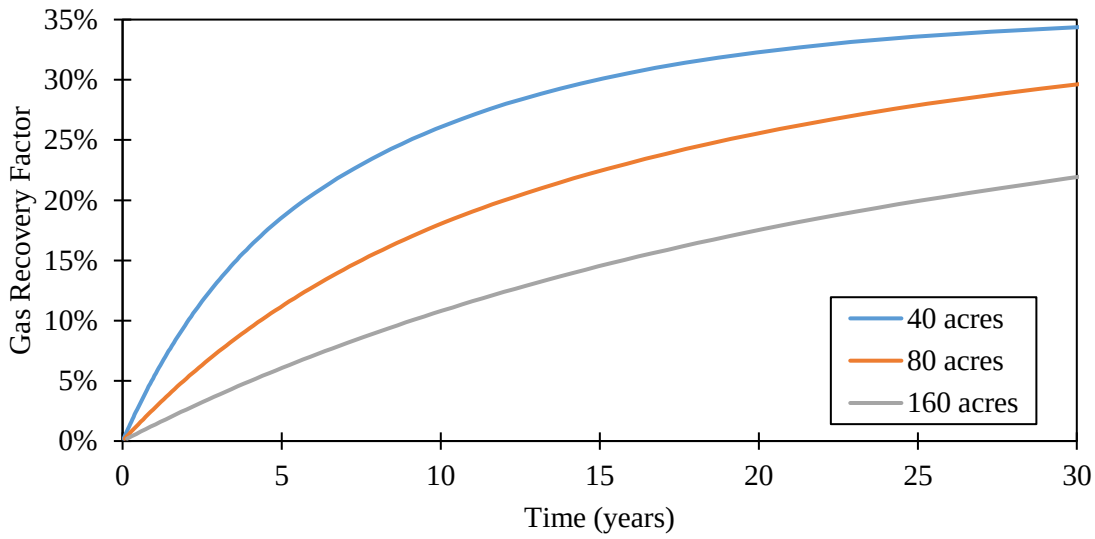

Figure 70 – Gas recovery factor considering different well spacings. The reservoir properties are taken from comparison Case 1.

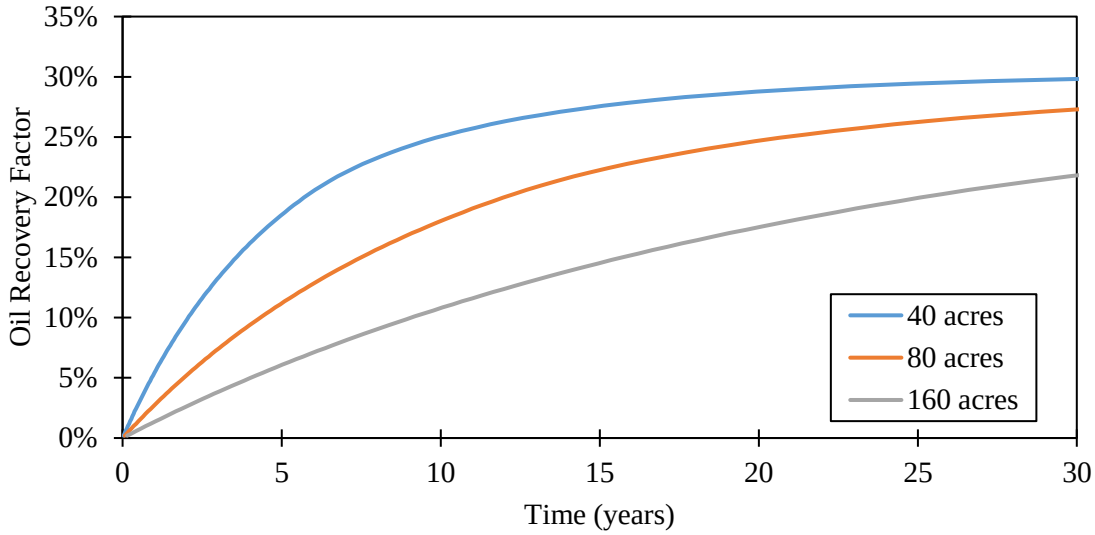

Figure 71 – Oil recovery factor considering different well spacings. The reservoir properties are taken from comparison Case 1.

4.3.2 Mechanistic Decline Curve

The mechanistic model can also be used to predict gas and oil production. Using the commercial simulator, I created two data sets with the reservoir and fluid properties presented in Table 19 and Table 10, respectively. For the examples, I simulated the well under constant bottomhole flowing pressure (p_{wf}), 2,000 psi and 3,800 psi, for a 30-year period and compared the decline curves against the Arps (1945) decline model.

The Arps decline curve assumes the well is producing under constant bottomhole pressure and in the boundary-dominated flow regime. This condition allows the Arps decline parameter (b) to be constant. The Arps exponential model is presented in Eq. 4.20, while the Arps hyperbolic decline model is presented in Eq. 4.19. The initial decline rate (D_i) as presented in Eq. 4.21 can be obtained from production history data. If production rate and time data are available, the D_i value can be obtained from the slope of the straight line on a semi-log plot.

$$q = q_i e^{-D_i t} \tag{4.19}$$

$$q(t) = \frac{q_i}{(1 + bD_i t)^{\frac{1}{b}}} \tag{4.20}$$

$$D_i = -\frac{d(\ln q)}{dt} = \frac{\ln\left(\frac{q_1}{q_2}\right)}{t_2 - t_1} \tag{4.21}$$

where

$q(t)$ = rate at time t

q_i = initial rate

b = constant decline parameter

D_i = initial decline rate

t = time

In the examples below, the Arps decline curves are empirically fitted to the production data. Mimicking the forecasts created by engineers in real life, knowledge of production history was restricted to 2 years, 6 years, and 10 years. Using only the production data provided for the specified amount of time, I created production forecasts with the Arps decline equation.

Forecasting Example 1: Constant Bottomhole Flowing Pressure 2,000 psi

The objective of these examples are to illustrate the capability of the mechanistic model to predict gas and oil production from gas-condensate reservoirs. In the first case, the well is producing under constant bottomhole pressure of 2,000 psi. Hydrocarbon production was forecasted for a 30-year period using the Arps decline model and the mechanistic model. For the Arps decline curve, I attempted to match and predict the production using 2, 6, and 10 years' worth of production data. The Arps matching was done empirically to obtain the closest match to the data available and project that decline curve into the future.

The log production rate is plotted versus time in Figure 72 for a 2-year production history. In the semi-log plot, the straight line indicates boundary-dominated flow. The flow period

prior to the straight line is ignored because the reservoir is still in the transient flow period. The decline rate is calculated from any two points on the straight line using Eq. 4.21. For the example in Figure 72, the initial decline rate is

$$D_i = \frac{\ln\left(\frac{q_1}{q_2}\right)}{t_2 - t_1} = \frac{\ln\left(\frac{267.66}{198.76}\right)}{1.91 - 0.57} = 0.22/\text{year}$$

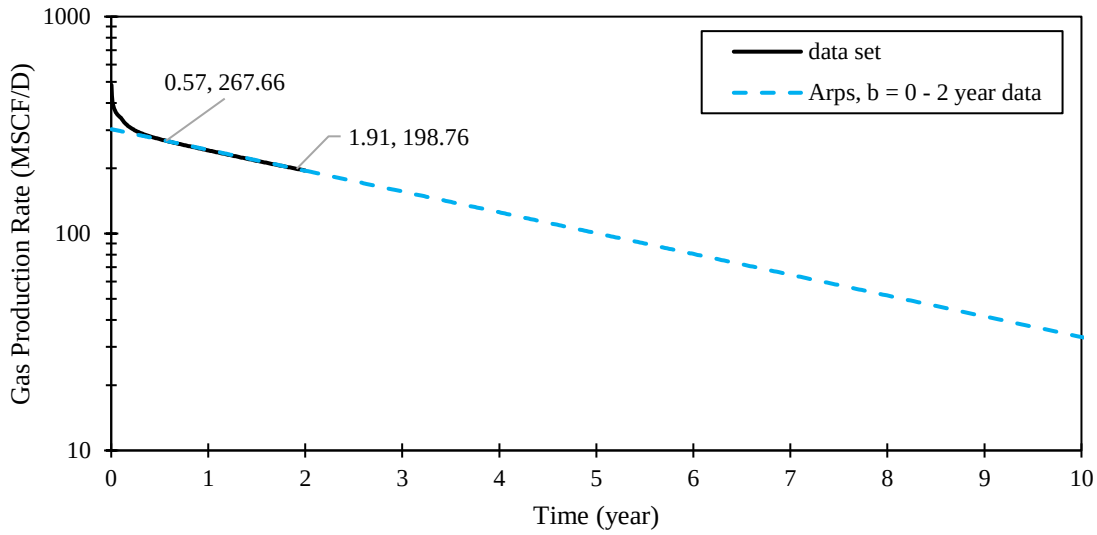

Figure 72 – Semi-log plot of gas rate versus time. The Arps decline curve is matched to the 2-year production data with b = 0.

The initial rate (q_i) for the Arps decline curve is obtained by extrapolating the semi-log straight line back to t = 0. For this first example, I obtained a q_i of 303 MSCF/D. Using parameters (D_i and b), I determined a constant decline parameter (b) to produce the closest match to the production history data. This matching is done by minimizing the summation of least squares between the production rate data and the forecasted rate. The minimization is only done for data in the boundary-dominated flow regime. I used the built-in solver

function from Microsoft Excel to minimize the least-squares summation, which is calculated using Eq. 4.22 and Eq. 4.23.

$$S = \sum_{i=1}^{N} r_i^2 \tag{4.22}$$

$$r_i = q^{\text{Data}} - q_i^{\text{Forc}} \tag{4.23}$$

where

S = summation of least squares

r_i = residual or difference between data and prediction

q^{Data} = value obtained from data

q^{Forc} = value obtained from forecast (Arps)

N = number of comparison points

For this gas-rate production data, I found that using a b value of 0 fit the 2-year production data best. This indicates an exponential decline for the gas production, which appeared to be too conservative, as proven in the forecasts using 6- and 10-year data. This illustrates the disadvantage of using an empirical-based forecasting method.

Next, I created a forecast gas production with 6 years of production history (Figure 73). Note that the initial decline rate (D_i) and initial production rate (q_i) remained the same as found earlier. I simply conducted the least-squares minimization using 6 years of production data to find the best b parameter. Similar to the previous case, this was done by using the solver function. For comparison, I also graphed the forecast results from using just the 2-year production history, which underestimates the production significantly. Figure 74 shows that having more production data available improves the forecast using the Arps decline equation. The summary of Arps parameters used in this first example for gas forecasting is tabulated in Table 25.

Table 25 – Arps decline curve constants used to forecast the gas production from the created data set (p_{wf} = 2,000psi). The parameters were chosen to best match the production from the data available (2, 6, and 10 years).

Gas Production History Data	q_i (MSCF/D)	D_i	b
Arps 2-year	303	22%	0.00
Arps 6-year	303	22%	0.36
Arps 10-year	303	22%	0.47

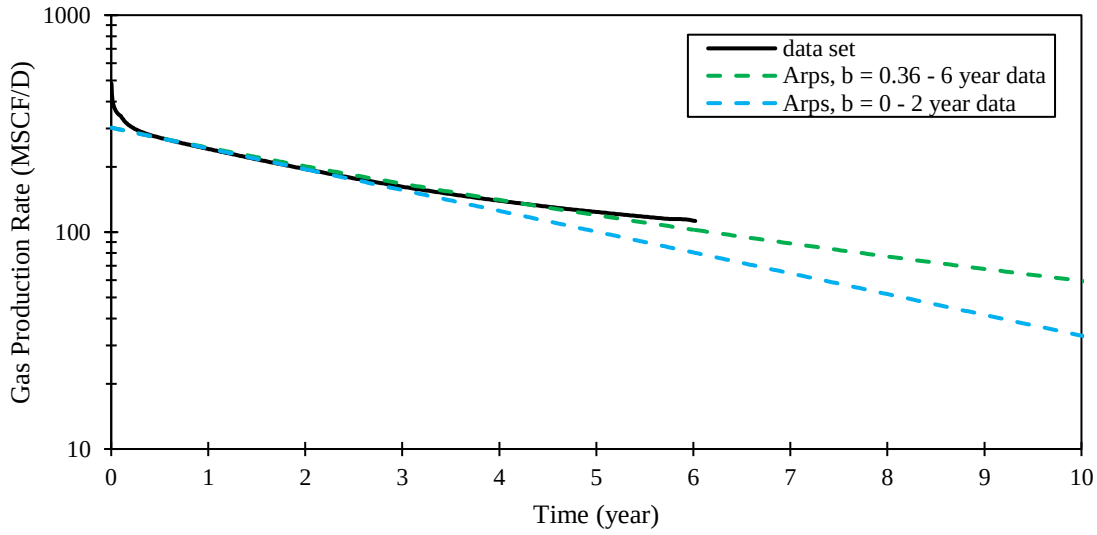

Figure 73 – Semi-log plot of gas rate versus time. The Arps decline curve is matched to the 6-year production data with a b = 0.36. Here, the deviations from the earlier forecast are apparent.

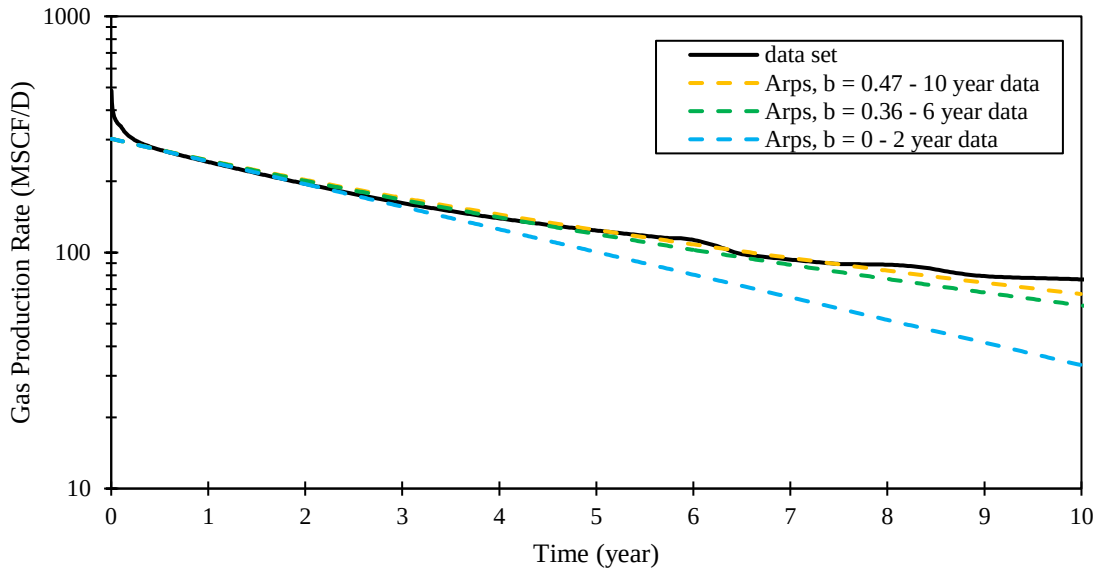

Figure 74 – Semi-log plot of gas rate versus time. The Arps decline curve is matched to the 10-year production data with a *b* = 0.47. The forecast using Arps is improved with time.

Using the Arps decline curve, I forecast the gas production for 30 years. I also created production forecasts using the mechanistic model, by inputting the reservoir and fluid properties into the model and using a constant bottomhole flowing pressure of 2,000 psi for the well constraint. The gas production rate forecasts and the production data set are compared in Figure 75 and the cumulative production are compared in Figure 76.

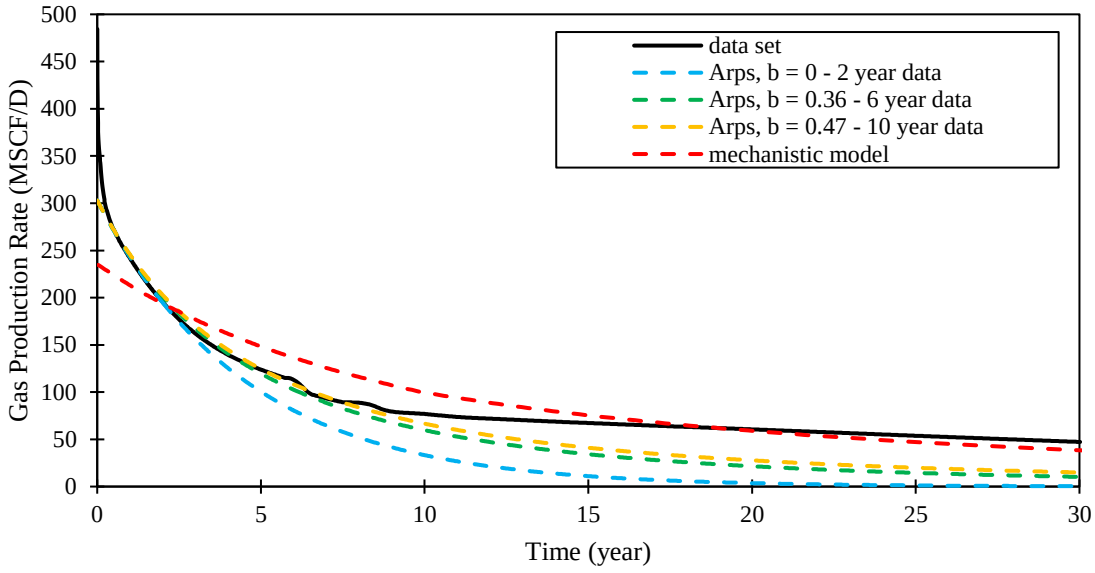

Figure 75 – Gas production rate matching and forecasting using Arps decline curve and the mechanistic model (p_{wf} = 2,000 psi).

To compare the deviation between the forecasts and the data set, I calculated the average absolute error of the production rate forecasts using Eq. 4.15 and Eq. 4.16. To compare the cumulative gas production, I used Eq. 4.15 at 10 years, 20 years, and 30 years. The comparisons are tabulated in Table 26.

$$e_i = \frac{\chi_i^{\text{Data}} - \chi_i^{\text{Forc}}}{\chi_i^{\text{Data}}} \tag{4.15}$$

$$E = \sum_{i=1}^{N} |e_i| \cdot \frac{1}{N} \times 100\% \tag{4.16}$$

where

χ^{Data} = value ($q_{g,o}$, G_p, N_p) from data set

χ^{Forc} = value ($q_{g,o}$, G_p, N_p) from forecast (Arps or mechanistic model)

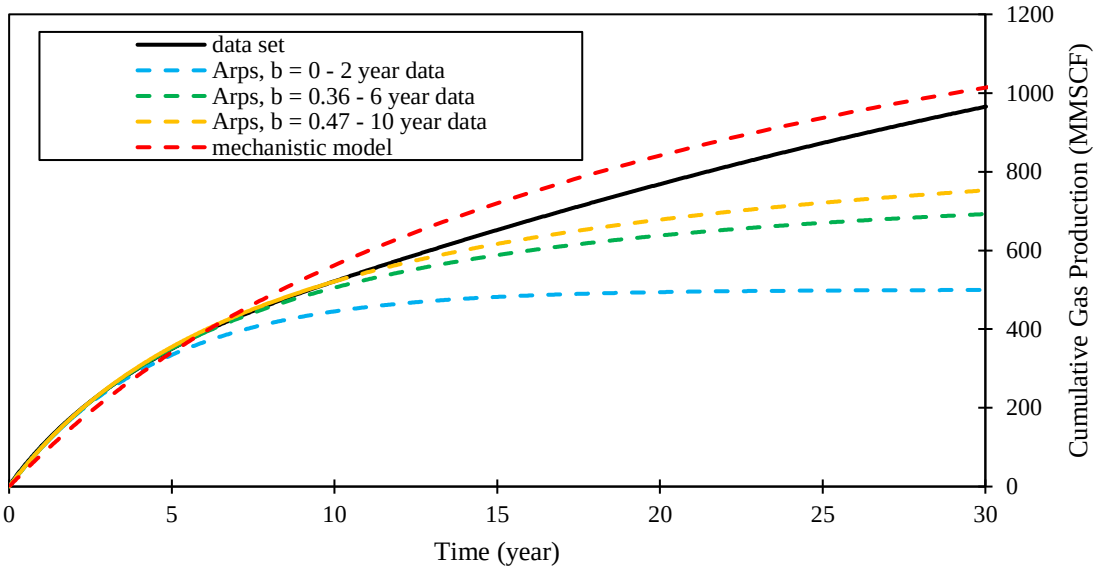

Figure 76 – Gas cumulative production forecasting using Arps decline curve and the mechanistic model (p_{wf} = 2,000 psi).

Table 26 – Average absolute error $[E(q_g)]$ of the forecasting method for gas production under constant bottomhole pressure constraint of 2,000 psi. The comparison $[e(G_p)]$ of cumulative production (10, 20 and 30 years) between the forecasts and the data set are also presented (negative value indicates overestimation, while positive value indicates underestimation).

Forecasting Method	$E(q_g)$	$e(G_p^{10})$	$e(G_p^{20})$	$e(G_p^{30})$
Mechanistic model	16.6%	-7.7%	-9.2%	-4.7%
Arps 2-year	37.7%	14.6%	35.7%	48.2%
Arps 6-year	21.2%	3.1%	17.0%	28.2%
Arps 10-year	17.1%	0.1%	11.7%	22.0%

The error comparisons presented in Table 26 display the benefit of using the mechanistic model for production forecasting. The mechanistic model takes into account the material balance of the reservoir and the complex fluid behavior, thus creating better estimates for both production rate and cumulative production. We see that the average absolute error of the gas production rate $[E(q_g)]$ of the mechanistic model forecast is significantly less than the Arps forecast. The mechanistic model also performs better at estimating the

cumulative production from the simulated gas-condensate reservoir. The mechanistic model prediction of cumulative gas production overall performs better than the Arps forecasts.

And the mechanistic model prediction for cumulative gas production gets better with time. At the end of 30 years, the cumulative gas prediction from the mechanistic model overestimates by 4.7%, while the Arps forecasts underestimates the cumulative production by 22%. This is significant in demonstrating the capability of the mechanistic model in creating accurate production forecasts for gas-condensate reservoirs.

The Arps equation can be used for both oil and gas forecasting. Here, I used the same method in forecasting oil production as in forecasting gas production. The Arps parameters used to create the decline curves are tabulated in Table 27, and the oil production forecasting is compared in Figure 77 and Figure 78. Once again, I compared the deviations between the oil production rate predictions and the data set using the average absolute error defined in Eq. 4.24 and Eq. 4.25. The differences in predicted oil cumulative production at 10, 20 and 30 years are also presented in Table 28.

Table 27 – Arps decline curve constants used to forecast oil production from the created data set (p_{wf} = 2,000 psi). The b parameters are empirically matched to the production data available (2, 6, and 10 years).

Oil Production History Data	q_i (STB/D)	D_i	b
Arps 2-year	43	22%	0.00
Arps 6-year	43	22%	0.28
Arps 10-year	43	22%	0.35

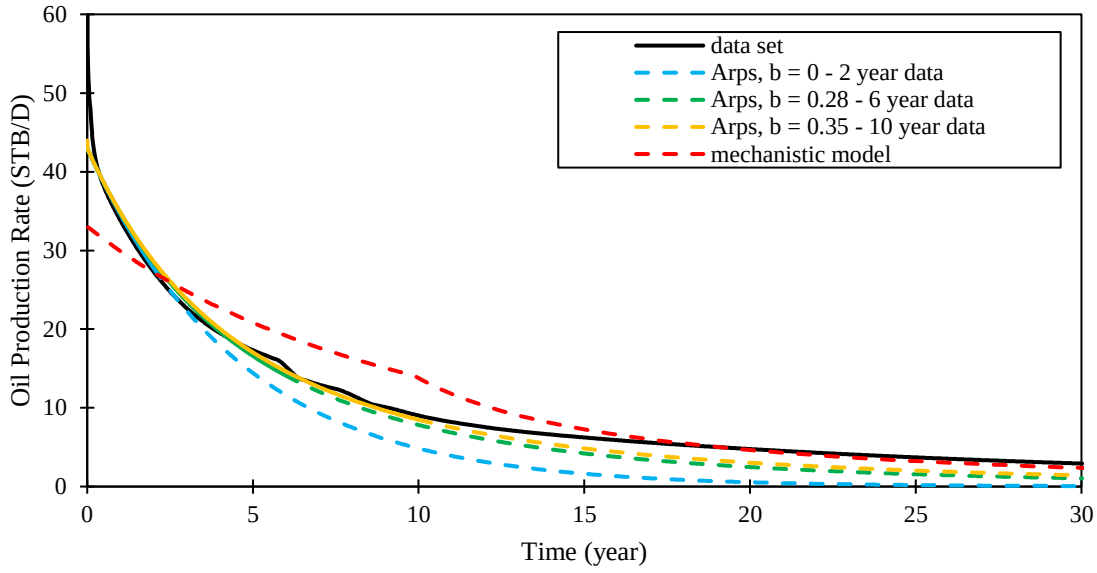

Figure 77 – Oil production rate matching and forecasting using Arps decline curve and the mechanistic model (p_{wf} = 2,000 psi). The forecasting results are compared to the data set acquired from commercial reservoir simulation.

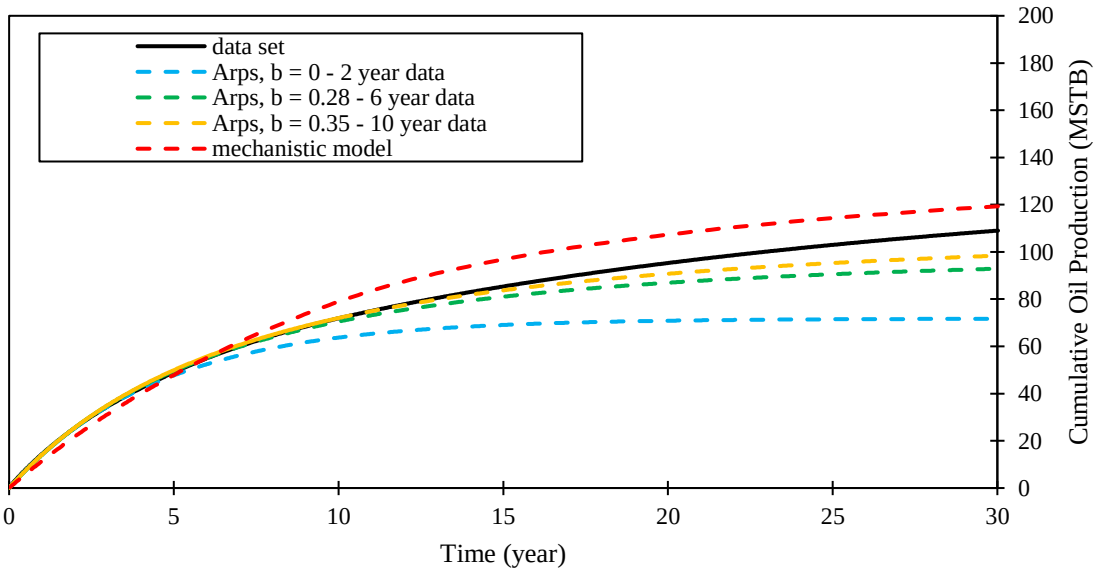

Figure 78 – Oil cumulative production forecasting using Arps decline curve and the mechanistic model (p_{wf} = 2,000 psi). The forecasting results are compared to the data set acquired from simulation in a commercial reservoir simulation.

Table 28 – Average absolute error [$E(q_o)$] of the forecasting method for oil production at constant bottomhole pressure of 2,000 psi. The comparison [$e(N_p)$] of cumulative production (10, 20 and 30 years) between the forecasts and the data set are also presented (negative value indicates overestimation, while positive value indicates underestimation).

Forecasting Method	$E(q_o)$	$e(N_p^{10})$	$e(N_p^{20})$	$e(N_p^{30})$
Mechanistic model	19.7%	-9.7%	-12.4%	-9.3%
Arps 2-year	34.1%	11.4%	25.6%	34.2%
Arps 6-year	16.3%	1.9%	8.8%	14.8%
Arps 10-year	11.9%	-0.2%	4.8%	9.7%

For the oil-production forecasting in a 30-year period, the mechanistic model performed better than the Arps decline curve. Similar to the gas production forecast, the cumulative oil production forecast improves as time progresses. The mechanistic model overestimates the oil cumulative production by 9.3%, while the Arps equation (with 10-year data) underestimates the value by 9.7%. The forecast of oil production rate from the mechanistic model is also better than the Arps prediction using 2-year data. However, the Arps decline curve is more successful at creating the rate decline forecasts. As expected, the Arps decline model performs better when more production history is available to be matched.

This example illustrates the advantage of using the mechanistic model for predictions. Since the mechanistic model takes into account the reservoir size and fluid properties, it is able to produce a more reliable forecast, especially in fluid cumulative production. Also, the advantage of the mechanistic model is that it does not need production data to be matched, thus eliminating the need to accumulate data to obtain a better forecast. Furthermore, it reveals the disadvantages in using empirically-based decline curves when predicting gas-condensate reservoirs. The first disadvantage is the need to create two production forecasts, for oil and for gas, whereas the mechanistic model takes into account the two-phase production in the forecasting. The second disadvantage is that the match is not always reliable in forecasting production, especially cumulative production. In this

example, the Arps model significantly underestimates the cumulative production for oil and gas.

Forecasting Example 2: Constant Bottomhole Flowing Pressure 3,800 psi

In the second example, the well produces from the same gas-condensate reservoir detailed in the first example but with production maintained above the dewpoint pressure (3,650 psi) by setting a bottomhole flowing pressure constraint of 3,800 psi on the wellbore. The reservoir and fluid properties are listed in Table 19 and Table 10. As in the first example, the performance of the mechanistic model was compared with the Arps empirical model to predict production for a 30-year period. The Arps model was forecasted knowing 2, 6, and 10 years of production history data. The method to create the production forecast using Arps was the same as presented previously in the first example.

The Arps decline curve parameters used to create the gas production forecasts are detailed in Table 29. The predictions from the mechanistic model and the Arps model are presented in Figure 79 and Figure 80, for gas rate and gas cumulative production, respectively. The deviations between the forecasting models and the production data set are presented in Table 30.

Table 29 – Arps decline curve constants used to forecast the gas production from the created data set (p_{wf} = 3,800psi). The parameters were chosen to best match the production from the data available (2, 6, and 10 years).

Gas Production History Data	q_i (MSCF/D)	D_i	b
Arps 2-year	139	12%	0.00
Arps 6-year	139	12%	0.14
Arps 10-year	139	12%	0.16

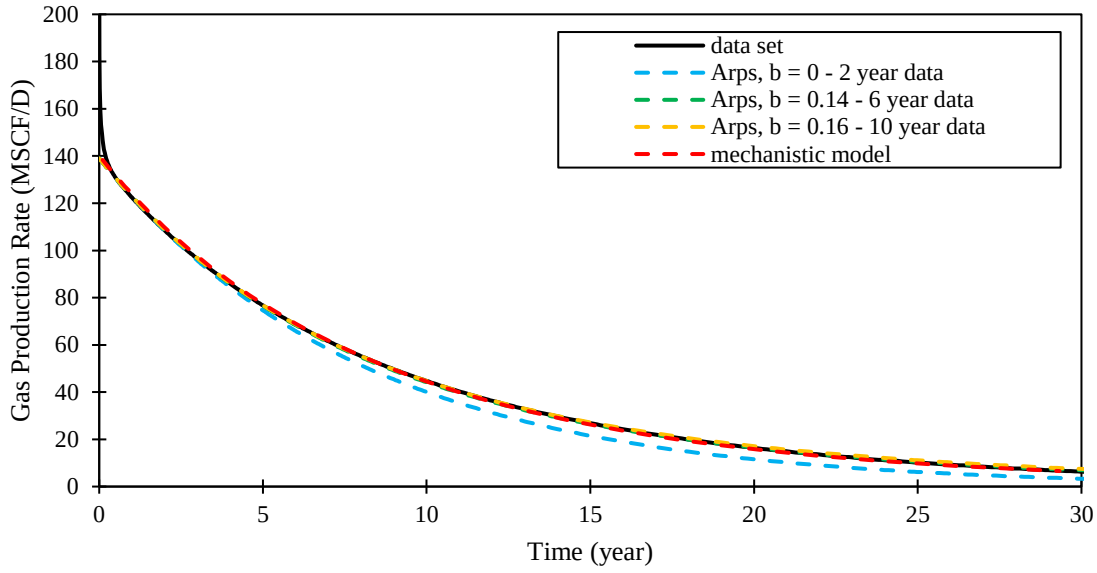

Figure 79 – Gas production rate matching and forecasting using Arps decline curve and the mechanistic model (p_{wf} = 3,800 psi). The forecasting results are compared to the data set acquired from the commercial reservoir simulator.

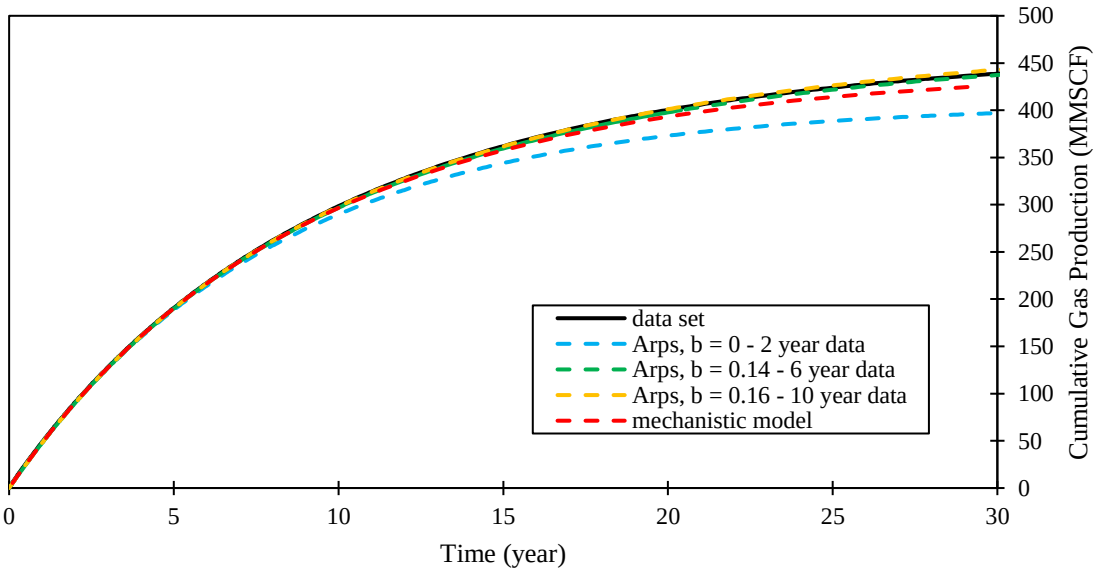

Figure 80 – Gas cumulative production forecasting using Arps decline curve and the mechanistic model (p_{wf} = 3,800 psi). The forecasting results are compared to the data set acquired from commercial reservoir simulation.

Table 30 – Average absolute error [$E(q_g)$] of the forecasting method for gas production under constant bottomhole pressure constraint of 3,800 psi. The comparison [$e(G_p)$] of cumulative production (10, 20 and 30 years) between the forecasts and the data set are also presented (negative value indicates overestimation, while positive value indicates underestimation).

Forecasting Method	$E(q_g)$	$e(G_p^{10})$	$e(G_p^{20})$	$e(G_p^{30})$
Mechanistic model	1.4%	0.9%	3.1%	3.1%
Arps 2-year	8.2%	2.9%	6.8%	9.5%
Arps 6-year	0.9%	0.5%	0.7%	0.3%
Arps 10-year	1.2%	0.2%	-0.2%	-1.0%

Similarly, the oil production rate was forecasted using the two methods. The Arps decline parameters for oil production prediction are tabulated in Table 31. The forecasting of oil production rate and cumulative production are presented in Figure 81 and Figure 82. The comparison of errors is presented in Table 32.

Table 31 – Arps decline curve constants used to forecast the oil production from the created data set (p_{wf} = 3,800 psi). The b parameters are empirically matched to the production data available (2, 6, and 10 years).

Oil Production History Data	q_i (STB/D)	D_i	b
Arps 2-year	19.4	12%	0.00
Arps 6-year	19.4	12%	0.18
Arps 10-year	19.4	12%	0.18

Table 32 – Average absolute error [$E(q_o)$] of the forecasting method for oil production under constant bottomhole pressure constraint of 3,800 psi. The comparison [$e(N_p)$] of cumulative production (10, 20 and 30 years) between the forecasts and the data set are also presented (negative value indicates overestimation, while positive value indicates underestimation).

Forecasting Method	$E(q_o)$	$e(N_p^{10})$	$e(N_p^{20})$	$e(N_p^{30})$
Mechanistic model	1.5%	0.7%	2.9%	2.9%
Arps 2-year	8.7%	3.3%	7.3%	10.0%
Arps 6-year	1.8%	0.3%	-0.5%	-1.7%
Arps 10-year	1.8%	0.3%	-0.5%	-1.7%

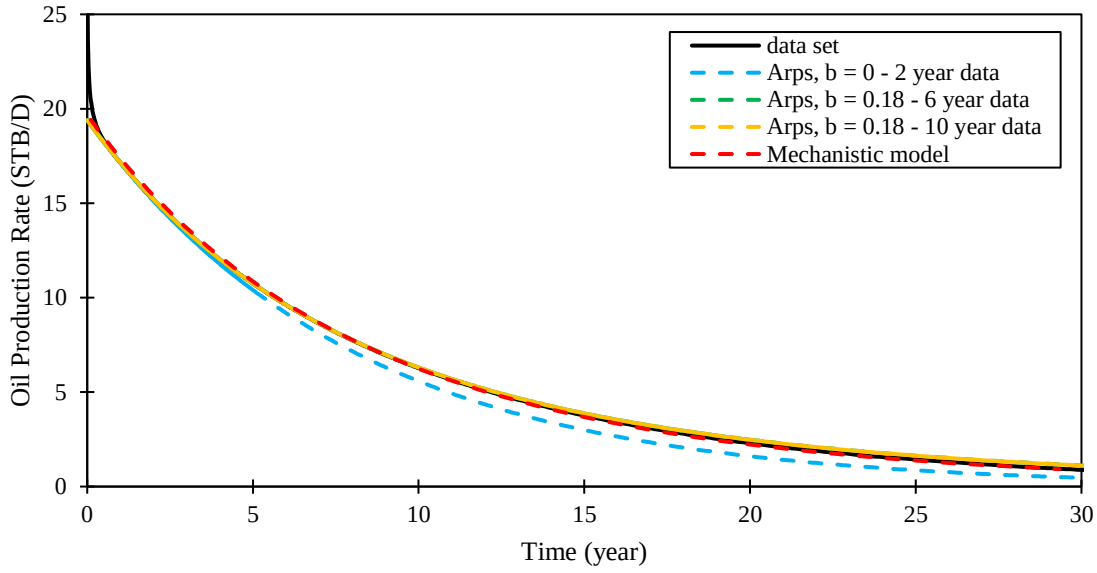

Figure 81 – Oil production rate matching and forecasting using Arps decline curve and the mechanistic model (p_{wf} = 3,800 psi). The forecasting results are compared to the data set acquired from commercial reservoir simulation.

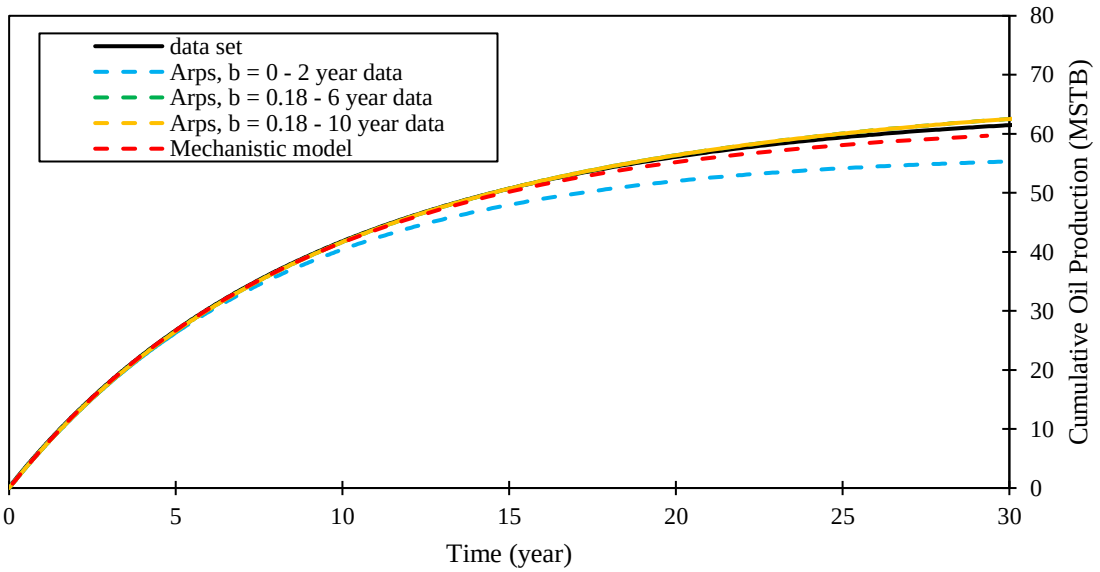

Figure 82 – Oil cumulative production forecasting using Arps decline curve and the mechanistic model (p_{wf} = 3,800 psi). The forecasting results are compared to the data set acquired from simulation in a commercial reservoir simulator.

In this second forecasting example, I maintained the production above the dewpoint pressure. The mechanistic model achieved excellent agreement with the data set. The average absolute error of the oil and gas production rate forecast are within 1.5% of the data set in the 30-year period. The excellent agreements between the mechanistic model and the data set are also seen in the cumulative production comparison. The cumulative production prediction from the mechanistic model are around 3% error, for both oil and gas.

Also, in this example, the Arps model performs better than in the first example. The reason for this improved performance is that the reservoir pressure was maintained above dewpoint pressure; thus, the fluid stays in a single phase in the reservoir. When there is no significant change to the reservoir, such as in this example, the Arps forecasting method is able to produce accurate results. However, as in the case in the first example, where pressure fell below the dewpoint, the Arps decline curve resulted in significant deviations from the data set. The advantage of the mechanistic model is that it takes into account the complex fluid behavior of gas-condensate reservoirs. As seen in the first example, the cumulative production forecasts from the mechanistic model produced a better agreement with the data set than the predictions by the Arps model.

CHAPTER V

CONDENSATE BANK SATURATION MODEL

In gas-condensate reservoirs, as reservoir pressure drops below the dewpoint, liquid accumulates in the reservoir. The liquid accumulation is most prevalent in the near-wellbore area, where the pressure is lowest in the reservoir. The increase in liquid saturation hinders the production of gas from the reservoir due to two-phase flow phenomena. Relative permeability curves are used to describe this effect in the flow equation. In the previous chapter, predictions from the mechanistic model deviated from the commercial simulator. This is due to the presence of condensate banking, which is simulated in the commercial simulator but ignored in the mechanistic model.

In this chapter, I attempted to add the condensate banking consideration into the developed mechanistic model through a two-tank approach. The two tanks represent the reservoir (big tank) and the condensate banking region (small tank). The big tank is the CVD-based mechanistic model described in previous chapters. The small tank, which is based on a CVD simulation modified with a replenishment concept introduced in this chapter, is solely used to estimate the liquid saturation buildup in the near-wellbore area, without altering the material balance of the system. The estimated liquid saturation from the small tank is used to determine the relative permeability value, which is later used in the flow equations of the mechanistic model.

5.1 Condensate Bank Modeling (Small-Tank Approach)

Condensate banking occurs in gas-condensate reservoirs as the pressure falls below the saturation pressure. Condensate (liquid) accumulates in the reservoir, hindering the flow of gas from the reservoir to the production well (Figure 3). The liquid buildup must be taken into account to properly model production from the gas-condensate reservoir. I

designed three replenishment methods to estimate condensate buildup in the near-wellbore region with the CVD-based mechanistic forecasting model.

In this two-tank approach, the big tank, which represents the reservoir is the mechanistic model detailed in previous chapters. The small tank, which represents the condensate-banking region, is used to estimate the liquid saturation buildup. The small tank is based on a CVD test modified to include production alterations and the concept of fluid replenishment (Figure 83).

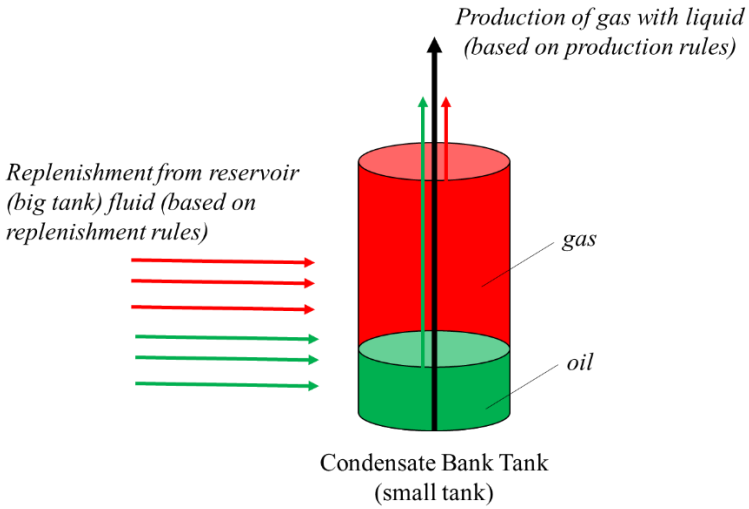

Figure 83 – Conceptual condensate bank modeling through modified CVD. The modified CVD takes into account total or partial replenishment using reservoir fluid composition that allows for liquid buildup.

The small tank allows for the production of gas and oil according to specified production rules. The production rules are based on the saturation of the small tank. The replenishment concept represents the flow of reservoir fluid into the near-wellbore region, which alters the near-wellbore fluid composition. This fluid mixing between the reservoir and the condensate bank region is modeled in the small tank by a composition-alteration equation. A user-defined mixing fraction (A) controls the amount of reservoir fluid

contribution into the small tank. The replenishment alters the composition of the small tank fluid and allows the heavier hydrocarbon component to accumulate, thus contributing to liquid buildup.

In all three methods to estimate the condensate bank liquid saturation, the saturation information from the condensate bank modeling is used to look up relative permeability (k_{r_g}) values to be used in the radial pseudosteady-state flow equation (Eq. 5.1). The mechanistic model forecasts, adjusted by the condensate bank consideration, are compared with those from the commercial simulator.

$$q_g = \frac{kk_{rg}h\left(m(\bar{p}) - m(p_{wf})\right)}{1424T\left(\ln\left(\frac{r_e}{r_w}\right) + s\right)} \tag{5.1}$$

5.2 Development of the Condensate Bank Saturation Profile

The condensate bank is modeled by a small tank of a user-specified size and charged initially with the initial reservoir fluid composition. The model is based on the constant volume depletion (CVD) test with an altered fluid production and replenishment scheme. The goal of the modifications is to mimic the restriction of fluid flow because of increased fluid saturation in the condensate bank region. This is done through altering the composition of the small tank CVD so that liquid saturation can increase in it. The three methods to predict near-wellbore liquid saturation do not change the material balance of the mechanistic model but only estimates liquid saturation buildup, thus providing a relative permeability value for the flow equation (Eq. 5.1).

The objective of the first and second methods is to create a liquid saturation as a function of pressure (saturation/pressure profile). Using the saturation/pressure profile, we look up the relative permeability value based on the bottomhole flowing pressure (p_{wf}) of the well.

The third method was developed from the production and replenishment schemes proposed in Method 2 (Chapter 5.2.2) and is further elaborated in Chapter 5.2.3. It offers a condensate-saturation estimation using a method of coupling small-tank and big-tank simulations. The coupling is done by comparing the moles produced from the small tank with those from the big tank and checking for the equal mole production from the small and big tanks.

The synthetic reservoir in Case 1, presented in Chapter 4, was used as the example case to compare the mechanistic forecasts considering condensate bank modeling. To recall, the reservoir properties and operating constraints are listed in Table 19 and Table 20, respectively, while the fluid is taken from the Eagle Ford gas-condensate region, detailed in Table 10. The relative permeability curves are presented in Figure 39. The comparisons between the commercial simulator and the mechanistic model considering condensate banking are presented in the Results section of each method.

5.2.1 Saturation Profile 1 - y^* Method

For the first method, I created a saturation/pressure profile to represent the condensate bank liquid saturation at different bottomhole flowing pressures. Similar to the conventional CVD, the volume produced at every pressure decrement is determined by subtracting the expanded volume by the reference (initial) volume of the small tank (Eq. 5.2).

$$V_{\mathrm{s,prod}}^{j} = V_{\mathrm{s}}^{j} - V_{\mathrm{s,ref}} \tag{5.2}$$

where

$V_{\mathrm{s,prod}}^{j}$ = small tank volume to be produced at pressure decrement j

V_{s}^{j} = total volume in small tank at pressure decrement j

$V_{\mathrm{s,ref}}$ = reference (initial) volume of small tank

The produced volume is divided between the fluids (oil and gas) based on the saturation of the expanded small tank (Eq. 5.3 and Eq. 5.4). The saturation of liquid and gas is defined in Eq. 5.5 and Eq. 5.6. For convenience, the subscript s is omitted in the equations below, although the equations still refer to the small-tank properties.

$$V_{\mathrm{prod}_g}^{j} = V_{\mathrm{prod}}^{j} S_g \tag{5.3}$$

$$V_{\mathrm{prod}_o}^{j} = V_{\mathrm{prod}}^{j} S_o \tag{5.4}$$

$$S_g = \frac{V_g^j}{V^j} = \frac{f_g n V_{m_g}}{n\left(f_g V_{m_g} + f_o V_{m_o}\right)} \tag{5.5}$$

$$S_o = \frac{V_l^j}{V^j} = \frac{f_o n V_{m_o}}{n\left(f_g V_{m_g} + f_o V_{m_o}\right)} \tag{5.6}$$

where

$V_{\mathrm{prod}_g}^{j}$ = small tank volume to be produced at pressure decrement j from phase g

$S_{g,l}$ = gas or liquid saturation of expanded small tank (fraction)

V_m = molar volume

$f_{g,o}$ = molar fraction of gas (g) or oil/liquid (o)

n = total moles currently in small tank

Once the production rules have been implemented, the small tank continues similarly to the CVD algorithm described in Chapter 3. The volumes of gas and liquid to be produced are determined, and the moles of the produced phases are calculated. This is done by dividing the volume of gas and liquid by the molar volumes of gas (Eq. 5.7) and liquid (Eq. 5.8), respectively.

$$n_{\mathrm{prod}_g} = \frac{V_{\mathrm{prod}_g}}{V_{m_g}} \tag{5.7}$$

$$n_{\mathrm{prod}_o} = \frac{V_{\mathrm{prod}_o}}{V_{m_o}} \tag{5.8}$$

Next, the remaining moles are determined through subtraction of the moles produced from the moles in the condensate-bank tank. Thus, the number of moles remaining (n_{rem}) after production in the condensate-bank tank are described in Eq. 5.9, Eq. 5.10, and Eq. 5.11.

$$n_{\mathrm{rem}_g} = n_g - n_{\mathrm{prod}_g} \tag{5.9}$$

$$n_{\mathrm{rem}_o} = n_o - n_{\mathrm{prod}_o} \tag{5.10}$$

$$n_{\mathrm{rem}} = n_{\mathrm{rem}_g} + n_{\mathrm{rem}_l} \tag{5.11}$$

The new molar fractions of liquid (f_o) and gas (f_g) are calculated using Eq. 5.12 and Eq. 5.13. The new molar fractions are used in the replenishment scheme.

$$f_o = \frac{n_{\mathrm{rem}_o}}{n_{\mathrm{rem}}} \tag{5.12}$$

$$f_g = 1 - f_o \tag{5.13}$$

To model the incoming fluid from the reservoir into the condensate-bank region, I implemented the concept of replenishment. In this first method, the replenishment is done by altering the composition of the gas phase (y_i) in the small tank with the overall reservoir composition (z_i). The contribution of the overall reservoir composition is controlled by the mixing constant (A). The new composition of the gas is termed y^* and is described in Eq. 5.14. This first method is interchangeably referred to as the y^* method.

$$y_i^* = z_i^{\mathrm{RES}}(A) + y_i^{\mathrm{SML}}(1 - A) \tag{5.14}$$

$$z_i^{\mathrm{SML}} = f_g y_i^* + (1 - f_g) x_i^{\mathrm{SML}} \tag{5.15}$$

where

y_i^* = new gas composition of component *i*

z_i^{RES} = overall fluid composition of big tank (RES) or small tank (SML)

A = user-defined fraction, $0 < A < 1$

y_i^{SML} = gas composition of the small tank

The user-defined mixing constant A controls the contribution of the reservoir fluid composition into the small tank. As the value of A approaches 1, the gas composition in the small tank is completely changed to be the overall composition of the reservoir fluid or full replenishment. If A is set to a value of zero, this means that there is no contribution from the reservoir fluid and the replenishment concept is ignored. Typically, from this study, I found that using a small mixing constant value, around $A = 0.1$, produces the best calibration results. A higher mixing constant leads to underestimation of fluid production forecasts due to overestimation of near-wellbore liquid saturation.

In this first method, the higher the mixing constant (A) selected, the heavier the small-tank overall fluid composition becomes with every pressure stage, resulting in higher liquid saturation buildup. The reason for this is that the small tank gas composition (y_i^{SML}) is altered with contribution from a heavier overall reservoir fluid composition (z_i^{RES}). The liquid (oil) composition (x_i^{SML}) remains the same in the small tank. The liquid and gas compositions are recombined to obtain the overall small tank composition (z_i^{SML}). The recombination is described in Eq. 5.15. The CVD simulation continues using the new recombined composition (z_i^{SML}). A flowchart of this first method is presented in Figure 84.

Results

The size and porosity of the condensate bank tank are described in Table 33. The radius of the small tank is chosen to be the same size as the first radial grid modeled in the commercial simulator. The height and porosity of the condensate bank are the same as in the created synthetic reservoir.

Table 33 – Small tank properties to model the near-wellbore saturation.

Radius	16 ft
Height	20 ft
Porosity	0.2

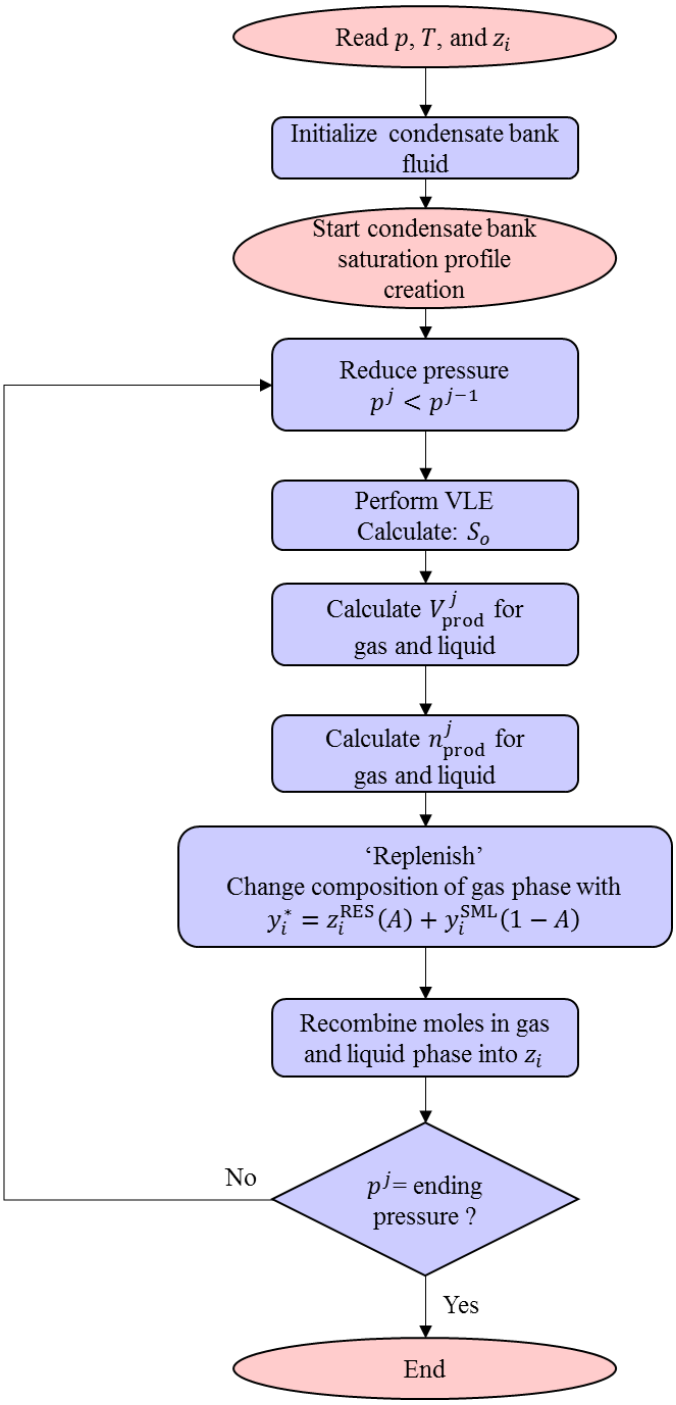

Figure 84 – Flowchart for condensate bank saturation profile creation using the y^* method. In this method, the production from each existing phase is based on the saturation of the small tank. The replenishment only alters the gas composition (Eq. 5.14), while keeping the liquid composition the same.

Using the y^* method, the replenishment scheme successfully created a near-wellbore saturation with closer resemblance to the commercial simulator prediction (Figure 85). The profile of liquid saturation versus pressure appears as Figure 86. The mixing constants selected (0.05, 0.1, and 0.2) provide the closest resemblance to the saturation profile from the commercial model.

The saturation profile created from this model was used to determine the relative permeability (k_r) used in the flow equation (Eq. 5.1). From the calculated or specified bottomhole pressure in the production model, the algorithm looks up the liquid saturation from the saturation profile created in this method. Then, using the liquid saturation obtained, the relative permeability value is obtained from the curve provided in the simulation model.

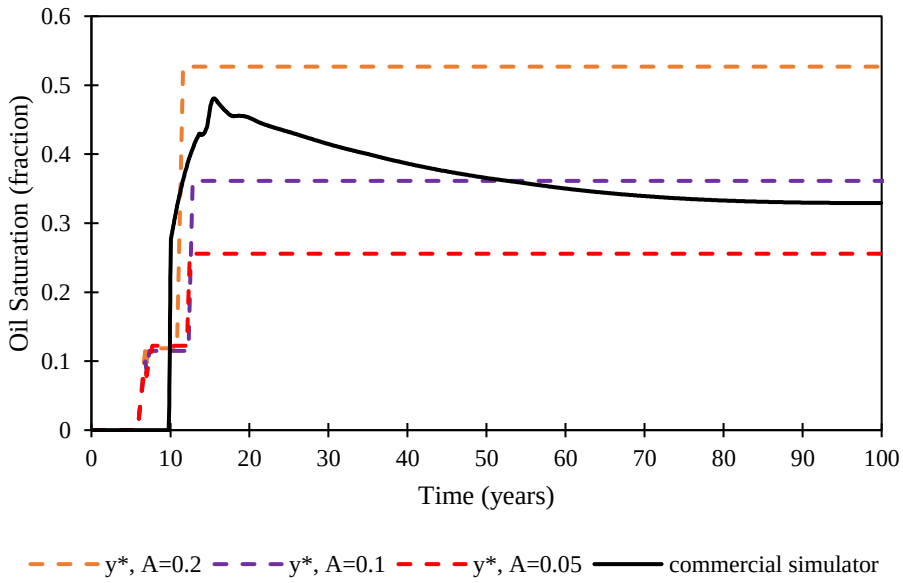

Figure 85 – Small tank liquid saturation versus time using the y^* method. The liquid saturation of the near-wellbore from the commercial simulator is taken from the nearest gridblock to the well.

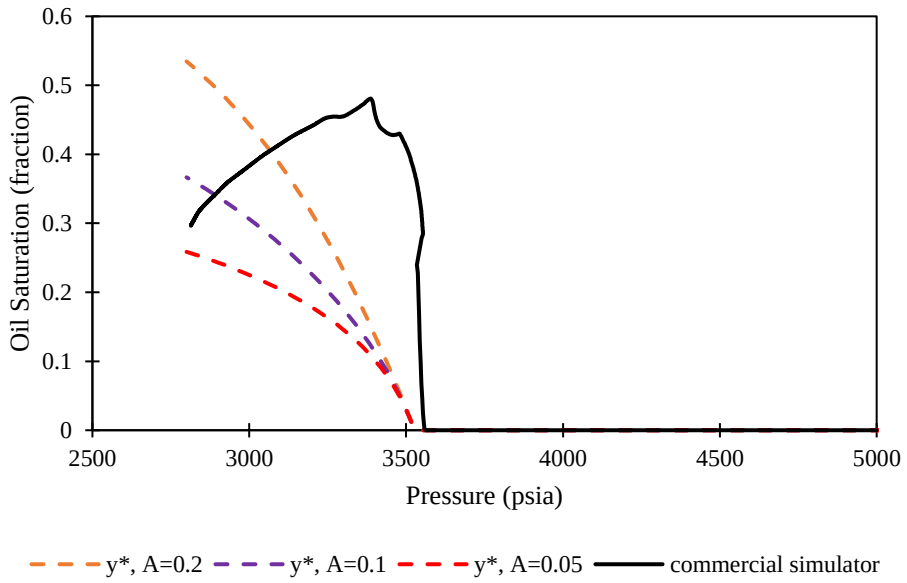

Figure 86 – Small tank liquid saturation versus pressure using the y^* method. The liquid saturation of the near-wellbore from the commercial simulator is taken from the nearest gridblock to the well.

Figure 87 presents the average reservoir pressure and bottomhole flowing pressure forecasts. The y^* method for condensate-bank saturation estimates improves the forecast from the mechanistic model. Mixing constants of 0.05 and 0.1 produced better forecasting predictions than a mixing constant of 0.2, which led to a large deviation from the commercial results.

The impact of the small-tank prediction on the forecasts can be explained by observing the liquid saturation profiles created using different A values (Figure 86); a higher A value in the condensate bank results in a larger liquid saturation prediction as pressure decreases. The higher saturation prediction relates to a lower gas relative permeability (k_{r_g}) value used in the flow equation. This decreases the calculated fluid production rate, thus increasing the time calculated for each pressure decrement step (Eq. 4.12). Physically, this represents the gas rate being restricted due to multiphase flow phenomena.

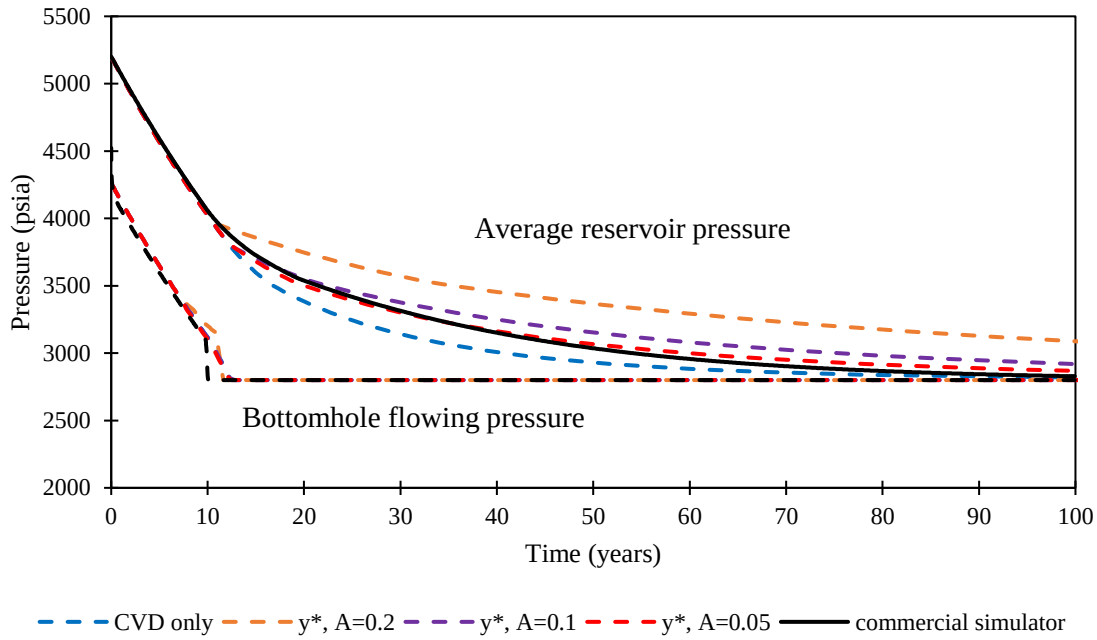

Figure 87 – Average reservoir pressure and bottomhole flowing pressure prediction using the y^* method for near-wellbore liquid saturation buildup.

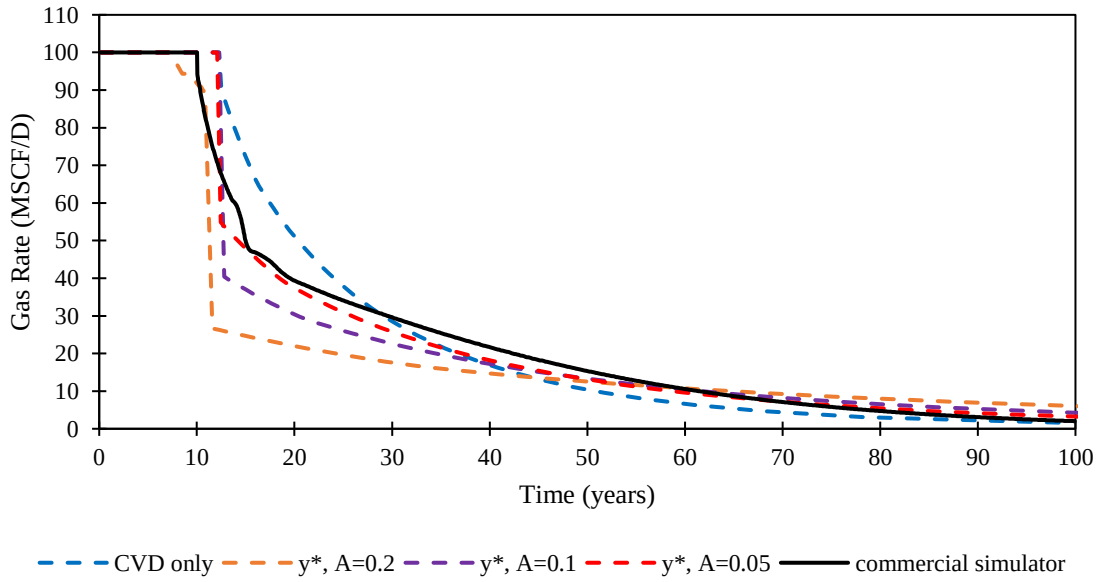

Figure 88 – Gas rate prediction using the y^* method for near-wellbore liquid saturation buildup.

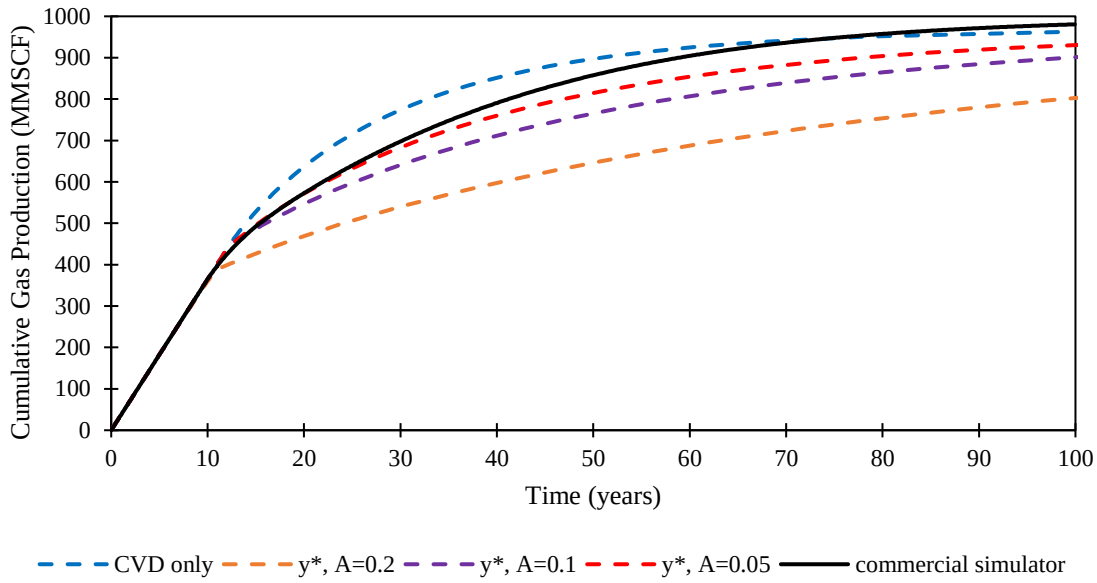

Figure 89 – Gas cumulative production forecasts using the y^* method for near-wellbore liquid saturation buildup.

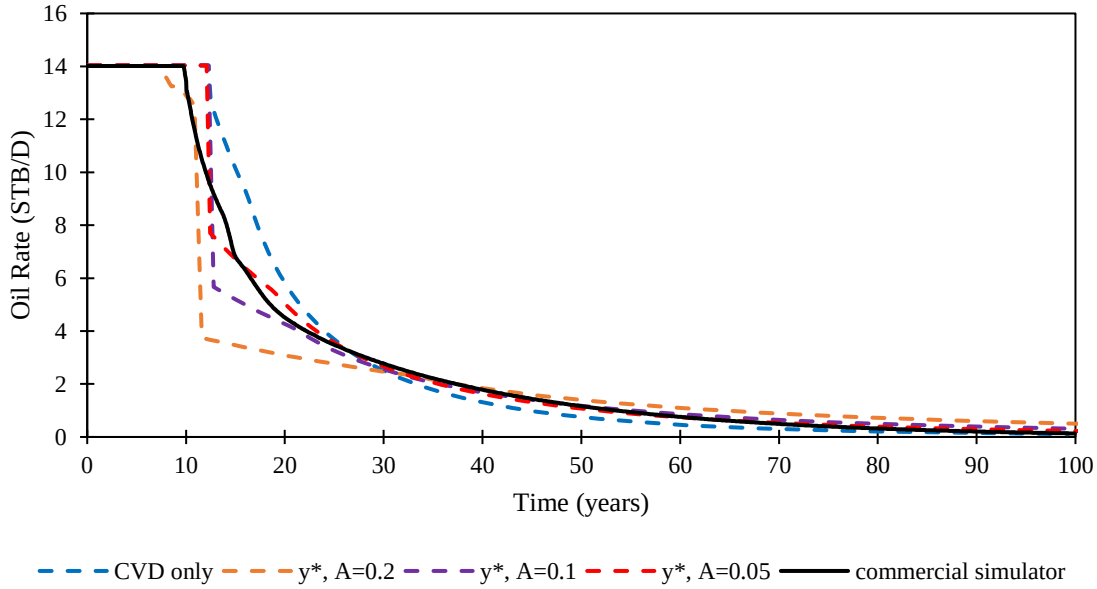

Figure 90 – Oil-rate prediction using the y^* method for near-wellbore liquid saturation buildup.

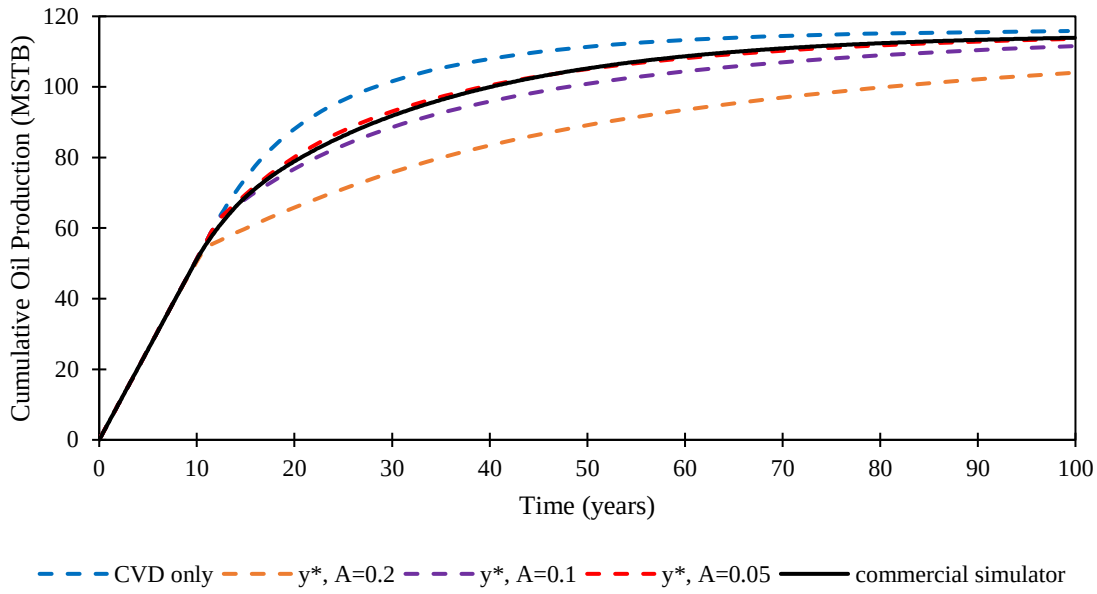

Figure 91 – Oil cumulative production forecasts using the y^* method for near-wellbore liquid saturation buildup.

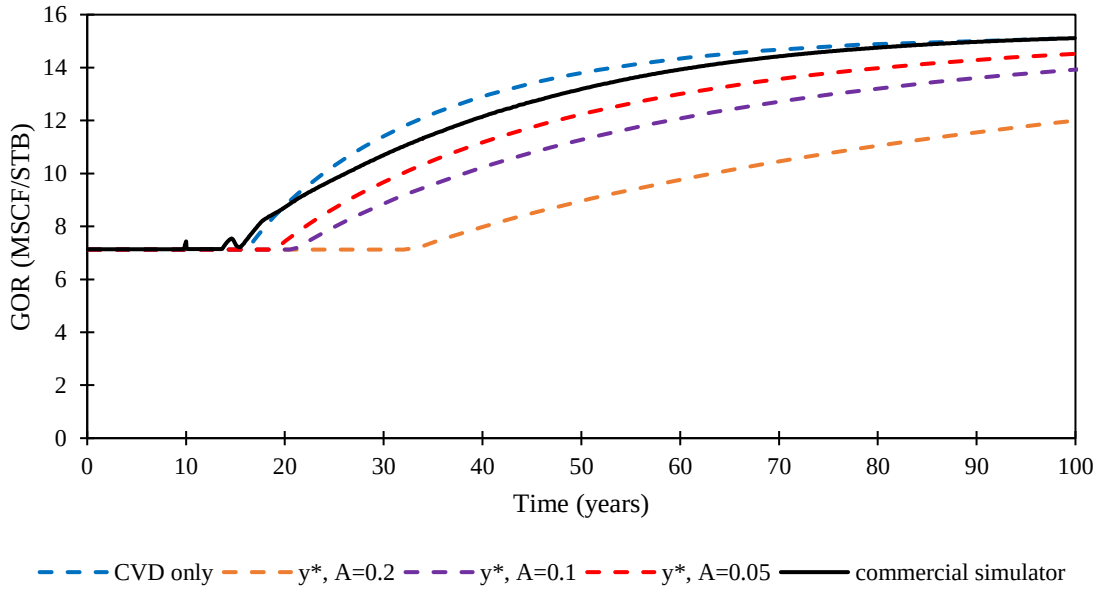

Figure 92 – Gas/oil ratio (GOR) forecasts using the y^* method for near-wellbore liquid saturation buildup.

Table 34 – Average absolute errors of mechanistic model (using y^* method) and commercial simulator predictions (Eq. 4.15). The highlighted row has the best agreement with the commercial simulator.

	P_{avg}	q_g	G_p	q_o	N_p	GOR
CVD only	2.00%	13.40%	3.90%	14.40%	4.10%	1.70%
y^*, A = 0.05	0.80%	6.80%	1.50%	5.90%	1.00%	3.30%
y^*, A = 0.1	1.20%	12.60%	3.30%	10.50%	1.80%	5.20%
y^*, A = 0.2	3.50%	19.50%	8.70%	21.20%	6.40%	9.90%

The summary of the average absolute error of the mechanistic model with and without condensate bank saturation modeling is presented in Table 34. Using the appropriate A value decreases the average error percentage between the mechanistic model and the commercial simulator results. However, Table 34 also shows that choosing an A value that is too high can cause higher error, such as the case of A = 0.2. From the comparison, we see that using a mixing value of 0.05 or 0.1 leads to a better error percentage than solely using the CVD. Observing this behavior, a lower mixing constant (A) when using the y^* method will achieve better forecasting results whereas a higher mixing constant will lead to overestimation of liquid saturation and large errors in the mechanistic forecasting.

5.2.2 Saturation Profile 2 - z^* Method

The *y** study suggested that improvements could be made in the liquid-saturation prediction to better the outcome of the mechanistic model results. One such improvement is in the immediate increase in saturation as pressure falls below the dewpoint (Figure 86). The second is in liquid saturation decreasing after reaching a peak saturation. I attempted to implement these improvements by altering the production rules of the condensate-bank modeling.

In the second method, I altered the production and replenishment rule to the small tank CVD on the basis of the relationship between production times (t). The derivation for the production rule begins with the relationship between volume produced, rate, and time as described in Eq. 5.16 and Eq. 5.17.

$$V_{\text{prod}_o} = q_o t \tag{5.16}$$

$$V_{\text{prod}_g} = q_g t \tag{5.17}$$

where

V_{prod} = volume produced of gas (g) or oil/liquid (o) phase

q = fluid rate production of gas (g) or oil/liquid (o)

t = production time

Setting the production time equal for Eq. 5.16 and 5.17 and rearranging gives Eq. 5.18, which describes the ratio between oil and gas production.

$$\frac{V_{\text{prod}_o}}{V_{\text{prod}_g}} = \frac{q_o}{q_g} \tag{5.18}$$

The ratio of liquid to gas rates can be approximated as in Eq. 5.19. The ratio between the rates reduces to the ratios of the viscosities of the fluids and the relative permeability of the fluids that are based on the saturation of the condensate-bank tank. To simplify the formula, we define the ratio of the volume produced with the term F as in Eq. 5.20.

$$\frac{V_{\text{prod}_o}}{V_{\text{prod}_g}} = \frac{q_o}{q_g} \cong \frac{\left(\frac{k_{r_o} A}{\mu_o}\right)\left(\frac{dp}{dr}\right)}{\left(\frac{k_{r_g} A}{\mu_g}\right)\left(\frac{dp}{dr}\right)} = \frac{k_{r_o}}{\mu_o}\frac{\mu_g}{k_{r_g}} \tag{5.19}$$

$$F = \frac{k_{r_o}}{\mu_o}\frac{\mu_g}{k_{r_g}} \tag{5.20}$$

where

k_r = relative permeability of gas (g) or oil (o) phase

A = reservoir area

μ = viscosity of gas (g) or oil (o) phase

$\frac{dp}{dr}$ = differential pressure with radius

F = ratio of oil volume to gas volume produced

Using the definition of total produced volume (Eq. 5.21) and Eq. 5.20, the relationship for volume of liquid produced is described in Eq. 5.22. Total volume produced at pressure step j is calculated using Eq. 5.2. Similarly, the relationship for volume of gas produced can be described as in Eq. 5.23.

$$V_{\text{prod}} = V_{\text{prod}_o} + V_{\text{prod}_g} \tag{5.21}$$

$$V_{\text{prod}_l} = \frac{FV_{\text{prod}}}{(F+1)} \tag{5.22}$$

$$V_{\text{prod}_g} = \frac{V_{\text{prod}}}{1+F} \tag{5.23}$$

After the volume to be produced from each phase has been calculated, the produced and remaining moles are calculated using Eq. 5.7 through Eq. 5.11, described in the previous section.

To model the flow of fluid from the reservoir into the condensate-bank region, the A value is defined as the ratio between the moles coming into the small tank and the remaining moles in the tank after production (Eq. 5.24).

$$A = \frac{n_{\text{into small tank}}}{n_{\text{remaining in small tank}}} \tag{5.24}$$

$$0 < A < 1$$

Thus, the user-defined mixing constant controls the addition of moles that enters the small tank. The total number of moles in the tank after replenishment is the summation of the number of moles remaining and the number of moles coming into the condensate-bank tank (Eq. 5.25). With a bigger mixing constant, more moles enter the small tank. This leads to a larger number of moles produced in the next pressure decrement step. Though

the number of moles produced is not tracked here, it is used in the third method to relate the small-tank production to the big tank production.

$$n_{\text{total}}^{\text{new}} = n_{\text{remaining in small tank}} + n_{\text{into small tank}} \tag{5.25}$$

In this second method, the replenishment rule alters the overall composition of the small tank. The alteration to the small tank composition is described in Eq. 5.26. Unlike the first method, where only the gas composition (y_i) is altered, here the overall composition (z_i) of the small tank is changed. The altered small tank overall composition is termed (z^*), so this method is called the z^* method.

$$z_i^* = Az_i^{\text{RES}} + (1 - A) \cdot [f_g^{\text{new}} y_i^{\text{SML}} + \left(1 - f_g^{\text{new}}\right) x_i^{\text{SML}}] \tag{5.26}$$

In this method, a higher mixing constant A corresponds to higher contribution from the big tank (reservoir) into the small tank. The altered overall composition is used for the next pressure decrement step to continue the small-tank CVD. The flowchart for the z^* method is presented in Figure 93.

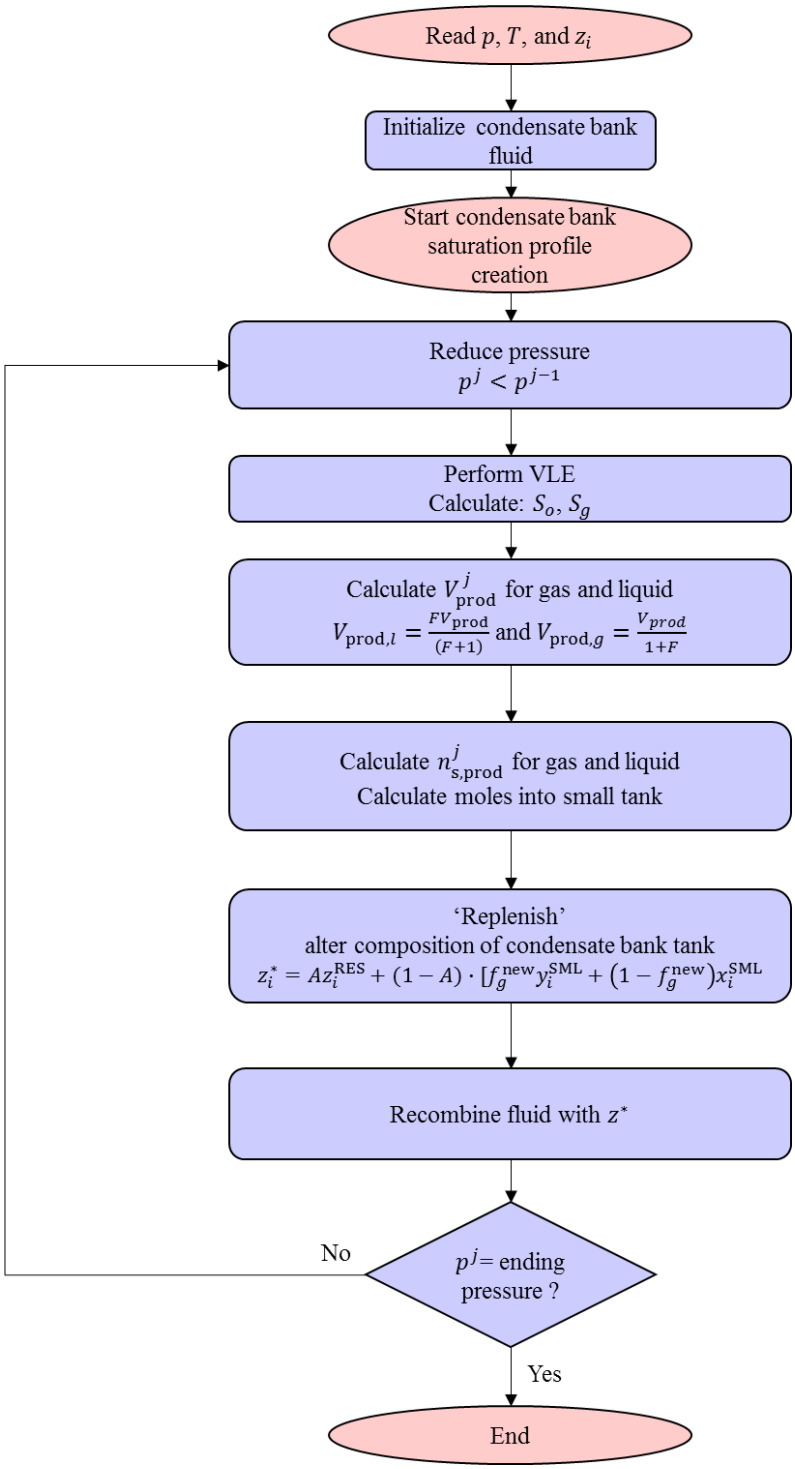

Figure 93 – Flowchart for condensate bank saturation profile creation using the z^* method. In this method, the production rule is based on the volume/rate ratio F. The replenishment alters both the gas and liquid composition of the small tank.

Results

To compare the results using this z^* method, I used the same reservoir, fluid and operating conditions as in the previous example. The properties of the condensate bank region are also the same as in the first (y^*) method, presented in Table 33. The comparison between the results obtained from the new model and the commercial reservoir simulator are presented in the figures below. Similar to the y^* method, the mixing values selected (0, 0.2, and 0.5) provide the closest resemblance to the saturation profile from the commercial model. Here, a mixing constant of $A = 0$ indicates no contribution from the reservoir fluid. Later, through comparison, this is shown to produce the best result for the calibration.

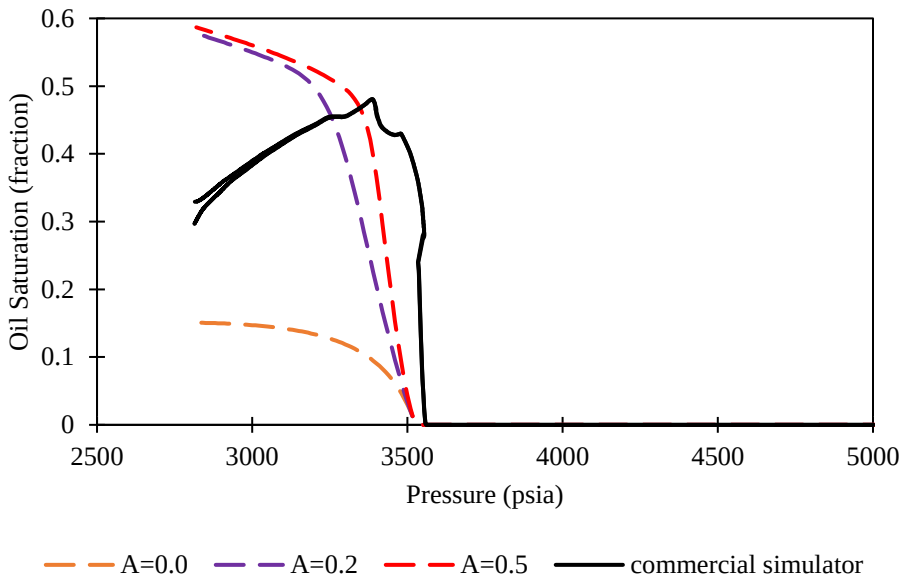

Figure 94 – Small-tank liquid saturation versus pressure using the z^* method. The liquid saturation of the near-wellbore region from the commercial simulator is taken from the gridblock closest to the well.

Using the z^* method, once pressure falls below the dewpoint, we can increase liquid saturation faster than using the y^* method, thus achieving the objective of a steeper liquid

accumulation for the condensate saturation estimation as pressure drops below the dewpoint.

However, the z^* method tends to overestimate the liquid saturation prediction at lower pressures. This can be attributed to its production rules. The value of F in Eq. 5.20 is suppressed by a combination of small values in the numerator ($k_{ro}\mu_g$) and the large values in the denominator ($k_{rg}\mu_o$). This results in very small liquid production from the small tank, leading to the large buildup and overestimation of the liquid saturation in that tank. Future work should improve upon this by allowing more liquid phase to be produced in the production rules. Also, this work assumes that the overall reservoir fluid contributes to the mixing in the small tank, which may not necessarily be true. Due to multiphase phenomena, the fluids coming from the reservoir (big tank) may actually get lighter with time, thus lightening the fluid in the small tank. With the lighter components coming into the small tank, the fluid will tend to be more gas than liquid.

The comparisons between the commercial simulator and the mechanistic model forecasts (considering the z^* method) are presented below. Saturation of liquid versus time is presented in Figure 95. The liquid saturation predicted by z^* method overestimates the liquid saturation significantly. The comparison of average reservoir pressure and bottomhole pressure is presented in Figure 96.

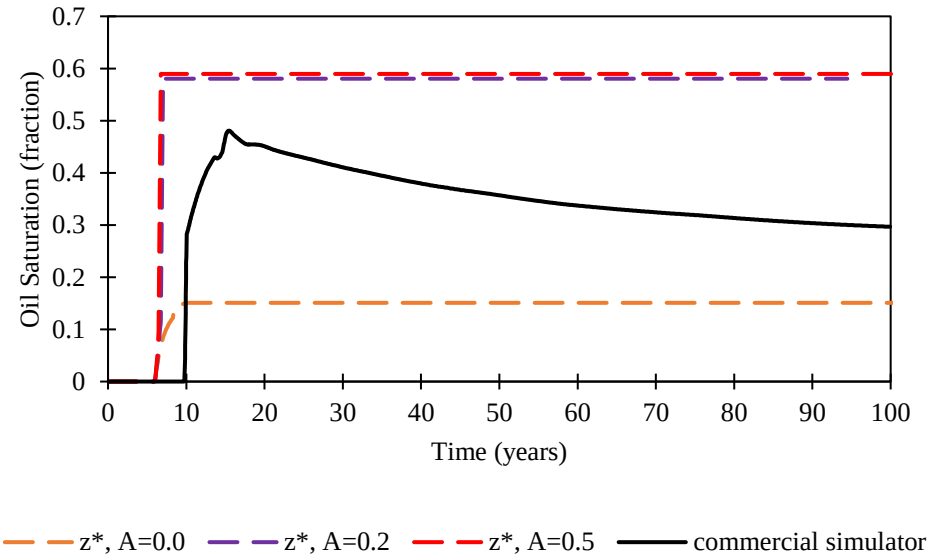

Figure 95 – Small-tank liquid saturation versus time using the z^* method. The liquid saturation of the near-wellbore region from the commercial simulator is taken from the gridblock closest to the well.

Using an A value of 0 results in an underestimation of liquid saturation. A mixing constant of 0 indicates that the small tank does not receive any contribution from the reservoir fluid, so the replenishment portion is ignored. However, using the A value of 0 produces a result closer to the commercial model. This is an interesting observation, since in the first method, the smallest mixing constant results in the best comparison with the commercial model. This indicates that the replenishment from the reservoir is limited and that applying a small value for the mixing constant can better achieve the proper forecasts.

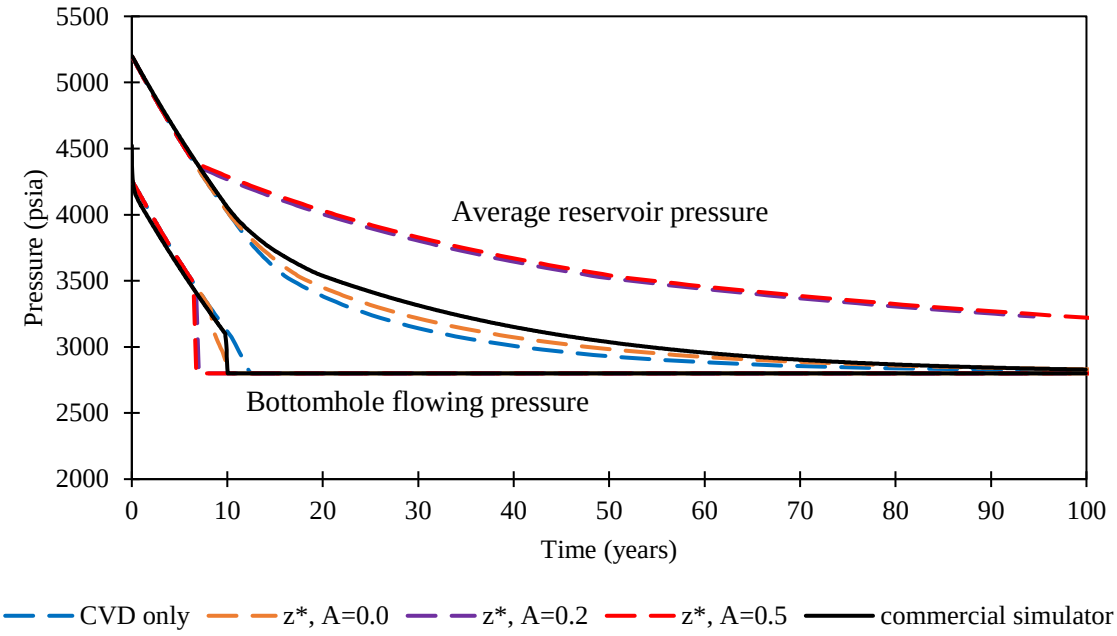

Figure 96 – Average reservoir pressure and bottomhole flowing pressure prediction from the z^* method for near-wellbore liquid saturation buildup.

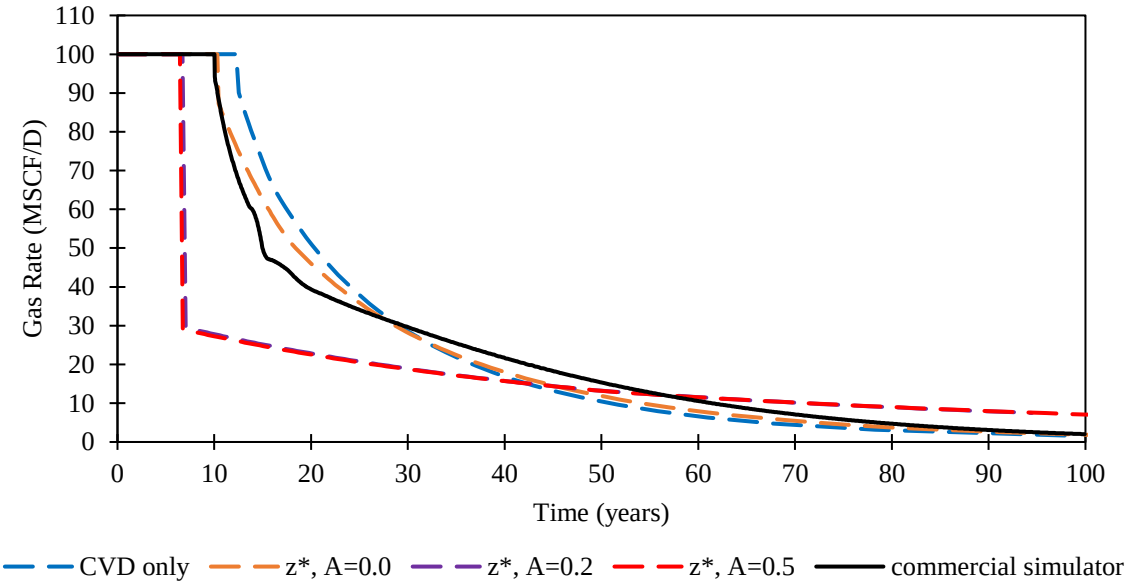

Figure 97 – Gas-rate prediction from the z^* method for near-wellbore liquid-saturation buildup.

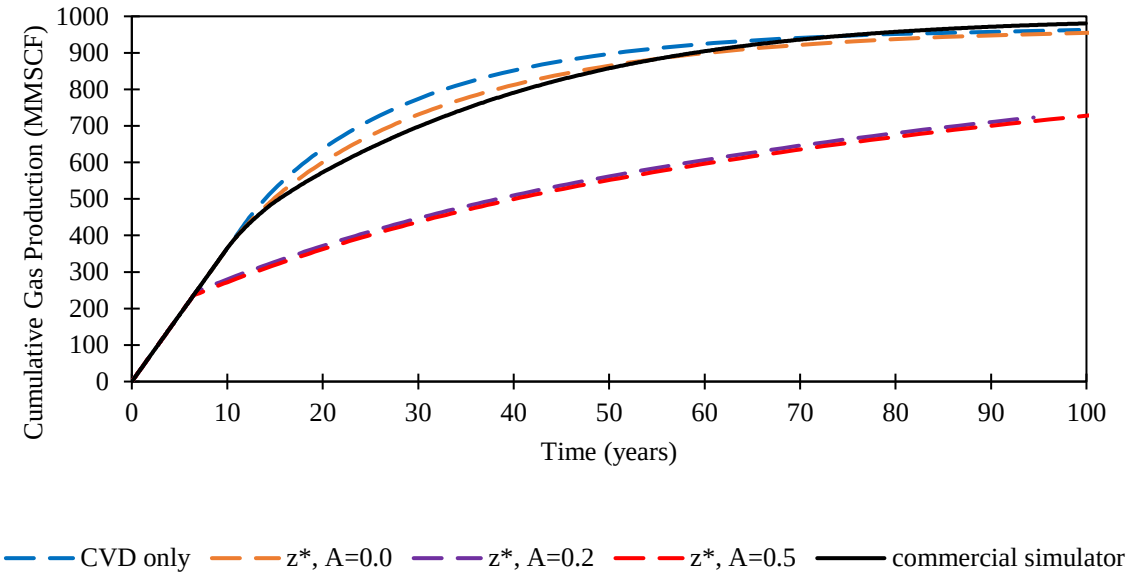

Figure 98 – Gas cumulative production forecasts from the z^* method for near-wellbore liquid saturation buildup.

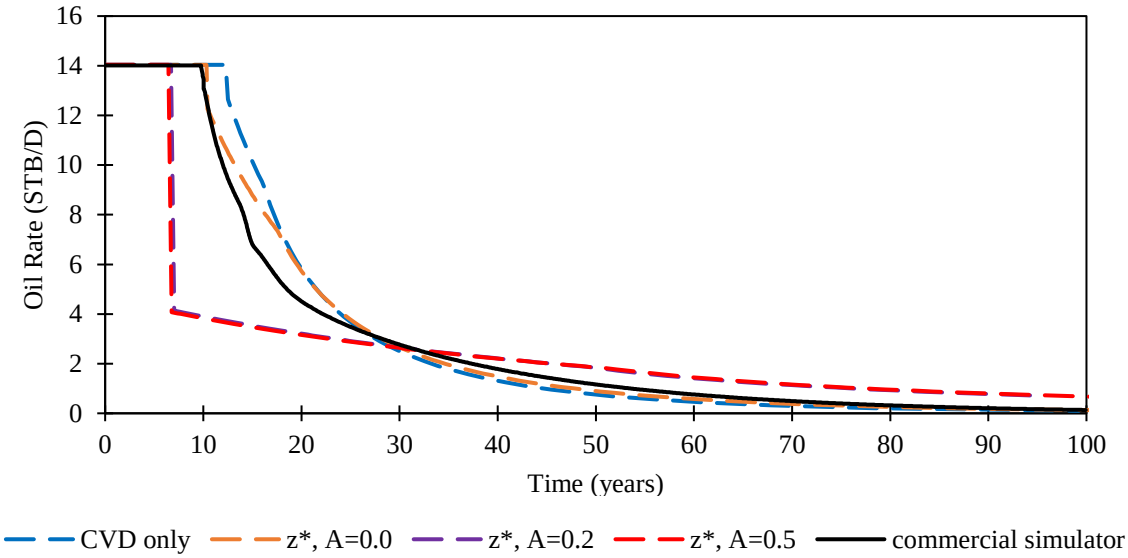

Figure 99 – Oil-rate prediction from the z^* method for near-wellbore liquid saturation buildup.

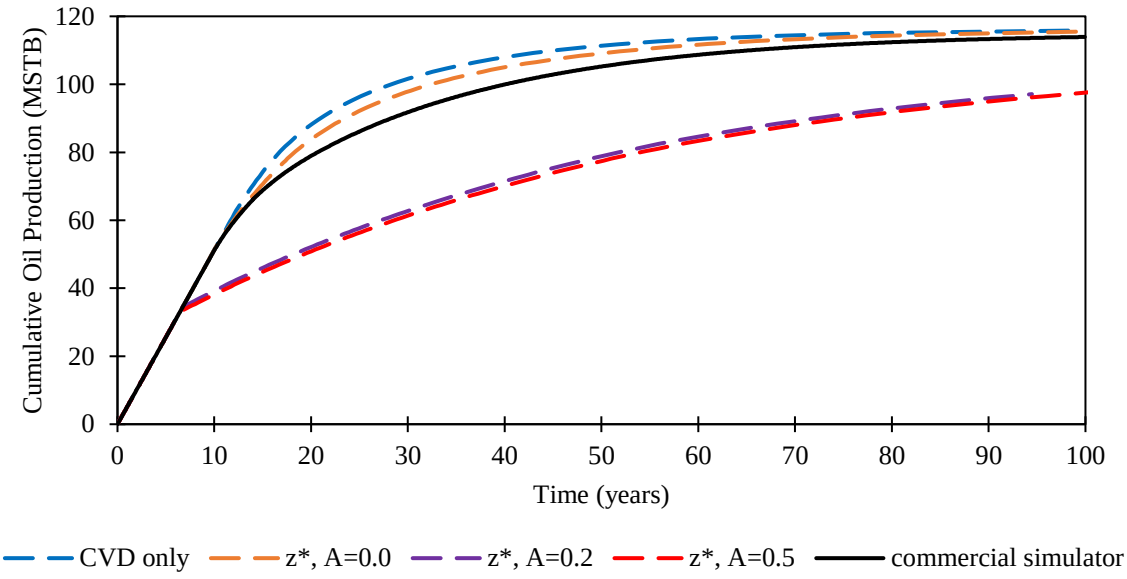

Figure 100 – Oil cumulative production forecasts from the z^* method for near-wellbore liquid saturation buildup.

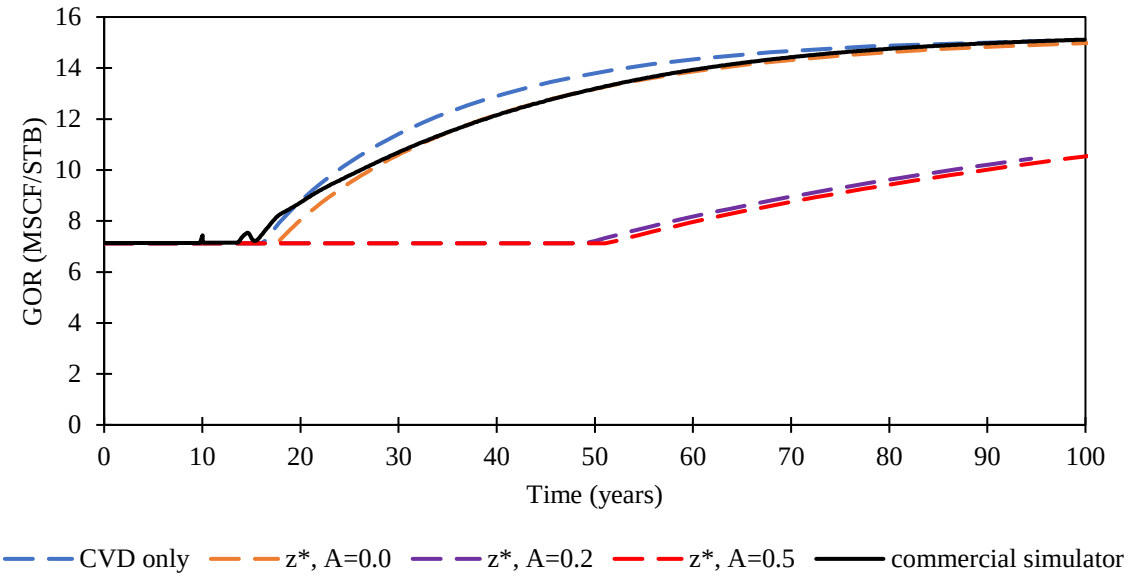

Figure 101 – Gas/oil ratio (GOR) forecasts considering z^* method for near-wellbore liquid saturation buildup.

Table 35 – Average absolute error between the results of mechanistic model (using the z^* method) and the commercial simulator predictions (Eq. 4.15). The highlighted row has the best agreement with the commercial simulator.

	P_{avg}	q_g	G_p	q_o	N_p	GOR
CVD Only	2.0%	13.4%	3.9%	14.4%	4.1%	1.7%
z^*, A = 0.0	1.2%	6.9%	2.0%	8.4%	2.7%	1.4%
z^*, A = 0.2	7.6%	27.6%	19.0%	37.4%	16.1%	15.0%
z^* , A = 0.5	8.2%	31.3%	20.3%	44.2%	17.3%	15.8%

A summary of the errors of the mechanistic model with liquid saturation from the z^* method are presented in Table 35. The selection of the mixing constant A is very significant to improving the mechanistic forecast results. From the gas and oil production forecasts, the higher A value underestimates the production rates. This is due to the lower relative permeability chosen as inputs to the flow equation because of the higher liquid saturation predicted in the condensate-bank model. This trend can be seen for the cumulative production and gas/oil ratio (GOR) results. The mixing constants of 0.2 and 0.5 lead to a higher deviation than without using the calibration (CVD only).

Interestingly, selecting a mixing constant of zero—indicating that there are no contributions from the big tank fluid into the small tank fluid—produced the best forecast calibration, although it means the small-tank CVD ignores the replenishment. This is similar to the first method, where we believe that the mixing parameter chosen by the user should be a low value of around 0 to 0.1.

As mentioned previously, the z^* method is successful in achieving a faster liquid accumulation. However, this method tends to overpredict liquid saturation as pressure decreases. Recommendations for future works to remedy this overestimation are altering the production rules to allow more liquid production or altering the replenishment scheme to allow lighter reservoir fluid into the small tank. Also, we discovered that using a smaller value for mixing constant (A) leads to better calibration of mechanistic model. This can indicate that the fluid contribution from the reservoir to the condensate bank is small.

Future work can also study whether varying the mixing constant A can lead to an improvement in the forecasting.

5.2.3 Integrated Condensate Bank Method

In the third method, I continued the work by using the z^* method approach to estimate condensate-bank liquid saturation. Reasons for using the z^* method are its use of the flow equation in the production rules and its concept of moles entering the small tank from the reservoir. This third method builds upon the z^* method by coupling the method to the production modeling instead of using it only to create a saturation/pressure profile to obtain relative permeability.

In this third method, I combined the condensate bank with the production model (Figure 102). The description of the integration is as follows:

1. The bottomhole flowing pressure of the well (either through calculation or user defined) is obtained from the production model.
2. The small-tank CVD test is conducted at the bottomhole flowing pressure from the production model.
3. The z^* method is conducted and repeated until the cumulative moles produced from the small tank production iterations equals the moles produced from the big tank (reservoir CVD test). This is described in Eq. 5.27 and Eq. 5.28.

$$n^k_{s,\text{cum prod}} = \sum_{k=1}^{N} n^k_{s,\text{prod}} \tag{5.27}$$

$$n_{s,\text{cum prod}} \geq n^{\text{RES},j}_{\text{prod}} \tag{5.28}$$

where

$n^k_{s,\text{cum prod}}$ = cumulative moles produced from the small tank at iteration k

$n_{s,\text{prod}}$ = moles production from small tank at iteration k

$n^{\text{RES},j}_{\text{prod}}$ = moles produced from big tank (reservoir) at pressure step j

N = total number of iteration

4. Once the moles produced between the small and big tanks are equal, the relative permeability value is looked up and used in the flow equation.
5. The composition in the small tank is recorded and used in the next pressure step.

Due to this material balance check between the moles produced in the condensate bank tank and the reservoir tank, this third method is more representative for modeling flow from the reservoir through the condensate bank and into the production well.

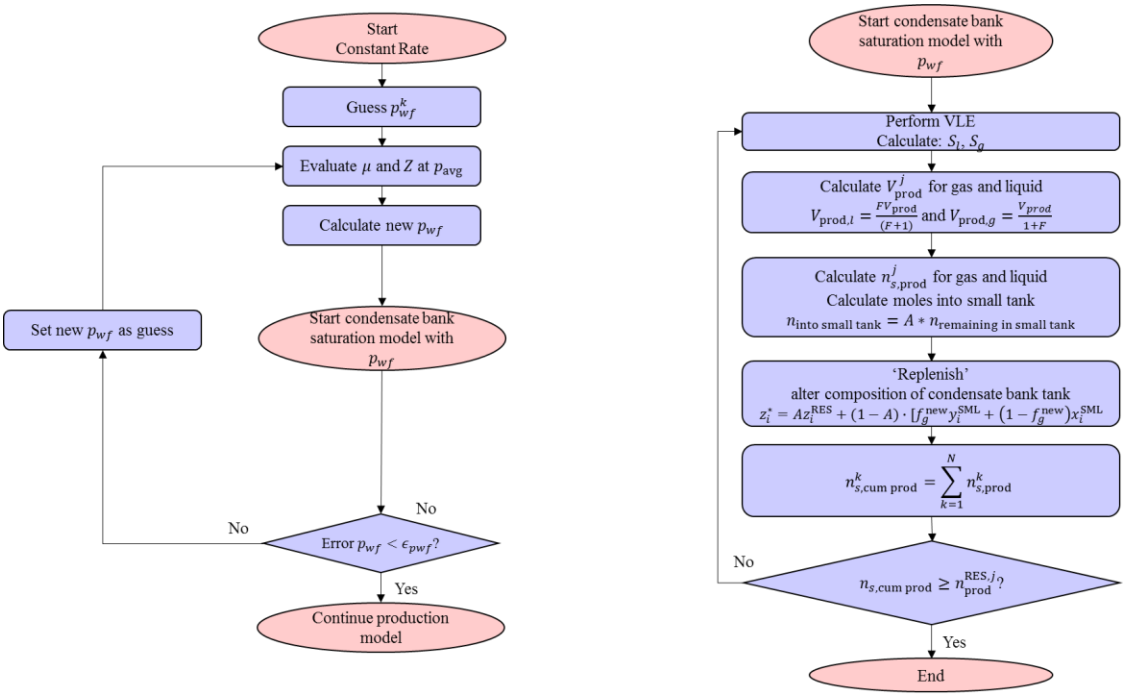

Figure 102 – Workflow of coupled condensate bank tank model with production model.

Results

The test case was used again with the third workflow to compare the forecasting results. The mixing constants were selected for the best calibration results. The saturation

predictions versus time created using this integrated method are presented in Figure 103. This integrated method obtained a different response from the A mixing constant. Here, a smaller mixing constant leads to higher saturation estimation. This is the opposite from the results of Methods 1 and 2.

In this integrated method, the mixing constant (A) control both the composition alterations and the moles that come into the small tank. However, the dominating factor that changes the impact of the mixing constant (A) is the control it has on adding moles into the small-tank system. A higher mixing constant (A) results in higher amounts of moles added through the small tank, and thus higher amounts of moles produced through the small tank. Larger production in the small tank relates to fewer iterations to achieve the equal moles production criteria (moles produced from the small and big tank should be equal). With fewer iterations, there is less contribution from the heavier reservoir fluid, thus resulting in a lower small-tank liquid saturation.

Furthermore, with this model saturation versus time is not a constant as in previous models. This is because in this method the saturation is not looked up as a function of bottomhole pressure but is calculated at every pressure decrement step of the reservoir CVD model. In Figure 103, we can see that the saturation slightly increases with time because of the accumulation that occurs in the small tank.

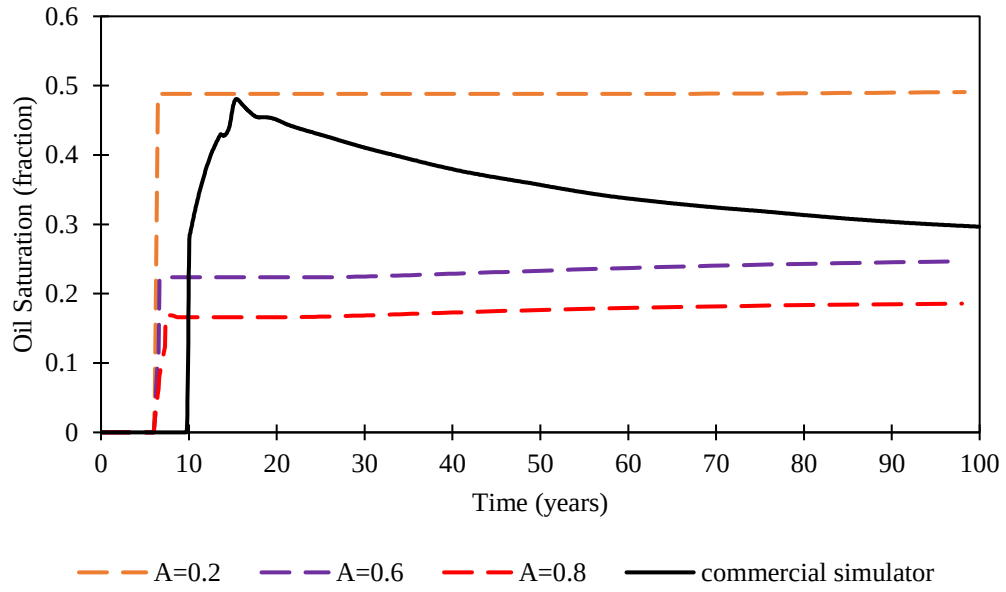

Figure 103 – Small-tank liquid saturation versus time using the integrated z^* method. The liquid saturation of the near wellbore from the commercial simulator is taken from the gridblock closest to the well.

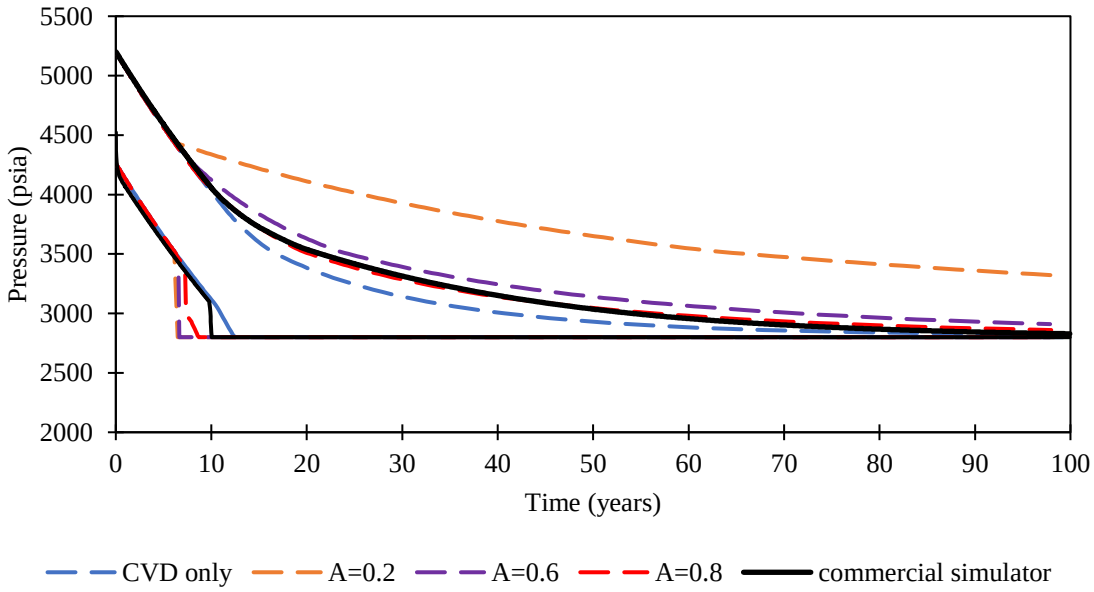

Figure 104 – Average reservoir pressure and bottomhole flowing pressure prediction from the integrated z^* method for near-wellbore liquid saturation buildup.

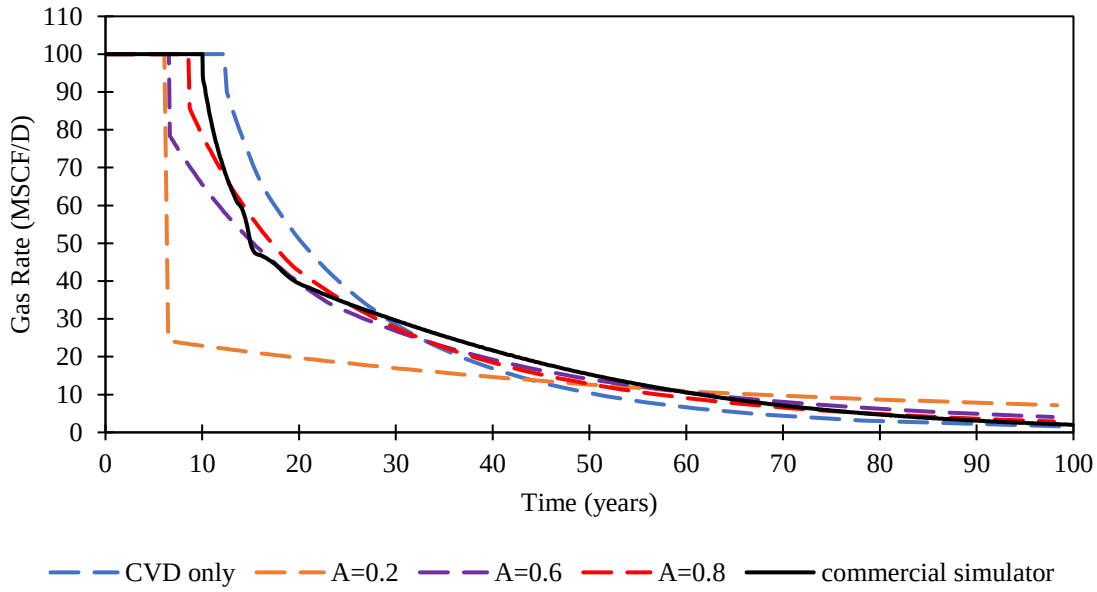

Figure 105 – Gas-rate prediction from the integrated z^* method for near-wellbore liquid saturation buildup.

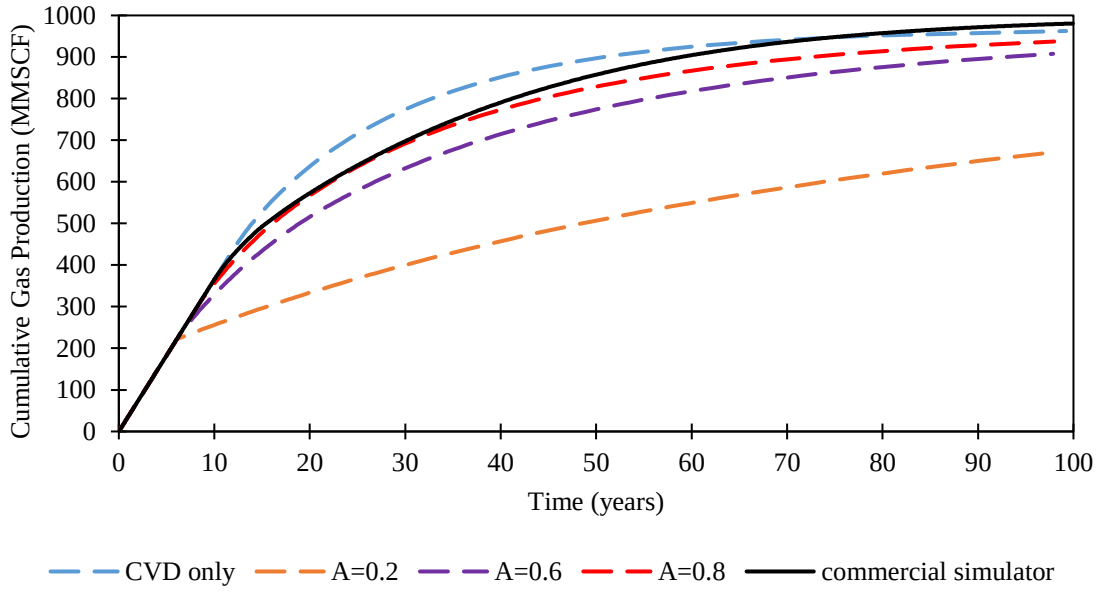

Figure 106 – Gas cumulative production forecasts from the integrated z^* method for near-wellbore liquid saturation buildup.

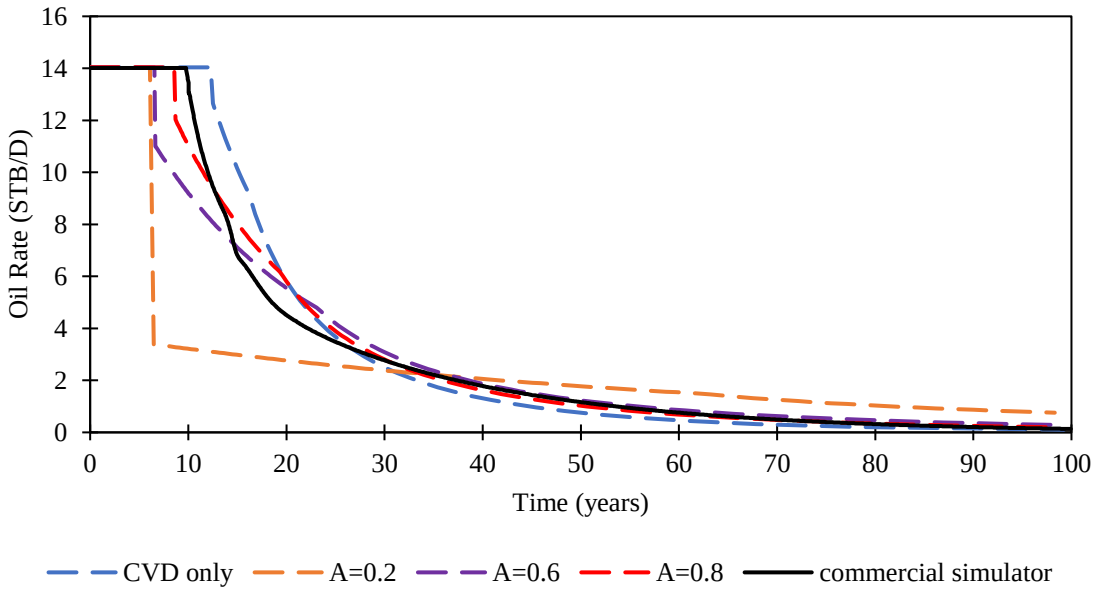

Figure 107 – Oil-rate prediction from the integrated z^* method for near-wellbore liquid saturation buildup.

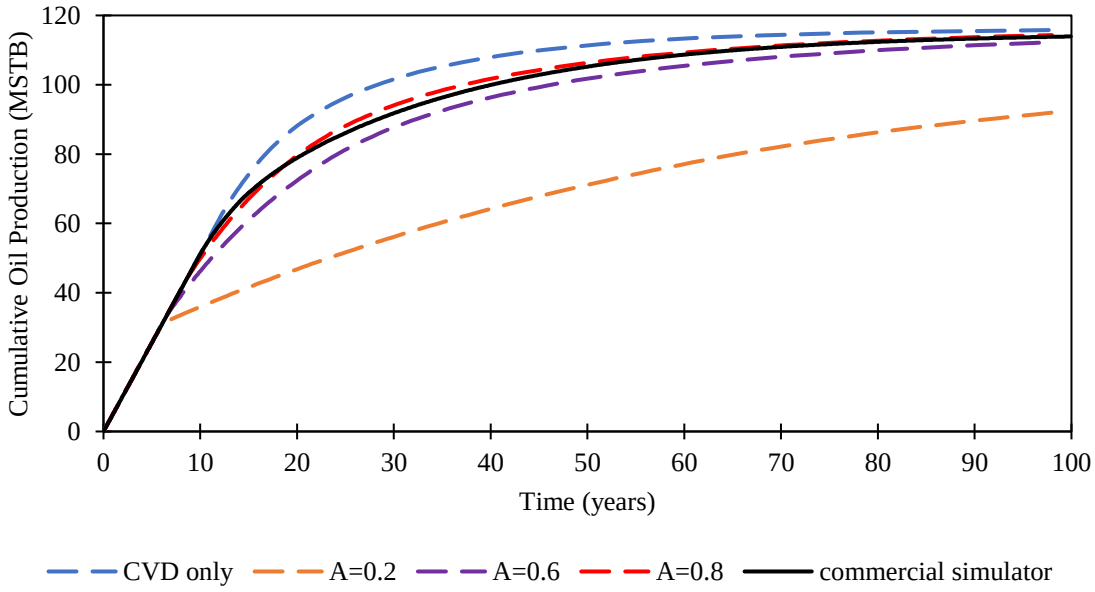

Figure 108 – Oil cumulative production forecasts from the integrated z^* method for near-wellbore liquid saturation buildup.

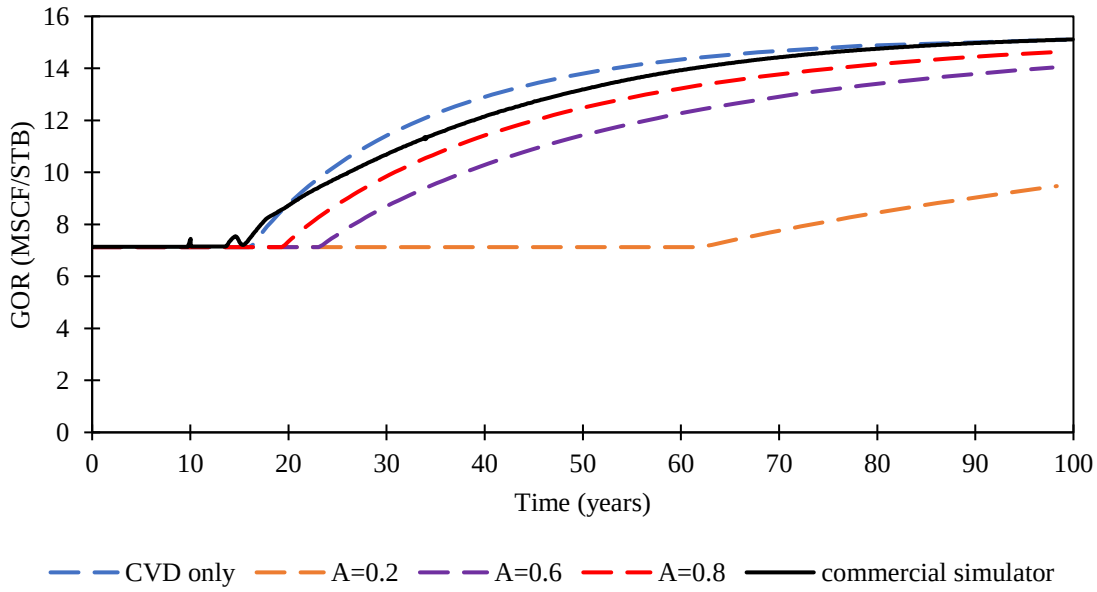

Figure 109 – Gas/oil ratio (GOR) forecasts from the integrated z^* method for near-wellbore liquid saturation buildup.

Table 36 – Average absolute error percentage (Eq. 4.15) between the results of the mechanistic model and the commercial simulator predictions from the integrated condensate bank saturation method.

Forecast Method	P_{avg}	q_g	G_p	q_o	N_p	GOR
CVD Only	2.0%	13.4%	3.9%	14.4%	4.1%	1.7%
Int. z^*, A = 0.2	9.9%	23.3%	23.3%	48.0%	20.2%	17.3%
Int. z^*, A = 0.6	1.7%	9.4%	6.6%	12.5%	4.9%	6.2%
Int. z^*, A = 0.8	0.5%	5.6%	1.9%	7.1%	1.7%	3.2%

Comparing the commercial simulator results to the mechanistic model calibrated using the integrated method, we see that using a higher A value achieved better agreement. This is seen in using both A = 0.6 and A = 0.8. Using this integrated method allows for a more flexible choice for the mixing constant value. For this integrated method, I recommend using a higher A constant of around 0.6 to 1.

All three methods to calibrate the forecasts created by the mechanistic model use a small tank to represent the condensate-bank region. The small tank is based on a modified CVD test that has alterations in the production rules and an added replenishment concept. In the replenishment concept, I introduced a mixing constant (A) to control the contribution of reservoir fluid into the small tank and found that increasing the reservoir fluid contribution leads to a heavier small-tank composition, and thus a higher liquid saturation. This is seen in the results from using the y^* and z^* methods, where higher mixing constants (A) result in higher small-tank liquid saturations. In the integrated condensate-bank model, I created a connection between the small tank and the big tank through the criteria of equal mole production. The small tank is built on the base of the z^* method that is repeated until the small tank produces the same number of moles as the big tank.

Overall, taking the condensate-bank saturation into consideration can improve the mechanistic model predictions. However, this improvement is highly dependent on the mixing constant selected by the user. Choosing an improper mixing constant can lead to higher errors in the mechanistic forecasting results, as shown in this chapter. Further work is needed to provide a better boundary for the mixing constant used in the methods. Also, as mentioned previously, future studies should investigate the effects of altering the compositions coming into the small tank from the reservoir. Allowing for a lighter fluid composition to mix in the small tank can remedy the overestimation of liquid saturation seen in these methods.

CHAPTER VI

CONCLUSION AND RECOMMENDATION

6.1 Conclusions

1. The study has successfully achieved its objectives by delivering a mechanistic production forecasting tool that uses a modified constant volume depletion (CVD) approach that's suitable to forecast the production behavior of liquid-rich systems. The CVD test is programmed in VBA and has been validated with a commercial PVT simulator.
    a. The results of the comparison between the developed CVD test and the commercial PVT simulation were in good agreement, with maximum error under 2.3% deviation from the commercial simulator.
    b. The CVD program was modified to consider the presence of adsorption using the extended Langmuir (EL) model. Acknowledging the work done by (Ambrose et al. 2012) regarding void space taken up by the adsorbed molecules (ϕ_a), I conducted a study on the space occupied by adsorbed gas to understand the impact of adsorbed gas on reservoir capacity. From the study, I conclude that the impact of adsorption on reservoir capacity is greater in smaller pore sizes. Considering single component adsorption (methane), a reservoir with 10% porosity and 10-nm pore diameter, volumetrically, the adsorbed molecules will occupy 0.8% of the void space. I found that the space percentage occupied by the adsorbed molecule significantly decreases as pore size increases.
    c. Using the Peng-Robinson EOS to estimate adsorbed phase density leads to a higher density than using the recommended van der Waals EOS from Ambrose et al. (2012). The higher density of the adsorbed phase increases the storage capacity of the reservoir by decreasing the occupied space taken by the adsorbed phase, thus allowing for greater space for free gas.
    d. The CVD was also modified to produce above the dewpoint pressure and considers production of liquid with gas. These modifications are necessary to mimic

production from gas-condensate reservoirs. The three CVD production methods evaluated in this work are gas-only production, perfect-mixture, and relative-permeability production.

2. The results from the CVD were coupled with pseudosteady-state-flow equations to produce a forecast of oil and gas production from gas-condensate reservoirs. The results were validated with results from a commercial simulator.
   a. Using the mechanistic model, oil and gas rate forecasts considering a single well deviate around 14% from the commercial simulator results while cumulative oil and gas production have a deviation of 4%.
   b. Considering the presence of hydraulic fracturing, the mechanistic model produce results of 18% and 24% deviation from the commercial simulator for the gas and oil rate, respectively, while cumulative produced gas and oil averaged 13% and 19% deviation from the commercial model. This high deviation may be caused by overestimation of negative skin value using the method proposed by Meyer and Jacot (2005).
   c. The mechanistic model is currently not capable of producing reliable results under constant drawdown pressure. This is due to the different definition of drawdown pressure between the mechanistic model and the commercial simulator. A study of pseudodrawdown pressure in the mechanistic found that further studies applying the constant drawdown pressure must be conducted to properly simulate this production constraint.
   d. The deviation between the commercial simulator and the mechanistic model appears to be due to the presence of condensate banking. Liquid accumulation in the near-wellbore area hinders the flow of gas into the well. I attempted to estimate the liquid buildup and calibrate the results of the mechanistic model forecasting, but the results were not encouraging.
   e. The mechanistic model can contribute to the plan of development of a field by giving recovery factor forecasts for different well spacing.

f. Due to the physical basis of the mechanistic model, it was able to develop a better prediction of gas and oil forecast than an Arps decline curve that had limited (2-year) production data. The complex fluid behavior in a gas-condensate reservoir allows for the mechanistic model to better predict the gas and oil production.
g. As more production data becomes available, the Arps decline curves are able to produce a better estimation than the mechanistic model. However, the Arps decline curve consistently underestimates the production from the gas-condensate data set. This is due to the changing behavior of the gas-condensate fluid after pressure falls below the dewpoint.

3. Condensate-banking models are proposed to estimate the liquid saturation buildup in the near-wellbore region. I proposed a small-tank model to represent the condensate-bank region. This small tank is based on the CVD test with an altered production scheme and added replenishment. The liquid saturation estimations created by the small tank model would be used to apply the corresponding relative permeability value in the flow equations. The small tank model does not alter the material balance of the reservoir system.
   a. The y^* method is capable of improving the forecasts of the mechanistic model when a smaller mixing constant (A) of around 0 to 0.2 is used. This method is simple and effective in calibrating the predictions created by the mechanistic model.
   b. The z^* method is less successful in calibrating the forecasts created by the mechanistic model. This method tends to overpredict the liquid-saturation estimation, thus drastically hindering the gas flow.
   c. The integrated model is successful in improving the mechanistic model forecast when a higher mixing constant (between 0.8 and 1) is used to obtain better forecasting results.

6.2 Recommendations

1. Further work is needed to consider shale/tight low-permeability reservoirs:
    a. Coupling the CVD test with the transient-flow equation. Due to the very low permeability of shale reservoirs, the transient-flow regimes can last for months or years. By using the transient-flow equation, better predictions can be made for tight reservoirs.
    b. Consideration of reservoir pore size effects. Currently, this work assumes pore size effects are negligible, thus limiting the use to conventional gas-condensate reservoirs, although this work touched upon the effect of adsorption in small pores prevalent in shale resources. This effect can be included to better understand the production from tight reservoirs.
2. Production forecasting from hydraulically fractured wells require further calibration. This calibration can be through the use of a more conservative formula for effective wellbore radius or through using multiple producing wells to simulate the production from a fracture.
3. Further study is required to properly model the constant-drawdown well constraint. The focus on implementing two different pseudodrawdown pressures, before and after bottomhole pressure falls below the dewpoint, may serve to improve the mechanistic model forecasts.
4. Further improvement to the condensate banking estimations should be made, specifically on the use of proper mixing constant (A). In this work, the A value is kept constant; however, the mixing between the reservoir and the condensate bank may change with pressure, composition, saturation, etc. With the correct mixing constant, better forecasts from the mechanistic model can be made.

REFERENCES

Agarwal, R.G., Gardner, D.C., Kleinsteiber, S.W. et al. 1998. Analyzing Well Production Data Using Combined Type Curve and Decline Curve Analysis Concepts. Presented at the SPE Annual Technical Conference and Exhibition, New Orleans, Louisiana, 27-30 September. SPE-49222-MS. DOI: 10.2118/49222-MS.

Al-Hussainy, R. and Ramey, H.J., Jr. 1966. Application of Real Gas Flow Theory to Well Testing and Deliverability Forecasting. *J Pet Technol* **18** (5): 637-642. SPE-1243-B-PA. DOI: 10.2118/1243-B-PA

Ambrose, R.J., Hartman, R.C., and Akkutlu, I.Y. 2011. Multi-Component Sorbed Phase Considerations for Shale Gas-in-Place Calculations. Presented at the SPE Production and Operations Symposium, Oklahoma City, Oklahoma, 27-29 March. SPE-141416-MS. DOI: 10.2118/141416-MS.

Ambrose, R.J., Hartman, R.C., Diaz-Campos, M. et al. 2012. Shale Gas-in-Place Calculations Part I: New Pore-Scale Considerations. *SPE J.* **17** (1): 219-229. SPE-131772-PA. DOI: 10.2118/131772-PA

Arps, J.J. 1945. Analysis of Decline Curves. *Trans., AIME*, **160**: 228. SPE-945228-G. DOI: 10.2118/945228-G

Barker, J.W. 2005. Experience with Simulation of Condensate Banking Effects in Various Gas Condensate Reservoirs. Presented at the International Petroleum Technology Conference, Doha, Qatar, 21-23 November. IPTC-10382-MS. DOI: 10.2523/IPTC-10382-MS.

Brooks, R.H. and Corey, A.T. 1964. Hydraulic Properties of Porous Media and Their Relation to Drainage Design. *Trans. ASAE* **7** (1): 26-0028. DOI: 10.13031/2013.40684

Cinco-Ley, H. and Samaniego, F. 1981. Transient Pressure Analysis for Fractured Wells. *JPT* **33** (9): 1749-1766. SPE-7490-PA. DOI: 10.2118/7490-PA

Dake, L.P. 1978. *Fundamentals of Reservoir Engineering*, first edition. Oxford, UK: Elsevier.

Darcy, H.P.G. 1856. *Les Fountaines Publiques De La Ville De Dijon*: Victor Dalmont, Paris.

Economides, M.J., Hill, A.D., Ehlig-Economides, C. et al. 2012. *Petroleum Production Systems*, second edition. Westford, Masscachusetts: Pearson Education.

EIA. 2016. U.S. Crude Oil and Natural Gas Proved Reserves, Year-End 2015. http://www.eia.gov/naturalgas/crudeoilreserves/. (accessed 10 January 2017).

Fekete. 2014. Reservoir Fluid Type. http://fekete.com/SAN/TheoryAndEquations/HarmonyTheoryEquations/Content/HTML_Files/Reference_Material/General_Concepts/Reservoir_Fluid_Types.htm. (accessed 21 November 2014).

Fevang, Ø. and Whitson, C.H. 1996. Modeling Gas-Condensate Well Deliverability. *Res Eval & Eng* **11** (4): 221-230. SPE-30714-PA. DOI: 10.2118/30714-PA

Firoozabadi, A. 1999. *Thermodynamics of Hydrocarbon Reservoirs*, first edition. New York, New York: McGraw-Hill.

Gensterblum, Y., Busch, A., and Krooss, B.M. 2014. Molecular Concept and Experimental Evidence of Competitive Adsorption of H2o, Co2 and Ch4 on Organic Material. *Fuel* **115**: 581-588. DOI: 10.1016/j.fuel.2013.07.014

Giamminonni, D., Fanello, G., Kfoury, M. et al. 2010. Condensate Banking Phenomenon Evaluation in Heterogeneous Low Permeability Reservoirs. Presented at the SPE Europe Annual Conference and Exhibition, Barcelona, Spain, 14-17 June. SPE-131582-MS. DOI: 10.2118/131582-MS.

Gong, X., Tian, Y., McVay, D.A. et al. 2013. Assessment of Eagle Ford Shale Oil and Gas Resources. Presented at the SPE Unconventional Resources COnference, Calgary, Alberta, 5-7 November. SPE-167241-MS. DOI: 10.2118/167241-MS.

Guo, B., Al-Bemani, A.S., and Ghalambor, A. 2007. Improvement in Sachdeva's Multiphase Choke Flow Model Using Field Data. *J Can Pet Technol* **40** (5): 22-26. PETSOC-07-05-01. DOI: 10.2118/07-05-01

Hartman, R.C., Ambrose, R.J., Akkutlu, I.Y. et al. 2011. Shale Gas-in-Place Calculations Part II - Multicomponent Gas Adsorption Effects. Presented at the SPE Unconventional Gas Conference, Woodlands, Texas, 14-16 June. SPE-144097-MS. DOI: 10.2118/144097-MS.

Honarpour, M.M., Nagarajan, N.R., Orangi, A. et al. 2012. Characterization of Critical Fluid PVT, Rock, and Rock-Fluid Properties - Impact on Reservoir Performance of Liquid Rich Shales. Presented at the SPE Annual Technical Conference and Exhibition, San Antonio, Texas, 8-10 October. SPE-15842-MS. DOI: 10.2118/158042-MS.

Huerta Quinones, V.A., Lanchimba, A.F., and Porlles, J.W. 2012. Modeling Condensate Banking Phenomena in Lean Gas Condensate Reservoirs. Presented at the SPE Latin American and Caribbean Petroleum Engineering Conference, Mexico City, Mexico, 16-18 April. SPE-153388-MS. DOI: 10.2118/153388-MS.

Kapoor, A., Ritter, J., and Yang, R.T. 1990. An Extended Langmuir Model for Adsorption of Gas Mixtures on Heterogeneous Surfaces. *Langmuir* **6** (3): 660-664. DOI: 10.1021/la00093a022

Lane, W. and Chokshi, R. 2014. Considerations for Optimizing Artificial Lift in Unconventionals. Presented at the Unconventional Resources Technology Conference, Denver, Colorado, 25-27 August. Unconventional Resources Technology Conference. DOI: 10.15530/URTEC-2014-1921823.

Langmuir, I. 1918. The Adsorption of Gases on Plane Surfaces of Glass, Mica and Platinum. *Journal of the American Chemical Society* **40** (9): 1361-1403. DOI: 10.1021/ja02242a004

Lee, S.-T. and Chaverra, M. 1998. Modelling and Interpretation of Condensate Banking for the near Critical Cupiagua Field. Presented at the SPE Annual Technical Conference and Exhibition, New Orleans, Louisiana, 27-30 September. SPE-49265-MS. DOI: 10.2118/49265-MS.

Lohrenz, J., Bray, B.G., and Clark, C.R. 1964. Calculating Viscosities of Reservoir Fluids from Their Compositions. *J Pet Technol* **16** (10): 1171-1176. SPE-915-PA. DOI: 10.2118/915-PA

Luo, S. and Barrufet, M.A. 2006. Simulation Study of Reentry Drilling for Gas-Condensate Reservoir Development. Presented at the SPE International Symposium and Exhibition on Formation Damage Control, Lafayette, Louisiana, 15-17 February. SPE-98142-MS. DOI: 10.2118/98142-MS.

McCain, W.D. 1990. *The Properties of Petroleum Fluids*, second edition. Tulsa, Oklahoma: PennWell Books.

McCain, W.D., Jr. 1994. Heavy Components Control Reservoir Fluid Behavior. SPE-28214-PA. DOI: 10.2118/28214-PA

Meyer, B.R. and Jacot, R.H. 2005. Pseudosteady-State Analysis of Finite Conductivity Vertical Fractures. Presented at the SPE Annual Technical Conference and Exhibition, Dallas, Texas, 9-12 October. SPE-95941-MS. DOI: 10.2118/95941-MS.

Mollerup, J.M. and Michelsen, M.L. 1992. Calculation of Thermodynamic Equilibrium Properties. *Fluid Phase Equilibria* **74**: 1-15. DOI: 10.1016/0378-3812(92)85049-E

Mott, R. 2002. Engineering Calculations of Gas Condensate Well Productivity. Presented at the SPE annual Technical Conference and Exhibition, San Antonio, Texas, 29 September - 2 October. SPE-77551-MS. DOI: 10.2118/77551-MS.

Nelson, P.H. 2009. Pore-Throat Sizes in Sandstones, Tight Sandstones, and Shales. *AAPG Bulletin* **93** (3): 329-340. DOI: 10.1306/10240808059

Norris, H.L. 2012. The Use of a Transient Multiphase Simulator to Predict and Suppress Flow Instabilities in a Horizontal Shale Oil Well. Presented at the SPE Annual Technical Conference and Exhibition, San Antonio, Texas, 8-1 October. SPE-158500-MS. DOI: 10.2118/158500-MS.

Okouma Mangha, V., Guillot, F., Sarfare, M. et al. 2011. Estimated Ultimate Recovery (Eur) as a Function of Production Practices in the Haynesville Shale. Presented at the SPE Annual Technical Conference and Exhibition, Denver, Colorado, 30October - 2 November. SPE-147623-MS. DOI: 10.2118/147623-MS.

Orr, F.M., Jr. 2004. Storage of Carbon Dioxide in Geologic Formations. *J Pet Technol* **56** (9): 90-95. SPE-88842-JPT. DOI: 10.2118/88842-JPT

Péneloux, A., Rauzy, E., and Fréze, R. 1982. A Consistent Correction for Redlich-Kwong-Soave Volumes. *Fluid Phase Equilibria* **8** (1): 7-23. DOI: 10.1016/0378-3812(82)80002-2

Peng, D.-Y. and Robinson, D.B. 1976. A New Two-Constant Equation of State. *Industrial & Engineering Chemistry Fundamentals* **15** (1): 59-64. DOI: 10.1021/i160057a011

Pope, C.D., Palisch, T., and Saldungaray, P. 2012. Improving Completion and Stimulation Effectiveness in Unconventional Reservoirs- Field Results in the Eagle Ford Shale of North America. Presented at the SPE European Unconventional Resources Conference and Exhibition, Vienna, Austrie, 20-22 March. SPE-152839-MS. DOI: 10.2118/152839-MS.

Prats, M. 1961. Effect of Vertical Fractures on Reservoir Behavior-Incompressible Fluid Case. *SPE J.* **1** (2): 105-118. SPE 1575-G. DOI: 10.2118/1575-G

Rachford Jr, H. and Rice, J. 1952. Procedure for Use of Electronic Digital Computers in Calculating Flash Vaporization Hydrocarbon Equilibrium. *J Pet Technol* **4** (10): 19-13. SPE-952327-G. DOI: 10.2118/952327-G

Sayed, M.A. and Al-Muntasheri, G.A. 2014. Liquid Bank Removal in Production Wells Drilled in Gas-Condensate Reservoirs: A Critical Review. *SPE Production & Operations* **30** (02): 85-102. SPE-168153-PA. DOI: 10.2118/168153-PA

Schlumberger. 2014. *Eclipse Technical Description and Reference Manual*. Abingdon, United Kingdom

Smith, J.M., Van Ness, H.C., and Abbott, M.M. 2005. *Introduction to Chemical Engineering Thermodynamics*, 7th edition: McGraw-Hill.

Smits, R.M.M., van der Post, N., and al Shaidi, S.M. 2001. Accurate Prediction of Well Requirements in Gas Condensate Fields. Presented at the SPE Middle East oil Show, Bahrain, 17-20 March. SPE-68173-MS. DOI: 10.2118/68173-MS.

Soave, G. 1972. Equilibrium Constants from a Modified Redlich-Kwong Equation of State. *Chemical Engineering Science* **27** (6): 1197-1203. DOI: 10.1016/0009-2509(72)80096-4

Stiel, L.I. and Thodos, G. 1961. The Viscosity of Nonpolar Gases at Normal Pressures. *AIChE Journal* **7** (4): 611-615. DOI: 10.1002/aic.690070416

Thomas, F.B., Bennion, D.B., and Andersen, G. 2009. Gas Condensate Reservoir Performance. *J Can Pet Technol* **48** (7): 18-24. PETSOC-09-07-18. DOI: 10.2118/09-07-18

Tóth, J. 2003. On Thermodynamical Inconsistency of Isotherm Equations: Gibbs's Thermodynamics. *Journal of Colloid and Interface Science* **262** (1): 25-31. DOI: 10.1016/S0021-9797(03)00236-4

Valbuena Olivares, E. 2011. Analytical Estimation of Co2 Storage Capacity in Depleted Oil and Gas Reservoirs Based on Thermodynamic State Functions. MS thesis, Texas A&M University, College Station. ((June 2011)).

Wheaton, R.J. and Zhang, H.R. 2000. Condensate Banking Dynamics in Gas Condensate Fields: Compositional Changes and Condensate Accumulation around Production Wells. Presented at the SPE Annual Technical Conference and Exhibition, Dallas, Texas, 1-4 October. SPE-62930-MS. DOI: 10.2118/62930-MS.

Whitson, C.H. and Sunjerga, S. 2012. Pvt in Liquid-Rich Shale Reservoirs. Presented at the SPE Annual Technical Conference and Exhibition, San Antonio, Texas, 8-10 October. SPE-155499-MS. DOI: 10.2118/155499-MS.

Whitson, C.H. and Torp, S.B. 1981. Evaluating Constant Volume Depletion Data. *SPE J.* **35** (3). SPE-10067-PA. DOI: 10.2118/10067-PA

Wilson, G.M. 1969. A Modified Redlich-Kwong Equation of State, Application to General Physical Data Calculations. In *65th National AIChE Meeting, Cleveland, OH*.

APPENDIX A

This appendix is to explain the conversion constant used in the adsorbed porosity fraction (Eq. 2.60) shown below.

$$\phi_a^{EL} = 1.318\times10^{-6}\widehat{M}\frac{\rho_b}{\rho_{s_{mix}}}\left[\sum_{i=1}^{n} G_{sLi}\frac{y_i p}{p_{L_i}\left(1+\sum_{j=1}^{n} y_j \frac{p}{p_{L_j}}\right)}\right]$$

where

ϕ_a^{EL} = adsorbed porosity fraction using the extended Langmuir model

ρ_b = bulk rock density (g/cc)

G_{sL_i} = Langmuir volume of component i (scf/ton)

p_{L_i} = Langmuir pressure of component i (psia)

y_i = mole fraction of component i

p = reservoir pressure (psia)

$\widehat{M}$ = mixture molecular weight (lb/lb_{mole} or ton/ton_{mole})

The term in the brackets is the extended Langmuir model with units of scf/ton. We can calculate the molar volume at standard conditions using Eq. A.1.

$$\frac{V}{n} = \frac{RT}{p} \tag{A.1}$$

$$\frac{V}{n} = \frac{10.73159\,\frac{\text{ft}^3\text{psia}}{\text{lb}_{\text{mole}}\,^\circ\text{R}}\cdot(460+60)^\circ\text{R}}{14.7\ \text{psia}} = 379.48\,\frac{\text{ft}^3}{\text{lb}_{\text{mole}}}$$

We must state the molar volume from Eq. A.1 in terms of ton moles to properly convert the units. This is described in Eq. A.2.

$$\frac{1}{379.48\,\frac{\mathrm{ft}^3}{\mathrm{lb}_{\mathrm{mole}}}}\cdot\frac{1\ \mathrm{ton}}{2000\ \mathrm{lb}}=1.318\times10^{-6}\ \frac{\mathrm{ton\ mole}}{\mathrm{ft}^3} \tag{A.2}$$

With this conversion factor, the calculation of the adsorbed void space fraction (ϕ_a) can be obtained, as shown in Eq. A.3. Inputting the units for the terms in Eq. A.1, we see that the units cancel out.

$$\phi_a[=]\left[\frac{\cancel{\text{ton mole}}}{\cancel{\text{ft}^3}}\right]\cdot\left[\frac{\cancel{\text{ton}}}{\cancel{\text{ton mole}}}\right]\cdot\frac{\left[\frac{\cancel{\text{g}}}{\cancel{\text{cc}}}\right]}{\left[\frac{\cancel{\text{g}}}{\cancel{\text{cc}}}\right]}\cdot\left[\frac{\cancel{\text{scf}}}{\cancel{\text{ton}}}\right] \tag{A.3}$$